

Modelling proton relays in molybdenum-containing metalloenzymes

Farhana Haque

A thesis submitted to the University of East Anglia
For the degree of Doctor of Philosophy
Submitted June 2022

This copy of the thesis has been supplied on condition that anyone who consults it is understood to recognise that its copyright rests with the author and that use of any information derived therefrom must be in accordance with current UK Copyright Law. In addition, any quotation or extract must include full attribution. ©

Abstract

Molybdenum is found in the active site of a number of metalloenzymes. It is supported in these systems by one or more sulphide ligands. This combination allows access to a range of oxidation states in which catalysis can take place. Mimicking this intriguing chemistry in synthetic models offers the potential to develop new catalysts for important industrial processes.

In this thesis, we explore the possibility of developing molybdenum-based mimics of two important systems: Nitrogenase and Formate Dehydrogenase (FDH). Central to this modelling is the introduction of a proton relay. These are present in the native enzyme but are largely absent in the currently known synthetic models.

Two approaches were explored in developing nitrogenase mimics. We first utilised a range of *N*-heterocyclic carbenes around molybdenum centre to enhance its electron density. Regrettably we were unable to isolate the target systems. Our second approach was to have molybdenum complexes supported by PNP ligands. Novel PNP ligands were synthesised and coordinated to molybdenum. Crystallisation showed that these ligands gave a mixture of mono- and bis(PNP) complexes. This precluded the study of the reactivity of the individual systems.

Shifting our attention to FDH models, we first developed a new synthetic route to functionalised molybdenum bis dithiolenes. The overall synthetic strategy utilised a 1,3-dithiolone as the key intermediate. Our ligand included a pendant hydroxy group for proton relay. Our initial aim was to explore the effect of a range of protecting groups on the oxygen of the hydroxy group by deprotecting the ligand once it was

coordinated to molybdenum. Unfortunately, the deprotection step was too harsh for our molybdenum carbonyl complex and it decomposed within minutes. We then switched to using the well established technique of transmetallation via nickel. Whilst this impacted on yield, this allowed us to access the target complexes.

Computational simulation is a powerful method for studying difficult to access systems. Here, we employed Density Functional Theory (DFT) to model the behaviour of our target complexes. We established that there is not one strongly preferred isomer.

Electrochemical methods are central to understanding the catalysis of redox active metals. We have studied the fundamental electrochemistry of our nickel and molybdenum dithiolenes and found them to be comparable to literature complexes. We explored the ability of our novel molybdenum dithiolene to catalyse electroreduction, revealing two competing pathways.

Access Condition and Agreement

Each deposit in UEA Digital Repository is protected by copyright and other intellectual property rights, and duplication or sale of all or part of any of the Data Collections is not permitted, except that material may be duplicated by you for your research use or for educational purposes in electronic or print form. You must obtain permission from the copyright holder, usually the author, for any other use. Exceptions only apply where a deposit may be explicitly provided under a stated licence, such as a Creative Commons licence or Open Government licence.

Electronic or print copies may not be offered, whether for sale or otherwise to anyone, unless explicitly stated under a Creative Commons or Open Government license. Unauthorised reproduction, editing or reformatting for resale purposes is explicitly prohibited (except where approved by the copyright holder themselves) and UEA reserves the right to take immediate 'take down' action on behalf of the copyright and/or rights holder if this Access condition of the UEA Digital Repository is breached. Any material in this database has been supplied on the understanding that it is copyright material and that no quotation from the material may be published without proper acknowledgement.

Acknowledgements

Firstly, I would like to thank University of East Anglia and EPSRC for the opportunity to do a Ph.D. Having said that, this would not have been possible without the support of my supervisor, Dr Joseph Wright. Thank you for coming up with an equally challenging project following the setbacks from initial project. Also, thank you for all your help with \LaTeX . Although it took a while to get used to using the programme, it does make editing this large document rather simple. I would like to thank Dr Trevor Simmons for his support and developing a core ligand preparation. Thank you to all EML group members throughout my time in the lab.

I would like to thank The National Crystallography Service, Bruker and Rigaku for collecting X-ray data, and Dr John Fielden for access to the ADF program.

Abbreviations

acac	Pentane-2,4-dionate
Ad	Adamantyl
ADF	Amsterdam density functional
ACHN	1,1'-Azobis(cyclohexanecarbonitrile)
Ac	Acetyl
ADP	Adenosine diphosphate
AIBN	2,2'-Azobis(2-methylpropionitrile)
Ar	Aryl
Arg	Arginine
ATP	Adenosine triphosphate
B3LYP	Becke, 3-parameter, Lee–Yang–Parr
BAr ₄ ^F	Tetrakis(3,5-trifluoromethylphenyl)borate
bdt	Benzene-1,2-dithiolate
Bn	Benzyl
BP86	Becke–Perdew functional
n-Bu	Butyl
^t Bu	<i>tert</i> -Butyl
c_0^∞	Bulk concentration
cat.	Catalytic
Cp	Cyclopentadienyl
Cp [*]	Pentamethylcyclopentadienyl

CV	Cyclic voltammetry
Cy	Cyclohexyl
Cys	Cysteine
δ	Chemical shift
D	Diffusion coefficient
d	Doublet
DBU	1,8-Diazabicyclo[5.4.0]undec-7-ene
dppb	1,4-Bis(diphenylphosphino)butane
DFT	Density functional theory
DMF	Dimethyl formamide
DMSO	Dimethylsulphoxide
E	Potential
EPR	Electron paramagnetic resonance
eq	Equivalents
Et	Ethyl
F	Faraday constant
Fc	Ferrocene
Fc ⁺	Ferrocenium
FDH	Formate dehydrogenase
FeMo	Iron–molybdenum
FT-IR	Fourier transform infrared
GGA	Generalized-gradient approximation
Glu	Glutamic acid
HIPT	Hexaisopropylterphenyl
His	Histidine
HMBT	Hexamethylterphenyl
HMDS	Bis(trimethyl)silylamide
HTBT	Hexa- <i>tert</i> -butylterphenyl

IMes	1,3-Bis(2,4,6-trimethylphenyl)imidazolium
IR	Infrared
i	Current
i_{peak}	Peak current
L	Ligand
LutH	2,6-Lutidinium
m	Multiplet
MPT	Molybdopterin
Me	Methyl
Mes	Mesityl
n	Number of electrons
ν	Scan rate
$\tilde{\nu}$	Wavenumber
NHC	<i>N</i> -Heterocyclic carbene
NMR	Nuclear magnetic resonance
ORTEP	Oak Ridge thermal-ellipsoid plot
Ph	Phenyl
PNP	Phosphine–nitrogen–phosphine ligand
PN ^R P	<i>N</i> -Substituted bis(diethylphoshinomethyl)amine
ppm	Parts per million
^{<i>i</i>} Pr	Isopropyl
q	Quartet
R	Gas constant
R_f	Retention factor
s	Singlet
Sec	Selenocysteine
T	Temperature
t	Triplet

TASF	Tris(dimethylamino)sulphonium difluorotrimethylsilicate
TBAF	Tetrabutylammonium fluoride
TBDMS	<i>tert</i> -Butyldimethylsilyl
TBP	Tris(phosphine)borane
TFA	Trifluoroacetic acid
THF	Tetrahydrofuan
TIPS	Tris(isopropyl)silyl
TPSS	Tao–Perdew–Staroverov–Scuseria
Tyr	Tyrosine
vs	versus
w/v	Weight per volume
ω B97X	Chai and Head-Gordon’s modified Becke functional
XC	Exchange-correlation functional
ZORA	Zero-order regular approximation

Contents

1	Introduction	1
1.1	Metalloenzymes	1
1.2	Nitrogen fixation	2
1.3	Nitrogenases	3
1.3.1	Overview	3
1.3.2	Chemical mechanism	4
1.4	Synthetic nitrogenase mimics	7
1.4.1	Early N ₂ complexes	7
1.4.2	Activation by molybdenum	9
1.4.3	Activation by iron	13
1.5	Beyond nitrogenases	16
1.5.1	Molybdoenzymes	16
1.5.2	Tungstoenzymes	19
1.6	Modelling oxotransferases	19
1.6.1	Xanthine oxidase mimics	19
1.6.2	Sulphite oxidase and DMSO reductase mimics	20
1.6.3	Summary	22
1.7	Activating formate	23
1.7.1	Formate as an energy vector	23
1.7.2	Existing catalytic methods	24

2	Molybdenum nitrogen complexes	25
2.1	Introduction	25
2.1.1	Modelling nitrogenases	25
2.1.2	Carbenes and <i>N</i> -heterocyclic carbenes (NHCs)	26
2.1.3	Molybdenum <i>N</i> -heterocyclic carbene complexes	27
2.1.4	<i>N</i> -Heterocyclic pincer complexes	28
2.1.5	Molybdenum pincer complex	30
2.1.6	Functionalised bis(phosphines) ligands	30
2.1.7	Molybdenum PNP complexes	31
2.1.8	Our approach	32
2.2	Molybdenum NHC complexes	33
2.2.1	Synthesis of imidazolium salts	33
2.2.2	Synthesis of free carbenes	34
2.2.3	Synthesis of molybdenum starting materials	37
2.2.4	Exploring carbene complex synthesis	37
2.2.5	Toward mixed phosphine–carbene complexes	38
2.2.6	Summary	40
2.3	Molybdenum N ₂ complexes bearing PNP ligands	40
2.3.1	Background	40
2.3.2	Synthesis of Mo(N ₂)(PPh ₂ Me) ₄	41
2.3.3	Synthesis of PNP ligands	42
2.3.4	Synthesis of mono(PNP) complexes	44
2.3.5	Synthesis of bis(PNP) complexes	47
2.3.6	Summary	48
2.4	Conclusions	48
3	Synthesis of functionalised molybdenum dithiolene complexes	50
3.1	Introduction	50
3.1.1	Activity of FDH	50

3.1.2	Simple molybdenum dithiolenes	51
3.1.3	Functionalised mimics	53
3.1.4	Our synthetic strategy	54
3.2	Molybdenum carbonyl precursors	55
3.3	Functionalised dithiolone ligands	57
3.3.1	(Propyn-1-yl)benzyl alcohol	57
3.3.2	Unprotected dithiolone	57
3.3.3	TIPS-protected <i>o</i> -dithiolone	58
3.3.4	TBDMS-protected <i>o</i> -dithiolone	60
3.3.5	Benzyl-protected <i>o</i> -dithiolone	60
3.3.6	Unsubstituted dithiolone	61
3.4	Alkynes bearing protected alcohols	61
3.4.1	TIPS-protected <i>o</i> -alkyne	62
3.4.2	Benzyl-protected <i>o</i> -alkyne	63
3.5	Dithiolone formation: from protected alkyne	63
3.5.1	Benzyl-protected <i>o</i> -dithiolone	63
3.5.2	TIPS-protected <i>o</i> -dithiolone	63
3.6	Direct formation of metal dithiolene complexes	64
3.6.1	TIPS-protected molybdenum complex	64
3.6.2	Benzyl-protected molybdenum complex	65
3.6.3	Unfunctionalised molybdenum complex	65
3.7	Deprotection	67
3.7.1	Deprotection of <i>o</i> - 74a using TASF	67
3.7.2	Deprotection of <i>o</i> - 74a using Et ₃ N · 3 HF	67
3.7.3	Deprotection of <i>o</i> - 74a using TBAF	67
3.7.4	Summary	68
3.8	Formation of molybdenum dithiolene complexes via nickel	68
3.8.1	<i>Ortho</i> -nickel complex using TIPS-protected proligand	68

3.8.2	<i>Ortho</i> -nickel complex using TBDMS-protected proligand . . .	69
3.8.3	<i>Ortho</i> -molybdenum complex	70
3.9	Side chain position	71
3.9.1	Ligand preparation	71
3.9.2	Metal complex formation	72
3.10	Summary	75
4	Density functional theory	76
4.1	Introduction	76
4.1.1	Computational methods	76
4.1.2	Previous modelling	77
4.2	Selection of approach	78
4.3	Simulation of dithiolene isomers	79
4.3.1	Detailed analysis of <i>ortho</i> isomers	79
4.3.2	Comparison of isomers	83
4.3.3	Reduced states	86
4.3.4	Additional carbon chain length	91
4.4	Conclusions	93
5	Electrochemistry of nickel and molybdenum dithiolene complexes	94
5.1	Introduction	94
5.1.1	Electrochemical methods	94
5.1.2	Nickel dithiolenes	96
5.1.3	Molybdenum dithiolenes	98
5.2	Nickel bis(dithiolenes)	100
5.2.1	<i>Ortho</i> complex	100
5.2.2	<i>Meta</i> complex	102
5.2.3	<i>Para</i> complex	104
5.3	Molybdenum dithiolenes	106

5.3.1	Molybdenum tris(dithiolenes)	106
5.3.2	Molybdenum bis(dithiolenes)	107
5.4	Conclusion	111
6	Conclusions	112
7	Experimental	115
7.1	General	115
7.2	Molybdenum–dinitrogen complexes	116
7.2.1	1-(2,6-Diisopropylphenyl)-1 <i>H</i> -imidazole 41	116
7.2.2	Pyridine-2,6-diylbis-[3-(2,6-diisopropylphenyl)- 3 <i>H</i> -imidazol-1-ium] dibromide 43	117
7.2.3	1,3-Bis(2,4,6-trimethylphenyl)-1 <i>H</i> -imidazolium bromide 48	117
7.2.4	2,6-Bis-[3-(2,6-diisopropylphenyl)imidazol-2-ylidene]- pyridine 34	118
7.2.5	1,3-Bis(2,4,6-trimethylphenyl)imidazol-2-ylidene 49	119
7.2.6	Bis(dinitrogen)tetrakis(methyldiphenylphosphino)- molybdenum(0) 53	119
7.2.7	PN ^{Ph} P Ligand 56a	120
7.2.8	PN ^{Bn} P Ligand 56b	120
7.2.9	PN ^{Me} P Ligand 56c	121
7.2.10	Complex 57b	121
7.2.11	Complex 57c	122
7.2.12	Complex 58a	122
7.2.13	Complex 58b	122
7.3	Molybdenum carbonyl precursors	123
7.3.1	Tri(acetonitrile)tricarbonylmolybdenum(0) 63	123
7.3.2	η^3 -Toluenetricarbonylmolybdenum(0) 64	123
7.4	Functionalised dithiolene ligands	124

7.4.1	2-(Propyn-1-yl)benzyl alcohol <i>o</i> - 67	124
7.4.2	3-(Propyn-1-yl)benzyl alcohol <i>m</i> - 67	125
7.4.3	4-(Propyn-1-yl)benzyl alcohol <i>p</i> - 67	125
7.4.4	TIPS-protected <i>o</i> -alkyne <i>o</i> - 73a	126
7.4.5	Benzyl-protected <i>o</i> -alkyne <i>o</i> - 73c	127
7.4.6	Unprotected <i>o</i> -dithiolene <i>o</i> - 69	128
7.4.7	<i>Diisopropyl</i> xanthogen disulphide 68	128
7.4.8	Unprotected <i>m</i> -dithiolene <i>m</i> - 69	129
7.4.9	Unprotected <i>p</i> -dithiolene <i>p</i> - 69	130
7.4.10	TIPS-protected <i>o</i> -dithiolone <i>o</i> - 70a	130
7.4.11	TBDMS-protected <i>o</i> -dithiolone <i>o</i> - 70b	131
7.4.12	TBDMS-protected <i>m</i> -dithiolone <i>m</i> - 70b	132
7.4.13	TBDMS-protected <i>p</i> -dithiolone <i>p</i> - 70b	132
7.4.14	Unfunctionalised dithiolone 72	133
7.4.15	Benzyl-protected <i>o</i> -dithiolone <i>o</i> - 70c	133
7.5	Direct formation of metal ditholene complexes	134
7.5.1	TIPS-protected molybdenum complex <i>o</i> - 74a	134
7.5.2	Benzyl-protected molybdenum complex <i>o</i> - 74c	135
7.5.3	Deprotection of <i>o</i> - 74a using TASF	135
7.5.4	Deprotection of <i>o</i> - 74a using Et ₃ N · 3 HF	135
7.5.5	Deprotection of <i>o</i> - 74a using TBAF	135
7.6	Formation of metal dithiolene complexes via nickel	136
7.6.1	<i>Ortho</i> -nickel complex <i>o</i> - 77 using TIPS-protected proligand . .	136
7.6.2	<i>Ortho</i> -nickel complex <i>o</i> - 77 using TBDMS-protected proligand	137
7.6.3	<i>Meta</i> -nickel complex <i>m</i> - 77	137
7.6.4	<i>Para</i> -nickel complex <i>p</i> - 77	138
7.6.5	<i>Ortho</i> -molybdenum complex <i>o</i> - 78	138
7.6.6	<i>Meta</i> -molybdenum complex <i>m</i> - 78	139

7.6.7	<i>Para</i> -molybdenum complex p-78	139
7.7	X-Ray crystallography	139
7.8	DFT calculations	140

Chapter 1

Introduction

1.1 Metalloenzymes

Transition metals offer chemists unique control of reactivity. The ability to vary oxidation state and to tune coordination chemistry using donor/acceptor ligands means that they occupy a central role in catalysis.¹

Enzymes are basic building block of life. About a third of all the currently identified enzymes are metalloenzymes.² Nature has selected to use transition metals for exactly the same reason chemists have: to tune reactivity. However, the exact choice of metals is somewhat different. In the laboratory, precious metals such as platinum and iridium are routinely available, and are used on an industrial scale for key processes. In contrast, in nature, elements used are earth abundant and cheap, for example, iron and copper.³

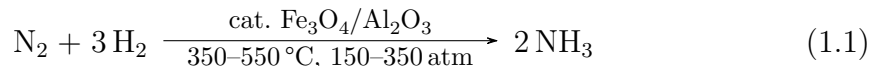
The target of many research groups have long been to combine earth abundant elements with bespoke ligands to catalyse economically important reactions using small molecule mimics. The advantage here is that we can control substrates and avoid the need for large bioreactors.

Before we can mimic enzyme active sites, we need to know what they contain and how they work. The starting point for any chemist designing biomimetic catalysts is

therefore insight into the underpinning knowledge of the active sites of the target enzymes.

1.2 Nitrogen fixation

Reduction of dinitrogen to ammonia is known as nitrogen fixation. Almost 200 million tons of ammonia is used every year, 85 % of which is used in fertilizers.⁴ About half of the ammonia comes from natural processes where bacteria ‘fixes’ nitrogen with the help of an enzyme called nitrogenase. The rest of the ammonia is produced commercially. The industrial method for nitrogen fixation is known as Haber–Bosch process, commercialised in 1910. This process involves very high temperature and high pressure to reduce nitrogen over a heterogeneous iron catalyst. The use of high temperature and pressure in this process makes it very expensive and environmentally unfavourable.⁵



For the last 50 years, chemists have been exploring different catalytic systems that would activate N_2 and reduce it to NH_3 under a much milder condition. N_2 is one of the most stable molecules, reflected by its use in air-sensitive chemistry. With $\text{N}\equiv\text{N}$ bond dissociation energy of 945 kJ mol^{-1} ,^{6,7} designing a synthetic catalytic system to activate $\text{N}\equiv\text{N}$ bond and reduce molecular dinitrogen to ammonia is unsurprisingly one of the challenging aspects of synthetic N_2 fixation.

1.3 Nitrogenases

1.3.1 Overview

Nitrogenases are a family of metalloenzyme present in some bacteria responsible for biological nitrogen fixation. Three distinct nitrogenase systems have been discovered in nature: vanadium dependent (VFe), iron only (FeFe) and molybdenum dependent (MoFe) nitrogenase.⁸ Of the three natural systems, molybdenum dependent nitrogenase has been most thoroughly studied.⁸ Both the molybdenum and iron centres in the molybdenum-dependent nitrogenase are believed to be involved in nitrogen fixation.⁹

Mo-dependent nitrogenase needs two integral proteins: MoFe protein and Fe protein.⁸ The Fe protein contains a [4Fe-4S] cluster (Figure 1.1(a)) and two MgATP binding sites.¹⁰ The MoFe protein contains a multimetallic FeMo-cofactor (Figure 1.1(c)), thought to be the substrate binding site and the P-cluster (Figure 1.1(b)) [8Fe-7S] which is proposed to mediate electron transfer from Fe protein.¹¹

During catalysis, the Fe protein associates with MoFe protein and transfers a single electron while two MgATP molecules are hydrolysed.¹² The Fe protein-2MgADP adduct then detaches from the MoFe protein, allowing another Fe protein-2MgATP to bind to the MoFe protein. This cycle is continued to supply sufficient electrons for dinitrogen reduction. Reduction of N_2 in MoFe protein is only supported by the Fe protein with bound ATP.⁸ Although several other electron transfer proteins can donate electron to the MoFe protein, none of them have shown to support any substrate reduction.¹³ This suggests that the role of Fe protein is more than just donating an electron; it must have some other specific tasks like inducing conformational changes within the MoFe protein to encourage substrate binding to FeMo-cofactor.¹³ Seefeldt and co-workers have found that electron transfer between Fe protein and MoFe protein is conformationally gated, involving protein conformational changes.¹⁴

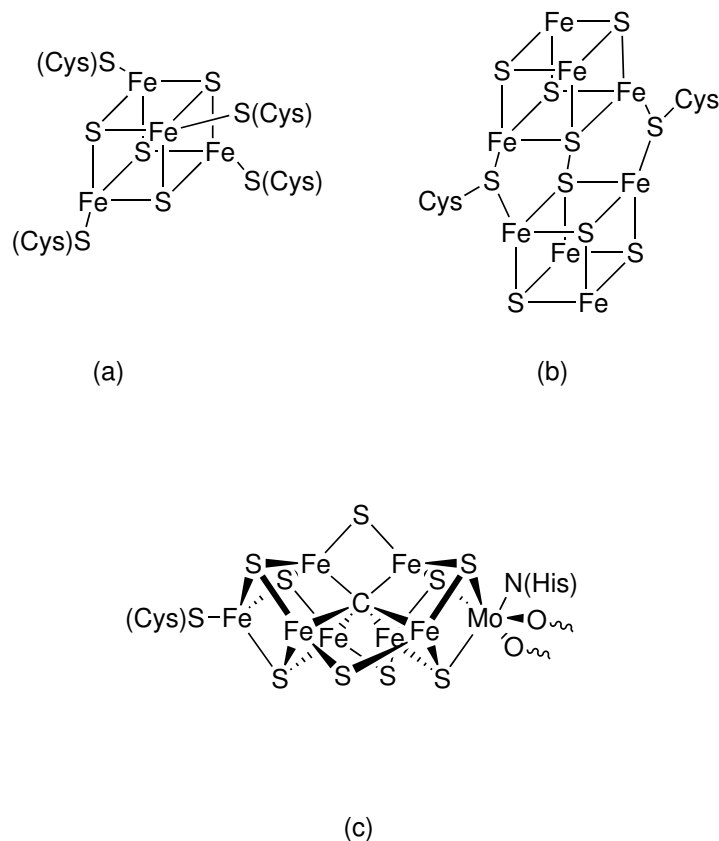


Figure 1.1: The three key metal-and sulphur-containing clusters in molybdenum nitrogenase: (a) $[4\text{Fe}4\text{S}]$ unit (b) P-cluster and (c) FeMo cofactor.

The identity of the interstitial atom in FeMo-cofactor of the MoFe protein was initially unknown. The electron density for this atom is concealed in structures with resolutions lower than 1.55 \AA due to Fourier series termination ripples from surrounding iron and sulphur atoms in the FeMo-cofactor.¹¹ However, Einsle¹⁵ and DeBeer¹⁶ both reported the interstitial atom to be carbon in 2011. This discovery was inspiration for many new synthetic Fe-N₂ model complexes, research by Peters¹⁷ and Holland,¹⁸ for example (see below).

1.3.2 Chemical mechanism

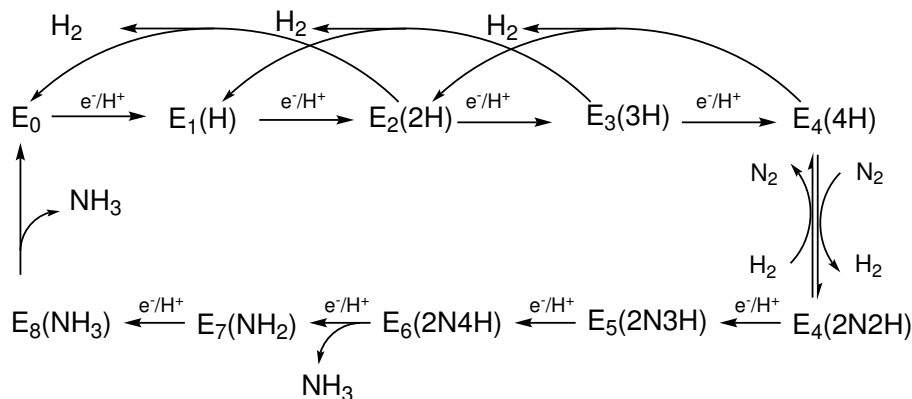
The overall stoichiometry for nitrogen reduction by nitrogenase is more complicated than a simple balanced equation for the formation of two molecules of ammonia. It

is instead given by the equation 1.2.¹⁹



As shown, the reaction forms one equivalent of dihydrogen for each reduced dinitrogen, consuming 4 ATP and 2 electrons.

The foundation of our understanding of this reaction mechanism is extensive kinetic studies conducted in the 1970s and 1980s, most notably led by Lowe and Thorneley.^{8,20,21} Our current understanding is summarised in Scheme 1.1, which is a simplified version of the full Lowe–Thorneley system. The labels E1 to E8 represent electron transfer steps and are routinely used in describing the putative structures of the intermediates.



Scheme 1.1: Simplified Lowe–Thorneley scheme for the nitrogen fixation catalytic cycle of the three nitrogenase enzymes

Nitrogen is not bound until step 4 (E4). This means that up to E4, the chemistry of nitrogenase active site shares key features with hydrogenase enzymes.²² State E4 is when the crucial binding of dinitrogen takes place. This is accompanied by release of one equivalent of dihydrogen. Two mechanisms have been proposed for this process: hydride protonation and reductive elimination. In both of these mechanisms, at least one bridging hydride must switch to a terminal binding mode for the reaction to proceed. The hydride protonation route is analogous with reactions suggested for

in the hydrogenase enzymes.¹⁹ In contrast, the reductive elimination mechanism is distinct from those of other biologically relevant metal hydrides.

Over time, a significant evidence has been obtained in support of the reductive elimination pathway. For example, when the reaction is carried out under D_2 in the presence of H^+ , HD is released.^{8,23,24}

Nitrogen binding may occur in a end-on or side-on fashion. Isolation of bound nitrogen states has to date proved challenging. However, a crystal structure containing CO, a reversible inhibitor, has been obtained.²⁵ This reveals CO binding symmetrically to two iron centres in the FeMo cluster (Figure 1.2). Noting that CO is isoelectronic to N_2 , it can be speculated that this represents the initial site of nitrogen activation.

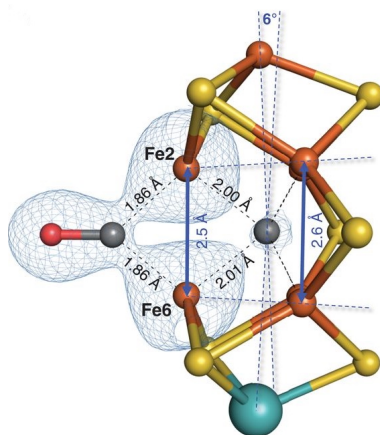
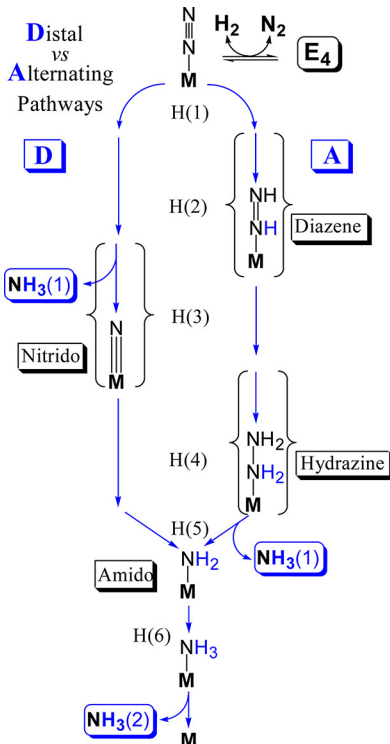


Figure 1.2: Side view of the FeMo cofactor highlighting the binding geometry of CO. Reproduced with permission from reference [25]. Copyright © 2014 The American Association for the Advancement of Science.

There are two possible pathways suggested for the reduction of nitrogen to ammonia (Scheme 1.2). In the distal pathway, a single nitrogen atom is hydrogenated exhaustively to liberate ammonia in three steps. This leaves the second nitrogen atom as a nitrido ligand, which is then converted to ammonia, again in three steps. In contrast, in the alternating pathway, the first two hydrogenation generates a diazene, and the second pair generates a hydrazine before the release of first ammonia, generating the common amido complex. Evidence from mononuclear complexes has in the past been used in support of distal pathway.²⁶ However, more

recently, a number of iron complexes have emerged which operate by an alternating mechanism.^{18,27,28} More conclusive evidence for the alternating pathway has been provided by elegant EPR (Electron Paramagnetic Resonance) experiments.¹⁹



Scheme 1.2: Comparison of distal (D) and alternating (A) pathways for N_2 hydrogenation, highlighting the stages that best distinguish them, most especially noting the different stages at which the first NH_3 is released. Reproduced with permission from reference [19]. Copyright © 2014 American Chemical Society.

1.4 Synthetic nitrogenase mimics

1.4.1 Early N_2 complexes

The first transition metal N_2 complexes, $[\text{Ru}(\text{NH}_3)_5\text{N}_2]\text{X}_2$ ($\mathbf{1X}_2$, Figure 1.3) were reported by Allen and Senoff in 1965²⁹ where $\text{X} = \text{Br}^-$, I^- , BF_4^- and PF_6^- . Cation $\mathbf{1}^{2+}$ was moderately stable in air and decomposed rapidly in water. Infrared spectra of these compounds revealed strong, sharp band between 2170 cm^{-1} and 2115 cm^{-1} , characteristic of N_2 stretching. The N_2 stretching modes seem to have undergone a slight shift towards lower frequency as molecular N_2 stretching is observed at

2331 cm^{-1} ,³⁰ suggesting activation of the coordinated N_2 molecule. Experiments have shown that treatment of the iodide salt ($\text{X} = \text{I}^-$) with 20 % NaBH_4 solution and 40 % NaOH solution evolves 24 % ammonia.²⁹

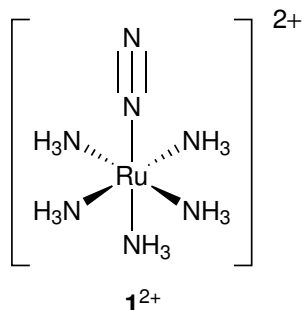


Figure 1.3: The first metal N_2 cation, counter ion Br^- , I^- , BF_4^- and PF_6^- .²⁹

Chatt and co-workers sought to model the function of molybdenum in nitrogenase.⁹ In their approach, they reacted **2** (Figure 1.4) with a number of halide complexes of early transition metals, listed in Table 1.1, to give brightly coloured crystalline products. There is a very strong interaction of the metal ions with the bound dinitrogen molecules, indicated by the reduction of N_2 stretching frequency from 2331 cm^{-1} in molecular N_2 to 1922 cm^{-1} in $[\text{ReCl}(\text{N}_2)(\text{PMe}_2\text{Ph})_4]$ to 1680 cm^{-1} in the $\text{MoCl}_4 \cdot 2\text{Et}_2\text{O}$ adduct.

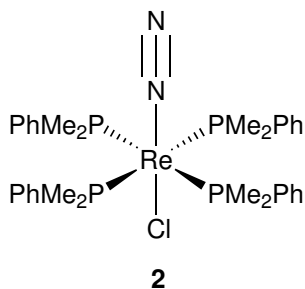


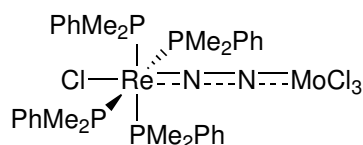
Figure 1.4: Rhenium N_2 complex synthesised by Chatt group.⁹

The first molybdenum N_2 complex to be characterised was the green-brown complex **3** (Figure 1.5).⁹ An explanation of how molybdenum significantly lowers the stretching frequency of N_2 in the adduct is explained by a synergic bonding mechanism.⁹ Thus, the nitrogen ligand acts as both a Lewis acid and a Lewis base,

donating electrons to the molybdenum centre and receiving them from rhenium.

Table 1.1: Colour and $\tilde{\nu}(\text{N}_2)$ of the adduct when reacted with rhenium complex **3**.⁹

Metal halide complexes	Colour	$\tilde{\nu}(\text{N}_2)/\text{cm}^{-1}$
$\text{TiCl}_3 \cdot 3 \text{ THF}$	Intense purple	1805
$\text{CrCl}_3 \cdot 3 \text{ THF}$	Violet-purple	1890
$\text{MoCl}_3 \cdot 3 \text{ THF}$	Green-brown	1850
$\text{MoCl}_4 \cdot 2 \text{ Et}_2\text{O}$	Emerald green	1795
$\text{MoCl}_4 \cdot 2 \text{ Et}_2\text{O}$ (excess)	Bright blue	1680



3

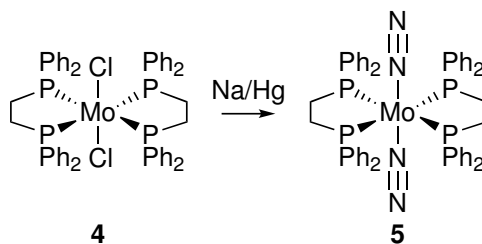
Figure 1.5: Chatt's rhenium-molybdenum complex.⁹

One of the 'truly' catalytic systems have been developed by Shilov and co-workers that presumably involves bimetallic Mo centres.³¹ The system is thought to be catalytic at room temperature and produces up to 170 equivalent of ammonia (with respect to molybdenum) at 110 °C.³¹ The turnover rate is also thought to be almost as good as Fe/Mo nitrogenase. Details on how dinitrogen is reduced in the system have not been explained except that a protic solvent (methanol) contains Mo(III), $\text{Mg}(\text{OH})_2$, some strong reducing agent, i.e. sodium amalgam.³²

1.4.2 Activation by molybdenum

The presence of a single molybdenum centre in the FeMo cluster led to significant interest in mononuclear molybdenum nitrogen complexes. Early work by Chatt, Dilworth, Pickett and others at the nitrogen fixation unit is perhaps most notable. For example, the trans dinitrogen complex **5** can be formed by reduction of the dichloride **4** (Scheme 1.3).

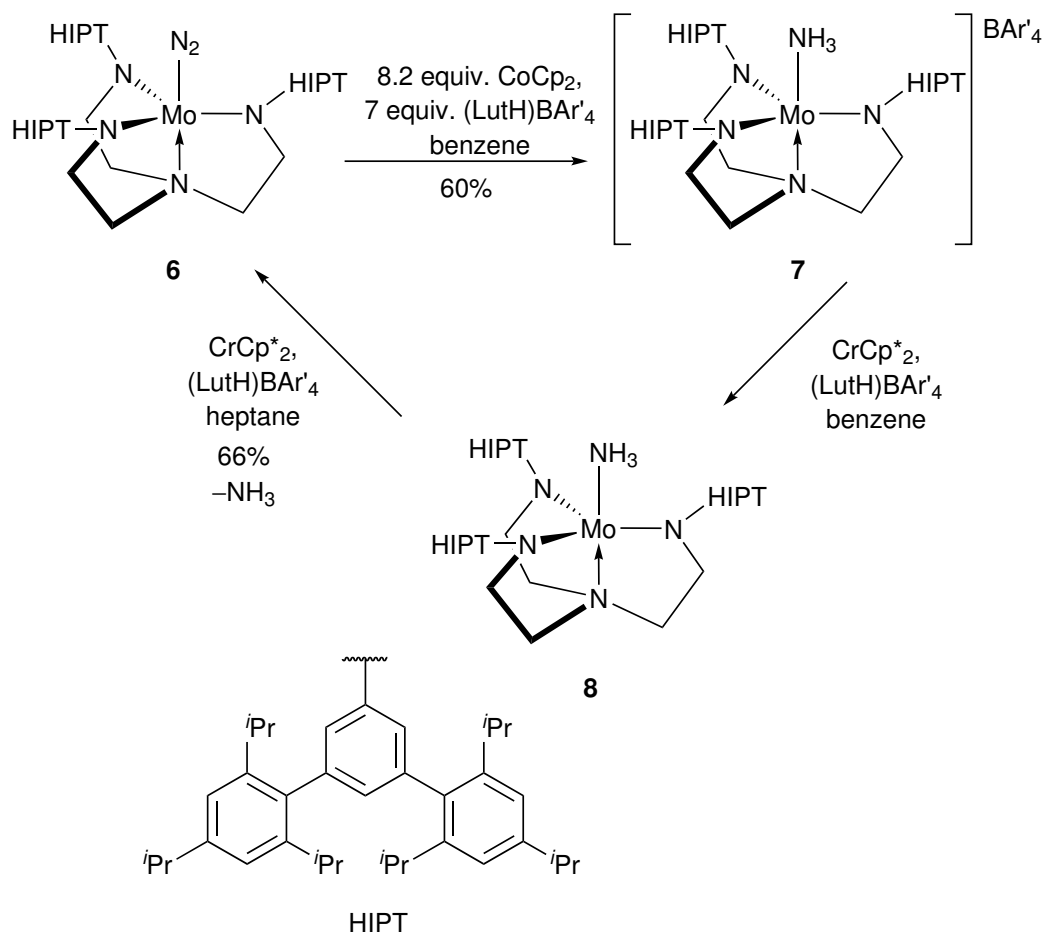
Schrock and co-workers pioneered the investigation on the possibility of activating dinitrogen at a single, well-protected molybdenum centre. They have found that



Scheme 1.3: Example Chatt type complex.³³

triamidoamine ligands were particularly good candidate for complexation with high oxidation state metal centres.³⁴ Using this approach Schrock was able to convert a bound nitrogen to ammonia and then close a formal catalytic cycle using the strong reductant CrCp_2^* (Scheme 1.4).^{35,36} These systems achieved a remarkable efficiencies of up to 66 % compared to 75 % in Fe/Mo nitrogenase.³⁶ The production of dihydrogen in N_2 reduction reactions is the main reason for not reaching 100 % efficiencies even in biological systems.

Tuczek and co-workers established a detailed energy profile for the proposed steps in the reduction of dinitrogen to ammonia catalysed by **6**.³⁷ An energy input of approximately 795 kJ mol^{-1} was calculated to be involved in the conversion of dinitrogen to two equivalent of ammonia, which is very close to the empirical value for biological nitrogen fixation.



Scheme 1.4: Catalytic conversion of dinitrogen to ammonia where Cp = cyclopentadienyl, Cp* = pentamethylcyclopentadienyl and Ar^F = 3,5-(CF₃)₂C₆H₃.^{35,36}

Nishibayashi and co-workers reported a bimetallic molybdenum PNP pincer complex (**9**), shown in Figure 1.6, capable of reducing dinitrogen into ammonia in 2010.³⁸ Like the Chatt system, and in contrast to Schrock's approach, these are Mo(0) system. They also bind nitrogen in both terminal and bridging modes.

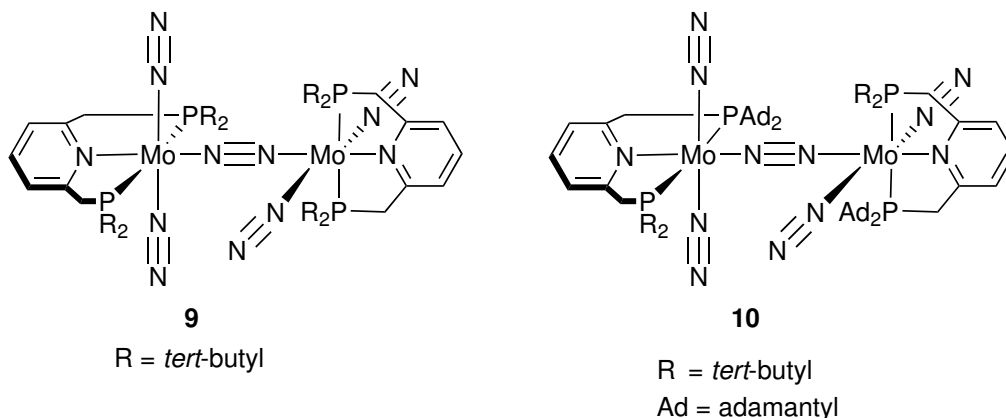


Figure 1.6: Mo PNP complexes reported by Nishibayashi in 2010 and 2012.^{38,39}

There are major differences between this catalyst and Schrock catalyst including that molybdenum is in oxidation state Mo(0) as opposed to Mo(III) in Schrock catalyst, a dimolybdenum complex was utilised instead of a single molybdenum centre and a tridentate PNP pincer ligand was employed rather than a sterically bulky tetradentate HIPT ligand. Calculations by Batista and co-workers suggest that the bimetallic complex catalysed reduction is thermodynamically more favourable than the reduction involving the monometallic complex.⁴⁰

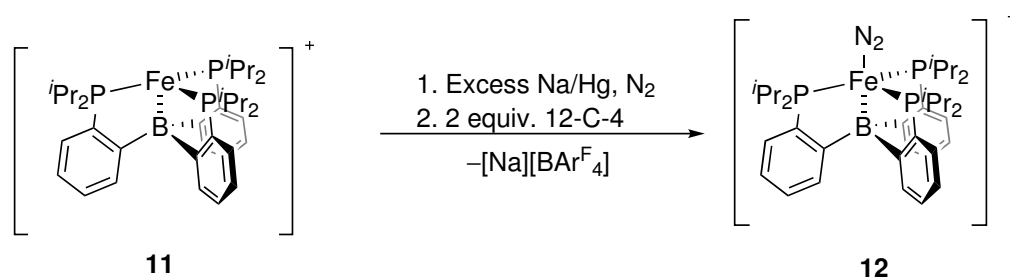
By employing cobaltocene as the electron source and 2,6-lutidinium triflate as the proton source, 12 equivalent of ammonia per molybdenum of the catalyst was produced within 20 hours at room temperature. The catalytic activity of the bimetallic complex is quenched when the tertiary butyl group is substituted with a phenyl group.³⁹ It is believed that the interaction between the two Mo centres facilitate protonation and that the formation of molybdenum hydride is related to the deactivation of the bimetallic catalyst.⁴⁰

In 2012, Nishibayshi found another dinitrogen bridged dimolybdenum complex

featuring PNP pincer ligand (**10**), to be catalytically active towards the reduction of dinitrogen to ammonia under ambient conditions.³⁹ More recently, in 2019, the group have demonstrated that by combining complex **9** with SmI₂ and alcohols turnover numbers of over 4000 can be obtained.⁴¹

1.4.3 Activation by iron

Of the three known hydrogenase enzymes, only one features a molybdenum atom in the catalytically competent cofactor. However, all of them feature multiple iron atoms. It is therefore unsurprising that mononuclear iron systems have attracted attention as potential catalytic mimics. The Peters group reported the first molecular iron complex, **12**, capable of catalysing nitrogen fixation in 2011 (Scheme 1.5).⁴² The substrate free complex, **11**, [(TPB)Fe][BAR₄^F] (TPB = tris(phosphine)borane) and the neutral (TPB)Fe(N₂), **13** (Figure 1.7) can both be reduced to **12** using Na/Hg under 1 atm of N₂ followed by the addition of 2 equivalents of 12-crown-4 (12-C-4) to encapsulate Na⁺.²⁷



Scheme 1.5: TPB supported Fe-N₂ complex.²⁷

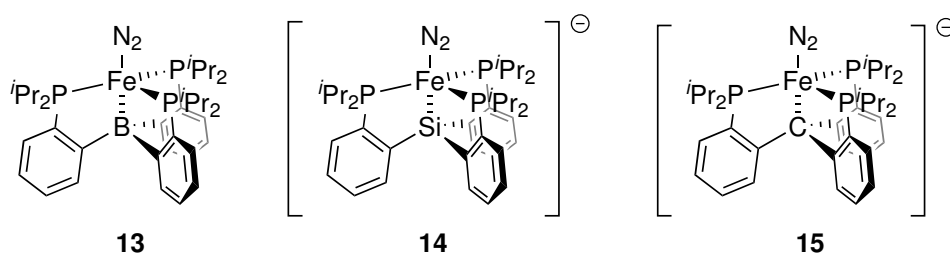
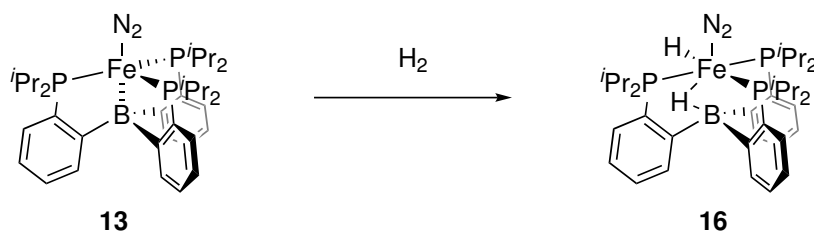


Figure 1.7: Fe-N₂ complex featuring B, Si and C atom as an anchor.¹⁷

Peters has tested a number of different reductants and acids in a variety of solvents at $-78\text{ }^{\circ}\text{C}$ to optimise the catalytic activity of the TPB-Fe system. The combination of KC_8 , $\text{HBAr}_4^{\text{F}} \cdot 2\text{Et}_2\text{O}$ and Et_2O seem to support the highest amount of catalytic generation of NH_3 , with seven equivalent of NH_3 per Fe equivalent in average.²⁷ N_2H_4 was not detected as an additional product with **12**. Reactions involving 2 equivalents of N_2H_4 (per Fe) with **12** under standard catalytic conditions only yielded a trace amount of N_2H_4 .²⁷ Therefore even if N_2H_4 was formed as an intermediate, it would be unlikely to be detected after analysis.

To determine whether a TPB-Fe containing precursor was needed for the catalysis, several Fe complexes were canvassed under analogous conditions.²⁷ One of the interesting complexes found was **14**, which is isostructural to **12** and the only difference is that the B in TPB is replaced by Si.⁴³ The main difference between **12** and **14** was the greater flexibility of the Fe–B bond in comparison to Fe–Si bond, which is *trans* to the apical ligand.^{42,43} Although complex **16** generated some ammonia under standard catalytic condition, Entry 4, Table 1.2, this system is not as effective as the TPB-Fe system. Addition of H_2 to **13** has been shown to generate **16** as a stable product which is suspected of catalyst poisoning (Scheme 1.6).⁴⁴



Scheme 1.6: Poisoning of the catalytic Fe- N_2 complex.^{27,44}

As the interstitial light atom in iron-molybdenum cofactor in MoFe nitrogenase has been identified as carbon,⁴⁵ Peters modelled a new Fe- N_2 complex, **14** with carbon as an ‘anchor’ to understand its role in the cofactor.¹⁷ This complex demonstrated moderate catalytic activity towards nitrogen fixation under the same standard conditions used before (Entry 3, Table 1.2).

Table 1.2: Ammonia generation from dinitrogen mediated by Fe precursors.^{17,27}

Entry	Fe precursor	NH ₃ equivalent/Fe
1	Compound 12	7.0
2	Compound 11	6.2
3	Compound 15	4.6
4	Compound 14	0.7
5	Compound 16	0.5

The central iron atoms in the FeMo cofactor, bound by sulphur and carbon, have been proposed to be the site of substrate binding.¹⁹ Taking inspiration from this, the Holland group have reported the first synthetic Fe-N₂ complex, **17**, supported by sulphur and carbon ligands in 2015 (Figure 1.8).¹⁸ This thermally sensitive complex was stable at -70 °C. Infrared spectroscopy of this complex revealed a strong stretching band at 1880 cm⁻¹.¹⁸ This suggests that the thiolates are powerful electron donor, allowing substantial back bonding from Fe to N₂, weakening N≡N bond.

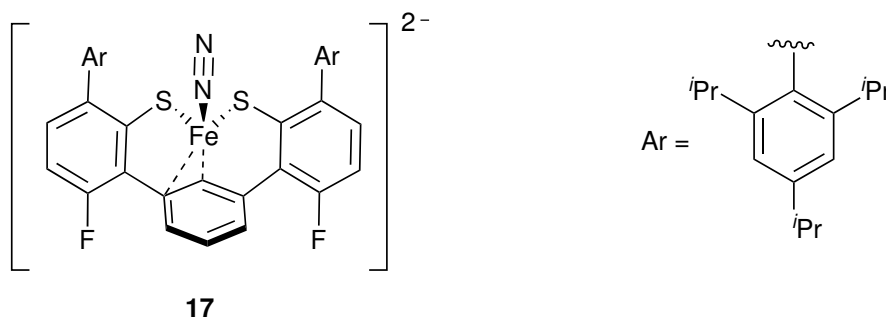
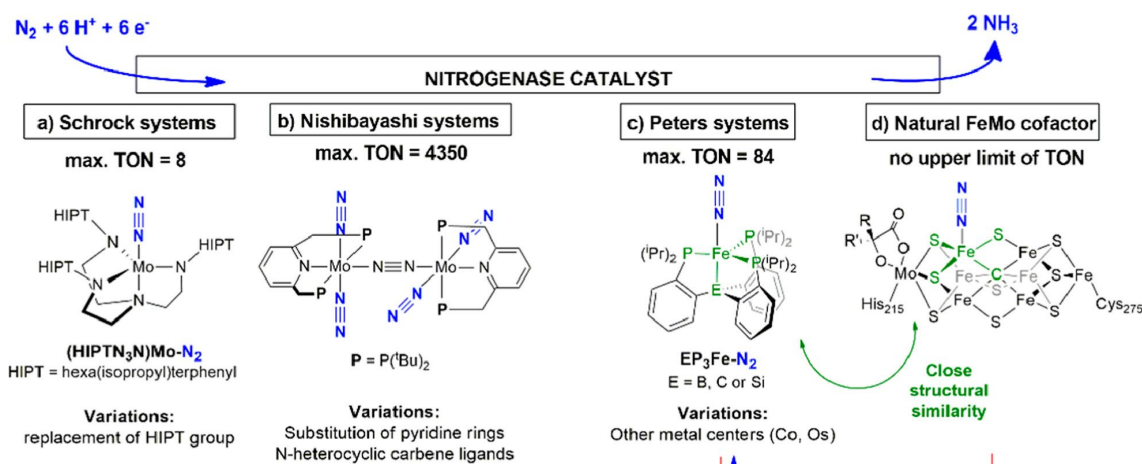


Figure 1.8: Fe-N₂ complex supported by sulphur and carbon ligands.¹⁸

Very recent computational work by the Oláh group has examined the deactivation of synthetic models and the limit this places on turnover number (Scheme 1.7).⁴⁶ This study showed that in the case of Peters type catalyst, the Gibbs free energy of H₂ and N₂ binding are strongly correlated. It is binding of H₂ and subsequent hydride formation which is responsible for deactivation. Oláh suggests that higher turnover numbers are likely to be obtained by removal of dihydrogen from the reaction mixture rather than modifying the catalyst.



Scheme 1.7: Representative structures of artificial and natural catalysts for atmospheric pressure ammonia synthesis, shown together with the highest obtained turnover numbers. Modified with permission from reference [46]. Copyright © 2022 American Chemical Society.

1.5 Beyond nitrogenases

1.5.1 Molybdoenzymes

Looking beyond the most well known metalloenzyme in the world, nitrogenase, there was a large number of molybdoenzymes. All of these contain at least one dithiolene ligand and can be divided into three distinct families. Although not all of these are responsible for transferring oxygen, they are often informally known as oxotransferases.

The three distinct families are exemplified by the enzymes xanthine oxidase, sulphite oxidase and DMSO reductase (Figure 1.9).⁴⁷ In all of these enzymes the molybdenum is ligated by a dithiolene cofactor known as pyranopterin (**18**, Figure 1.10). Both xanthine oxidase and sulphite oxidase families feature square pyramidal molybdenum bearing one pyranopterin and one oxo ligand in the square plane. They vary in the fourth ligand in the equatorial plane and in the axial ligand. In contrast, the DMSO reductase family feature two dithiolenes at the trigonal prismatic metal. The remaining coordination sites bear a range of oxo, thiolato, hydroxy and selenato groups.

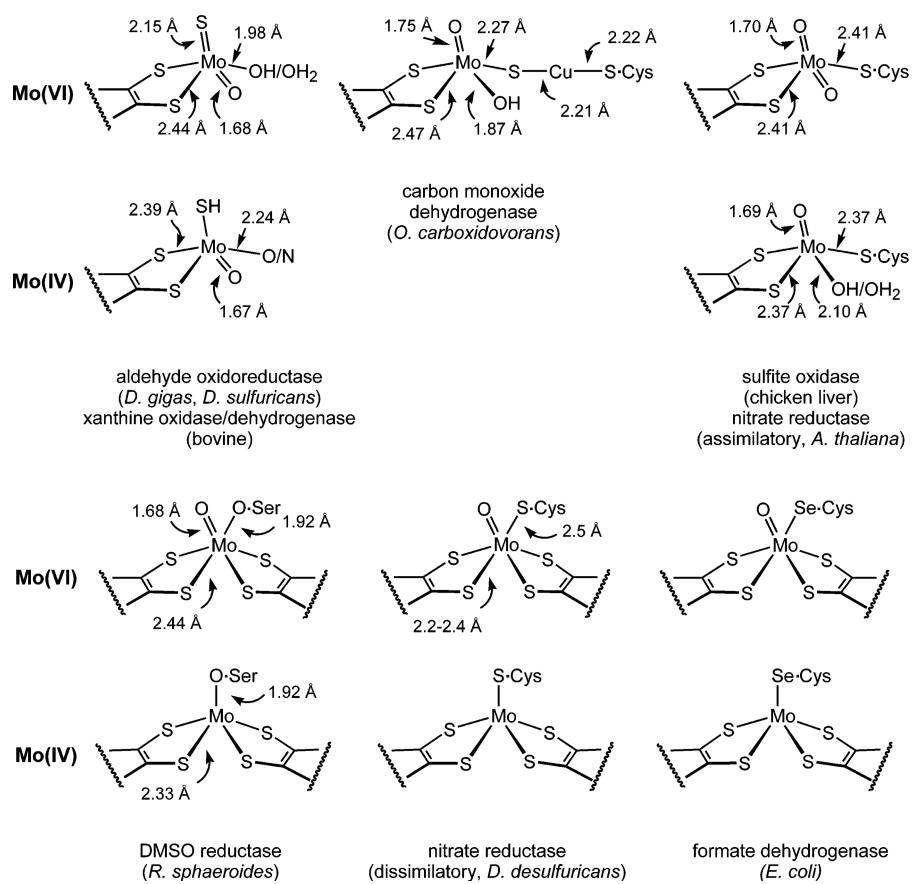


Figure 1.9: Structure of the active sites of oxotransferase enzymes. Modified with permission from reference [48]. Copyright © 2004 American Chemical Society.

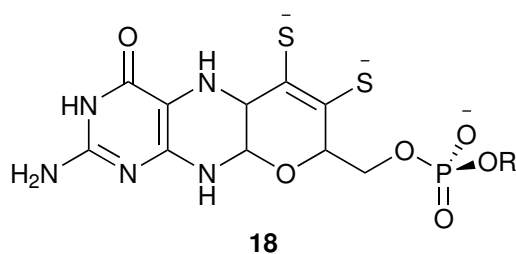


Figure 1.10: Structure of the pyranopterinodithiolate ligand.

Members of the xanthine oxidase family typically catalyse oxidative hydroxylation. Bovine xanthine oxidase was first isolated in 1924 and is therefore one of the most extensively studied enzymes known.⁴⁹ Almost all organisms use xanthine oxidase to degrade purines. Most organisms also utilise aldehyde oxidases from the same enzyme family.

The consensus mechanism for purine oxidation by xanthine oxidase utilises a glutamate from the protein as a proton acceptor in concerted oxygen transfer step (Figure 1.11).^{50,51} This step is accompanied by formal reduction of the metal from Mo(VI) to Mo(IV).

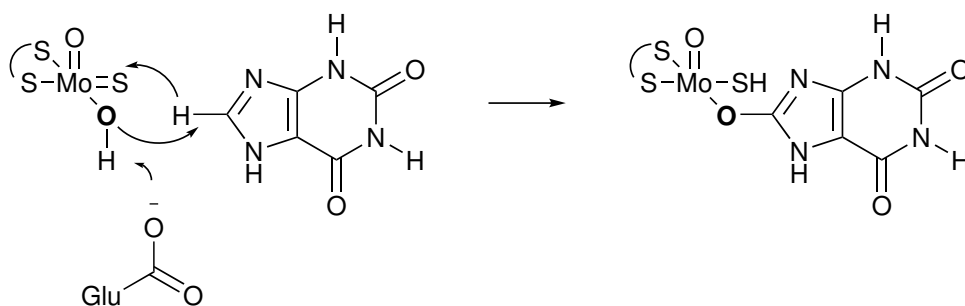


Figure 1.11: The reaction mechanism of xanthine oxidase.^{50,51}

The most interesting variation in the xanthine oxidase family is CO dehydrogenase. This features a binuclear active site, in which Cu(I) centre is bound to molybdenum via a sulphur bridge (Figure 1.9).⁵² The position of copper in the active site has previously been modelled by selenium.

Sulphite oxidase enzyme family act as true oxygen atom transferases. Sulphite oxidase itself is oxygen donor, whereas nitrate reductase acts as an oxygen atom acceptor. As with the xanthine oxidases, these enzymes are found in both prokaryotes and eukaryotes. The latter include examples from both animal and plants. The mechanism of oxygen transfer has been studied by density functional theory (DFT) methods.⁵³ This established that the equatorial M=O antibonding π^* is central to formation of a bound hydroxy, which then breaks down to give the product.

The final family, DMSO reductase, is by far the most varied both in terms of the

structure of the active site and the types of catalysis carried out. Unlike the other two enzyme families, DMSO reductases are only found in prokaryotes. The majority of these enzymes carry out oxygen transfer, but there are also examples of other forms of redox chemistry and hydroxylation. Unlike xanthine and sulphite oxidase enzymes, DMSO reductases exhibit strong visible absorptions.^{54,55} This allows convenient study of mechanism and kinetics. Formate dehydrogenase (FDH) is a member of the DMSO reductase family and will be covered in more detail in Chapter 3.

1.5.2 Tungstoenzymes

It is well known that elements in the same group share common reactivity features. At the same time differences in, for example, size, d-orbital splitting and preferred oxidation states mean that there are key differences between similar metals. It is therefore unsurprising that tungstoenzymes have also evolved in the biological systems. Some of these carry out the same processes as their molybdenum counterparts, whereas others offer unique reactivity.⁵⁶ All known tungstoenzymes are members of DMSO reductase family as they bear two pyranopterin ligands.^{57,58}

1.6 Modelling oxotransferases

1.6.1 Xanthine oxidase mimics

Nearly 20 years ago, Holm stated that⁴⁸

With molybdenum, meaningful site analogues and analogue reaction systems of the [sulphite oxidase] and DMSO [reductase] families have been achieved, but not yet in the [xanthine oxidase] family, which is not further considered.

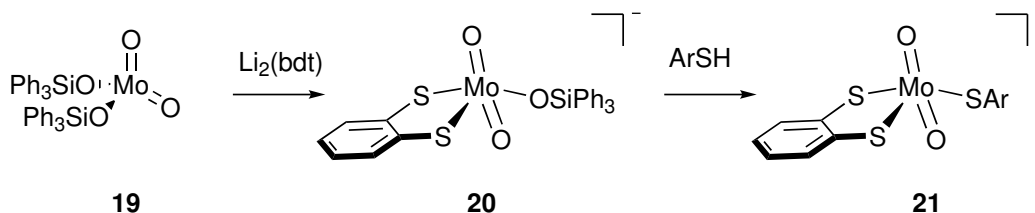
To this date the above remains true: there are no reported structural mimics of xanthine oxidase enzymes that contain a dithiolene ligand. Instead, the key target in

this area has been reproducing the primary coordination sphere of the metal. Even given this limited ambition, there are surprisingly few models. Those which have been reported are ligated by polydentate nitrogen donors. As such, large amount of work remains to be done to obtain realistic structural models in this family.

1.6.2 Sulphite oxidase and DMSO reductase mimics

In contrast to xanthine oxidase mimics there are dithiolene containing models for both sulphite oxidase and DMSO reductase enzymes. Synthetic route to mono- and bis(dithiolenes) share common pathways and therefore, it is convenient to consider them together. There are also non-dithiolene mimics for sulphite oxidase active site, which as in the xanthine oxidase case are focussed on the primary coordination sphere. The latter are of limited interest here, and are covered in detail by Holm.⁴⁸

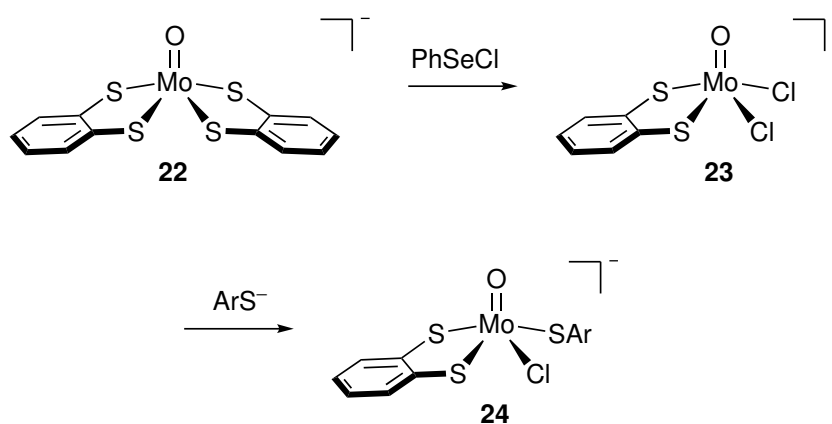
Introduction of single dithiolene proves to be quite challenging at molybdenum as there is a tendency to form bis(dithiolene) preferentially. There are two strategies to overcome this problem. The first is to make the metal centre sufficiently bulky so there is capacity for only one dithiolene ligand (Scheme 1.8).⁵⁹ Thus for example, Holm used a bulky triphenylsiloxy group to allow access to the mono(dithiolene) complex (**20**) from the simple molybdenum starting material (**19**). This could then be elaborated to the sulphite oxidase mimic (**21**).



Scheme 1.8: Synthesis of a sulphite oxidase model using bulky ligand (Ar = 2,4,6-*i*-Pr₃C₆H₂, bdt = benzene-1,2-dithiolate).⁵⁹

The second approach to form mono(dithiolenes) is to first form bis(dithiolene) (see below) and then to cleave one of these ligands from the metal. The key step here is the use of a reagent capable of targeting the dithiolene. Holm achieved

this using the electrophilic reagent PhSeCl, which captures a dithiolate ligand as a selenosulphide (Scheme 1.9).⁵⁹



Scheme 1.9: Synthesis of a sulphite oxidase model via a bis(dithiolene) intermediate (Ar = 2,4,6-*i*Pr₃C₆H₂).⁵⁹

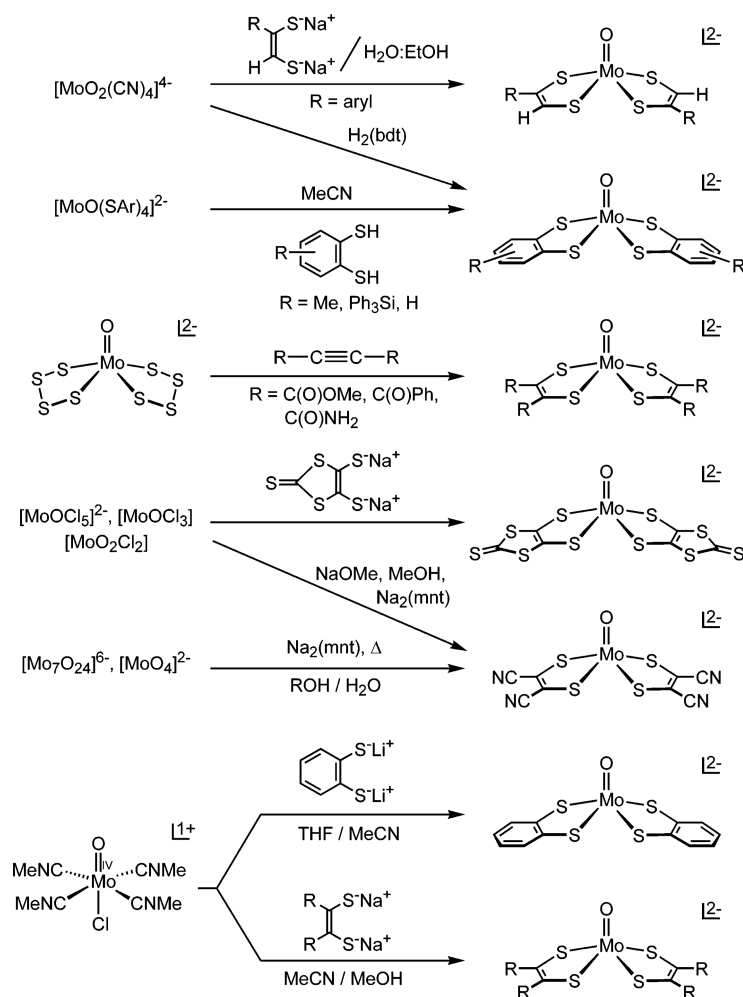
Turning our attention to DMSO reductase mimics, a wide range of approaches have been explored for the synthesis of molybdenum oxo bis(dithiolenes) (Scheme 1.10). Although there are a variety of methods, many of them are restricted to very limited range of substituents patterns on the ligands. Perhaps the most general is the reaction of [Mo(O)(MeCN)₄Cl]⁺ with a deprotonated dithiolate.

Oxygen transfer catalysis has been demonstrated using these Mo(IV) salts, for example, in abstracting the oxo group from trimethylamine *N*-oxide.^{60,61} Related Mo(VI) systems can be used to carry out oxygen transfer to triphenyl phosphine stoichiometrically.⁶²

Derivatisation of Mo(IV) oxo bis(dithiolenes) has been used to form a variety of Mo(VI) complexes. The additional ligand introduced can be oxo, thio, seleno or the related alkoxides, etc.^{63–65}

Whilst the robustness of molybdenum oxo unit means that there is a choice of routes to introduce the dithiolene ligand, it is very difficult to remove the oxygen entirely. This hinders the potential of this route for producing oxo free complexes. Alternative approaches involve the use of transmetallation via nickel to molybdenum carbonyl precursors (Scheme 1.10). The resulting complexes are more readily

derivatised. This approach is covered in detail in Chapter 3.



Scheme 1.10: Synthetic pathways to synthesise Mo(O)(dithiolene)₂ complexes. Modified with permission from reference [48]. Copyright © 2004 American Chemical Society.

1.6.3 Summary

Fundamental coordination chemistry of mono- and bis(dithiolene) molybdenum complexes is well established. The range of functional groups present in most of these systems is markedly limited. There remain significant challenges in elaborating the metal centre to mimic enzyme active sites completely. It is notable that in contrast to some other parts of biomimetic chemistry, the last decade has not seen an explosive of research in this area. This doubtless reflects the much steeper chemical challenge

posed by high valent molybdenum.

1.7 Activating formate

1.7.1 Formate as an energy vector

It is deeply concerning that the current rate of use of fossil fuel is unsustainable: both depletion of finite reserves and emissions from combustions are critical. Therein lies a pressing need to find more environmentally friendly alternatives. Energy production in the future is likely to depend upon a range of methods which may include solar, wind or geothermal approaches. These can provide electricity to the grid but in themselves can not replace all of our current energy consumptions. To do that, new energy vectors will be required: small molecules that can be produced efficiently, store energy, and be used ideally avoiding combustions.

There are several molecules which have been suggested to fill this role, including, dihydrogen, ethanol and formate. The idea of a hydrogen economy is promising and does not rely solely on direct use of hydrogen gas. Formic acid is potentially an attractive choice for hydrogen storage as it contains 4.4 wt% hydrogen and is relatively non-toxic.^{66,67} Formic acid can be produced reversibly from carbon dioxide and dihydrogen.⁶⁸



This equilibrium lies towards the gaseous product as expected.⁶⁹ In principle, therefore, formic acid can be used to release dihydrogen in a open system without a catalyst. However, formic acid can also break down to water and carbon monoxide. As such, production of high purity hydrogen for fuel cell use requires catalytic assistance.

1.7.2 Existing catalytic methods

Synthetic catalysts focus almost exclusively on decomposition of formic acid. Earlier efforts have centred on platinum group metals with the focus increasingly placed on ruthenium and iridium complexes.⁷⁰⁻⁷² Whilst there are highly successful systems in this area, we can not ignore the fact that they rely on precious metals. Development to the scale needed for a true hydrogen economy is therefore still dependent on the discovery of earth abundant alternatives.

A true closed cycle will of course require reversibility. One can achieve this by sacrificing either the efficiency or the selectivity of electrocatalysis, or again by using rare precious metals.⁷³ Nature has already solved this problem, with FDH operating reversibly, close to the thermodynamic potential and using only earth abundant elements. This is surely the direction in which we must look to find truly scalable solutions.

In this thesis two aspects of bio-inspired catalytic behaviour of molybdenum chemistry will be explored. Firstly by activating dinitrogen molecule bound to molybdenum centre supported by various carbenes and secondly by mimicking FDH active sites capable of reversibly interconverting CO₂ and formate.

Chapter 2

Molybdenum nitrogen complexes

2.1 Introduction

2.1.1 Modelling nitrogenases

Activating dinitrogen is a fundamentally important process for life. The challenge of activating the metal–metal triple bond can be appreciated by the enormous bond dissociation energy of 946 kJ mol^{-1} for $\text{N}\equiv\text{N}$. Interestingly, in nature, bacteria tackles this challenge with the help of a specific group of enzymes known as nitrogenase. Since the production of nitrogen-containing fertilizers is a major economic activity, replicating the nitrogen fixation process artificially is vital. The current commercially available process for nitrogen fixation, the Haber process, requires extremes of temperature and pressure for conversion of dinitrogen to ammonia, shown in Equation 1.1. Therefore, finding a catalytic system that does this job under a much milder condition is hugely attractive.

Synthetic chemists have been working on designing systems with Fe and Mo to find a suitable catalyst for nitrogen fixation. Exploring the chemistry of metals present in nitrogenase, (Fe, Mo) and finding new ways to activate dinitrogen mildly is therefore a scientific challenge with potential to have an enormous impact on the society. Fe complexes supported in a ‘clamp’ fashion by *N*-heterocyclic dicarbene

ligands have shown great potential for nitrogen fixation.⁷⁴ Whilst molybdenum pincer carbene chemistry is quite rare, the Ohki group has recently started exploring molybdenum monocarbene complexes. In addition to ‘pincer’ biscarbene systems, we were therefore interested in the potential of homoleptic monodentate carbene complexes.

2.1.2 Carbenes and *N*-heterocyclic carbenes (NHCs)

Carbenes are neutral compounds featuring divalent carbon atoms with six electrons in their outer shell. The carbene carbon has a lone pair that is used to bind to transition metals via σ donation. The carbon atom in *N*-heterocyclic carbenes is stabilised by π -donation of the nitrogen lone pairs into the empty orbital of the carbon as shown in Figure 2.1.

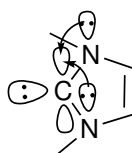


Figure 2.1: π stabilisation of NHC.

The stability and reactivity of *N*-heterocyclic carbenes were first investigated by Wanzlick⁷⁵ in the early 1960s. A few years later in 1968, the first application of NHCs as ligand was reported independently by Wanzlick⁷⁶ and Öfele.⁷⁷ The first successful attempt to isolate a stable crystalline free NHC, **25** (Figure 2.2), was reported by Arduengo and co-workers in 1991.⁷⁸

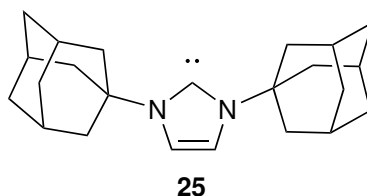


Figure 2.2: The first isolated carbene.⁷⁸

The carbene **25** features an imidazole backbone with an adamantyl group on each

of the two nitrogen atoms. The isolation of the ‘free’ carbene is mainly attributed to π donation of electron density from the nitrogen atoms to carbon, stabilising the formally divalent carbene carbon.⁷⁹ The stabilisation by π donation allows the NHCs to act as two electron donors, analogous to phosphines. Carbenes are stronger σ donor than PPh_3 .⁸⁰ The lower CO stretching frequencies of Mo–CO complexes stabilised by NHC suggests stronger σ donating properties relative to their phosphine analogues.⁸¹

N-Heterocyclic carbenes are capable of strongly coordinating to a wide variety of transition metals and stabilise a broad range of oxidation states. A number of useful catalytically active species containing monodentate carbenes have been developed; one of the most notable being Grubbs second generation catalyst, **26** (Figure 2.3) for metathesis.⁸²

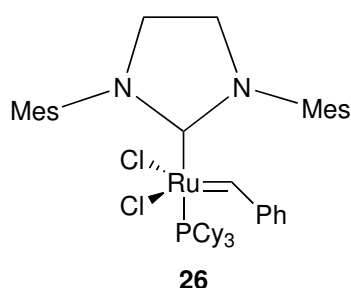
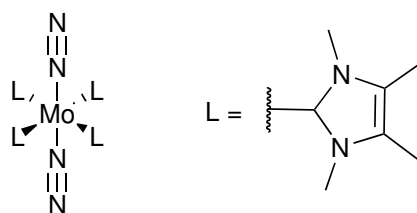


Figure 2.3: Grubbs 2nd generation catalyst.⁸²

2.1.3 Molybdenum *N*-heterocyclic carbene complexes

Ohki and co-workers have reported *NHC*-supported Mo(0) dinitrogen complex, **27** (Figure 2.4) in 2015.⁸³ As a result of strong σ -donation from the *N*-heterocyclic carbene to the molybdenum, this complex exhibited longer N≡N bond length, shorter Mo–N bond length and lower N≡N stretching frequencies compared to their corresponding phosphine analogues.⁸³ Ohki and co-workers have found that the asymmetric stretching frequencies of N≡N in NHC stabilised Mo–N₂ complexes are significantly lower, (1836–1838 cm⁻¹)⁸³ than their phosphine counterparts (1906–2004 cm⁻¹).^{84,85}

The lower frequency is the result of stronger electron donating property of the NHCs, leading to greater back-bonding and weakening N≡N bond. Therefore, it was no surprise that the N₂ in Mo-NHC was more basic and undergoes protonation by H₂O to form NH₃ whereas the corresponding phosphine stabilised Mo-N₂ complex shows no such reaction.⁸³ Interestingly however, phosphine supported tungsten complex, *cis*-W(N₂)₂(PMe₂Ph)₄ reacts with H₂O at 50 °C to produce NH₃.⁸⁶

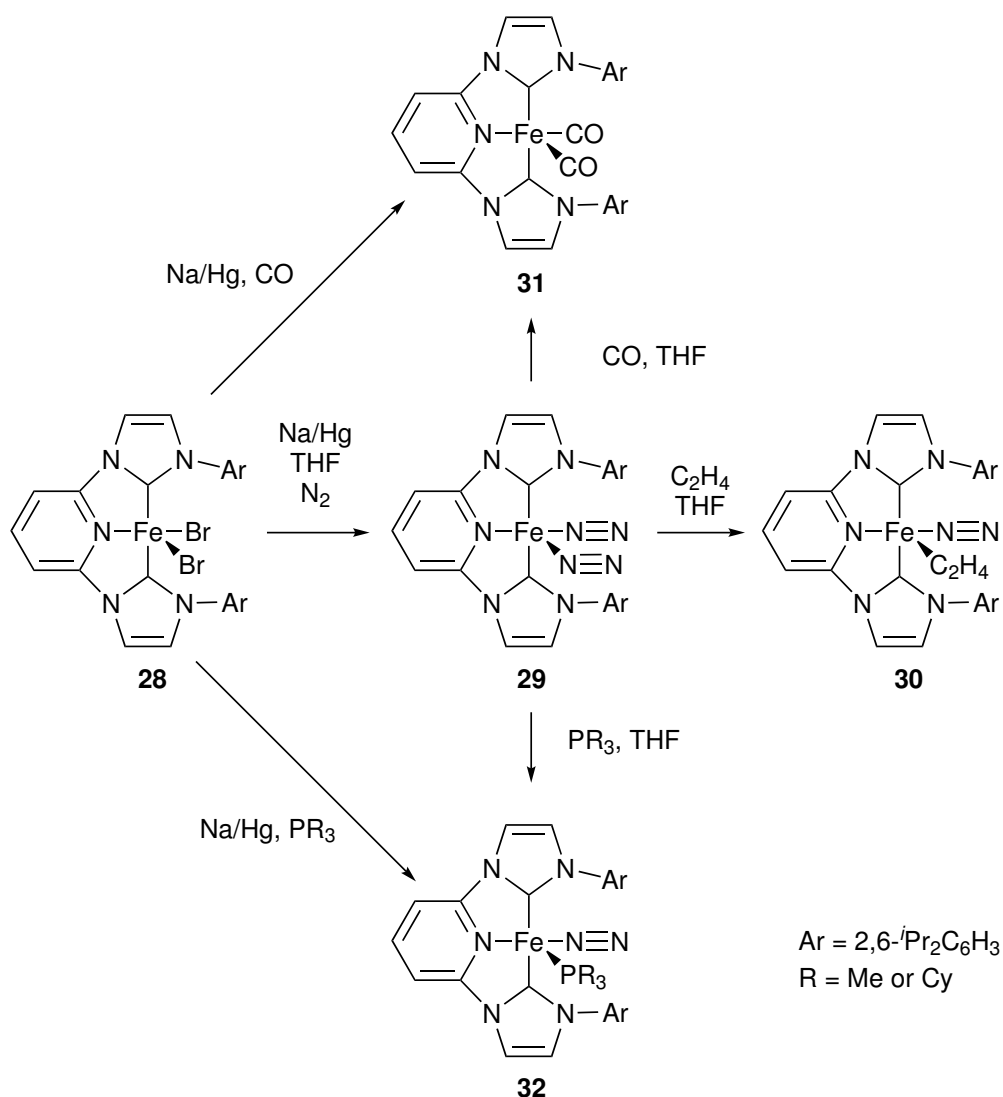


27

Figure 2.4: *N*-heterocyclic carbene supported Mo(0) dinitrogen complex reported by Ohki in 2015.⁸³

2.1.4 *N*-Heterocyclic pincer complexes

The Danopoulos group pioneered synthesis of metal complexes with *N*-heterocyclic pincer dicarbene ligand.⁸⁷ They reported the first Fe(0)-N₂ complex stabilised by an *N*-heterocyclic ligand, **29** in 2005 (Scheme 2.1).⁷⁴ Reduction of **28** with excess Na/Hg in THF under N₂ yielded **29**. Complex **29** exhibits a distorted square pyramidal geometry in the solid state with one apical and one basal end-on ligand.⁷⁴ X-ray diffraction revealed the N≡N bond length to be slightly longer than in free N≡N.⁷⁴ Although NHCs are stronger σ donors than phosphines, the infrared stretching frequencies of the bound dinitrogen molecule are higher (2109–2031 cm⁻¹)⁷⁴ than those observed for Fe(N₂)(P-P)₂ complexes (1950–2068 cm⁻¹).⁸⁸ This indicates a lower degree of back bonding than originally envisaged. The presence of a weak band at 2044 cm⁻¹ in infrared spectrum suggests an equilibrium between square pyramidal and trigonal bipyramidal structures in solution.⁷⁴ Complex **29** can be used



Scheme 2.1: Fe pincer dicarbene complexes.⁷⁴

as a convenient precursor for the synthesis of other Fe stabilised pincer dicarbene complexes, for example, **30–32**.⁷⁴

The Danopoulos group have also synthesised a variety of pincer dicarbene stabilised metal complexes in higher oxidation states including Ti(IV), V(II) (**33**, Figure 2.5), Cr(II), Mn(II), Nb(III) and U(IV).⁸⁹ Research by Gibson and co-workers showed that Cr(III) can also be stabilised by pincer NHCs, **34**, Scheme 2.2.⁹⁰

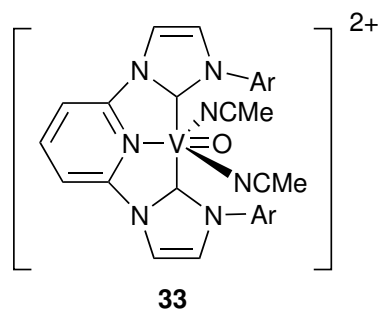
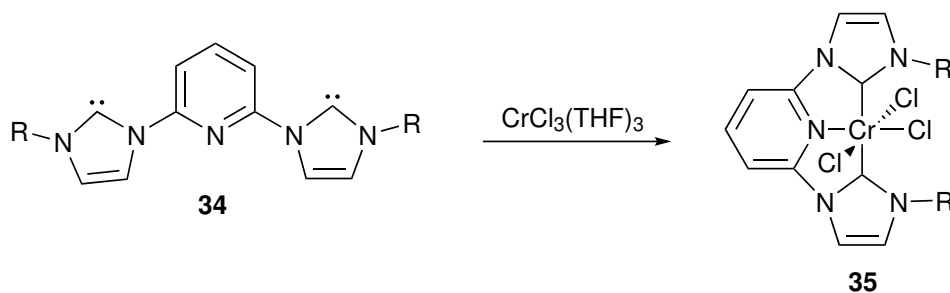


Figure 2.5: V(II) supported by *N*-heterocyclic dicarbene, where Ar = 2,6-*i*Pr₂C₆H₃.⁸⁹



Scheme 2.2: *N*-heterocyclic dicarbene supported Cr(III) complex, where R = *i*Pr, 2,6-*i*Pr₂C₆H₃, 1-adamantyl.⁹⁰

2.1.5 Molybdenum pincer complex

Although molybdenum is one of the metals present in nitrogenase, synthetic studies concerning molybdenum complexes with carbene and pincer ligands are still at its infancy. Ohki⁸³ group have studied mono metallic Mo-NHC complex for N₂ activation. Nishibayashi^{38,39} group have reported Mo-PNP pincer complex with potential to reduce dinitrogen. Studies into monometallic molybdenum pincer complexes has only recently begun to be explored by Bernskoetter in 2013.⁹¹ Mo pincer chemistry is still very under-explored and research into polydentate Mo pincer dicarbene chemistry 'hardly exists'.

2.1.6 Functionalised bis(phosphines) ligands

As detailed in Chapter 1, Chatt-type complexes featuring bidentate phosphines have been widely explored as mononuclear models of molybdenum dependent nitrogenase. At the same time, work by Dubois, Helm and others has unveiled the catalytic

potential of bisphosphine ligands containing a central nitrogen atom, capable of acting as a proton relay.^{92–95}

These so called PNP ligands offer the potential to vary donacity and basicity by selection of R groups on the phosphorus and nitrogen atoms, respectively. This is perhaps best illustrated in the activity of square planar nickel bis(PNP) complexes which can be tuned for either proton reduction or hydrogen oxidation (Figure 2.6).

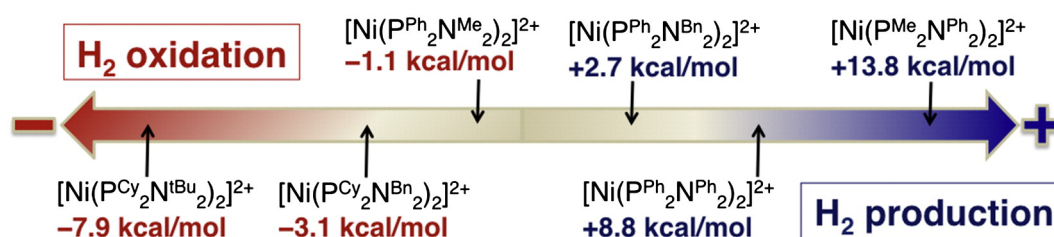


Figure 2.6: Catalyst tuning in Ni-PNP complexes, including free energy H₂ addition. Used with permission from reference [94]. Copyright © 2013 Elsevier

2.1.7 Molybdenum PNP complexes

Combining the Chatt chemistry with the proton relay ability of PNP ligands has potential to create powerful nitrogen activation catalyst. The Mock group have explored this chemistry with Cr, Mo and W centres.^{96–99} Mock established that in situ reductions of MoX₃(THF)₃ in the presence of a range of PNP ligands yields the trans bis nitrogen complexes (Figure 2.7).

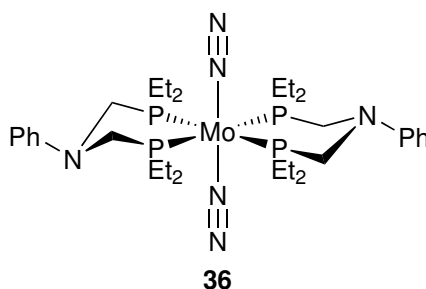


Figure 2.7: Example Mo-PNP complex.

Mock has explored the protonation chemistry of these systems in order to establish their viability as nitrogen activation catalyst. Using in situ infrared (IR) at low

temperature Mock was able to establish that protonation occurs at the metal and at the bound N_2 before protonation at the amine. Low temperature nuclear magnetic resonance (NMR) of ^{15}N labelled systems was used to probe this reaction further.⁹⁹

To allow the amine to approach the bound dinitrogen more closely, Mock has designed two flexible amines on one of the phosphorus atoms (Figure 2.8). To prevent these flexible groups approaching the metal too closely, the R groups were chosen to be sterically bulky irrespectively of their electron donor properties. These complexes show no evidence for metal protonation whilst retaining their ability to activate the terminal position of the dinitrogen ligand.

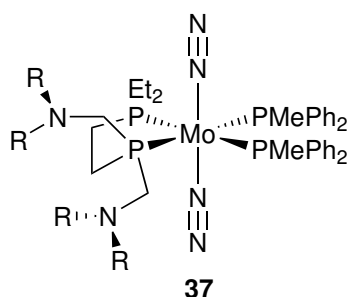


Figure 2.8: Example Mo-PNP complex.

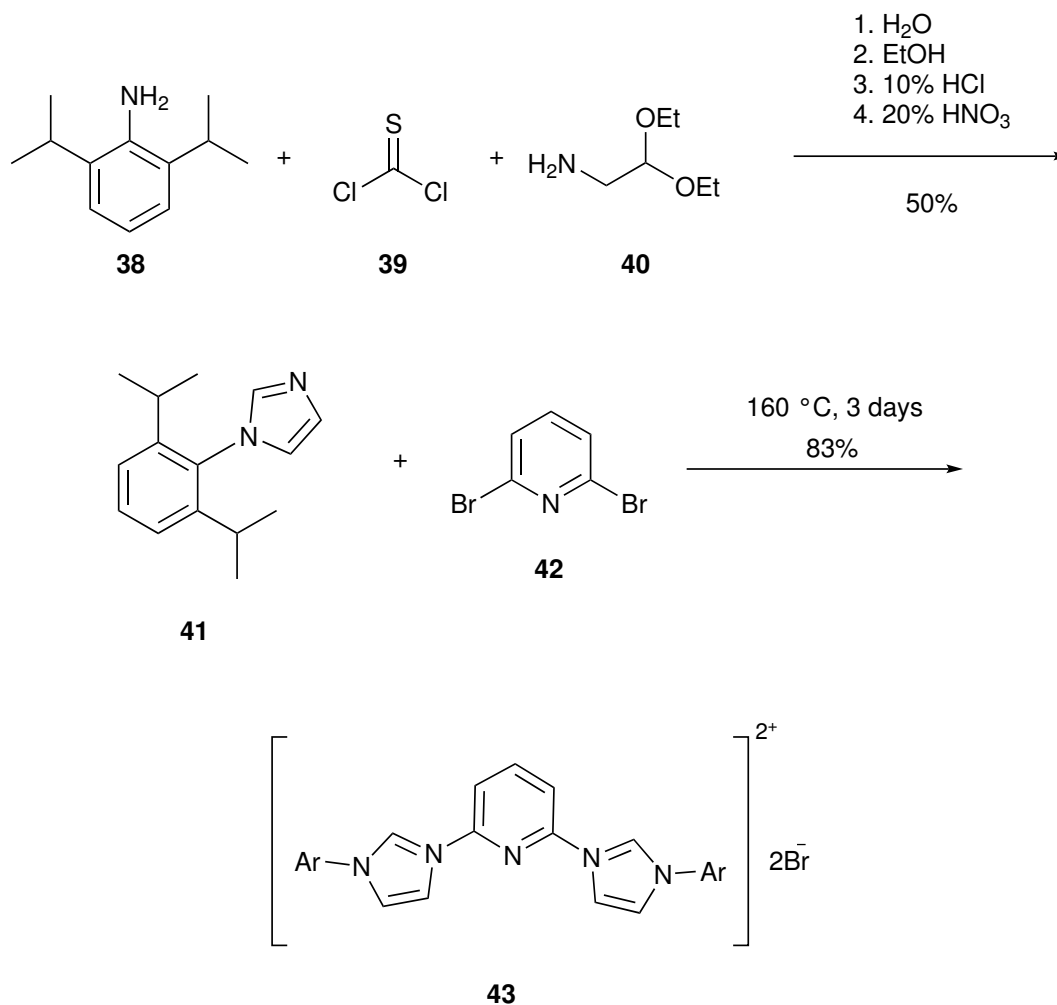
2.1.8 Our approach

This chapter covers work toward two classes of molybdenum nitrogen complexes. The first part details efforts to synthesise novel molybdenum complexes containing *N*-heterocyclic carbene ligands. The second part describes efforts to access complexes bearing bidentate phosphine ligands containing integrated amine bases. This work was motivated by careful consideration of the structure-activity relationship reported by Mock.^{96,97,99}

2.2 Molybdenum NHC complexes

2.2.1 Synthesis of imidazolium salts

Synthesis of the target ‘pincer’ bis(carbene) ligands requires access to aryl-substituted imidazoles **41**. These were prepared following the method reported by Johnson (Scheme 2.3).¹⁰⁰ Thus, reaction of aniline **38** with thiophosgene proceeded to give the related isothiocyanate. Nucleophilic attack on this by the amine **40** gives the thiourea derivative. Unmasking the protected aldehyde under acid conditions leads to ring closure to the mercaptoimidazole. Finally, oxidation using nitric acid generates imidazole **41**.



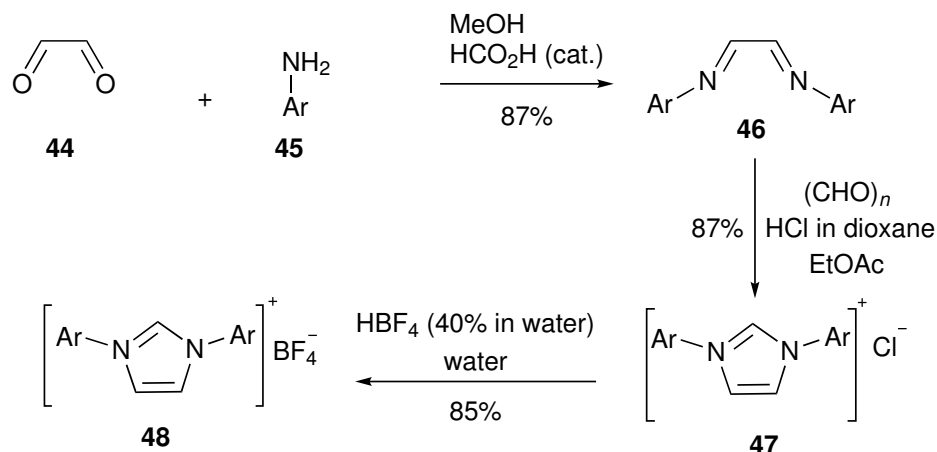
Scheme 2.3: Synthesis of diimidazolium salt **43** (Ar = 2,6-*i*-Pr₂C₆H₃).

The subsequent quaternisation reaction required implementing very high temperatures due to the stability of the aromatic ring. This reaction was carried out following methods reported by Danopoulos.⁸⁷ The imidazole and dibromopyridine, both (off)white solids, were heated to 140 °C in a closed vessel for 4 days. Unfortunately, the reaction did not go to completion in this time, with yield of only 42%. A higher yield, 65%, was achieved if the reaction was run for 6 days at 140 °C. Under these conditions, the reaction mixture at the end of the heating period was dark-brown/black viscous liquid. A more acceptable yield (83%) was achieved when the reaction was run at 160 °C for 3 days. At the end of the this time, the reaction mixture was a brown lumpy solid. The salt was dissolved in dichloromethane and precipitated out with diethyl ether. As the salt was very hygroscopic, azeotropic distillation in toluene was used to remove water. Refluxing the crude salt in toluene had the advantage of dissolving unreacted starting materials, which could then be removed via hot filtration. The presence of free imidazole is suspected to inhibit carbene **34** formation in the following step, so this was an important consideration.

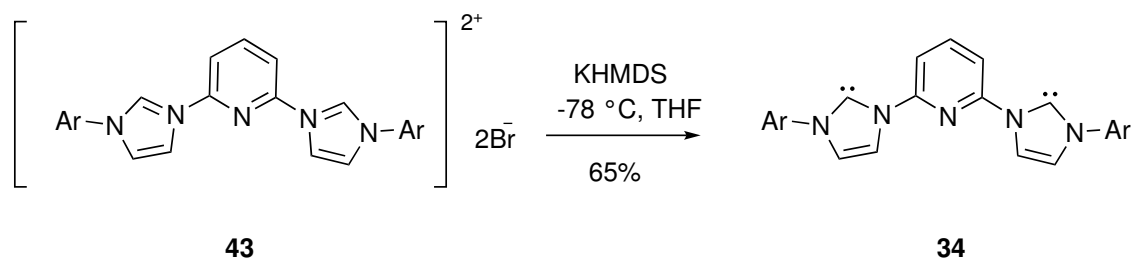
Monodentate carbene precursors were prepared following established methods (Scheme 2.4).¹⁰¹ Thus, after formation of the diazabutadiene, **46**, in good yield, formation of IMes-HCl, **47** was achieved by stirring with paraformaldehyde under acidic conditions. The use of HCl in dioxane allows the product to precipitate out; reaction with aqueous HCl yields a brown liquid instead of a white/cream solid, which is more challenging to purify. Anion exchange was facile; deprotonation of **48** was expected to yield a much cleaner carbene than the corresponding chloride salt. Deprotonation occurred smoothly to give the target material in good yield (85%).

2.2.2 Synthesis of free carbenes

The pincer dicarbene **34** was synthesised by deprotonation of salt **43** with the strong sterically hindered base potassium hexamethyldisilane (KHMDs) following standard literature procedure (Scheme 2.5).⁸⁹ The crude ligand was used directly



Scheme 2.4: Synthesis of monoimidazolium salt (Ar = 2,6-*i*Pr₂C₆H₃ or 2,4,6-Me₃C₆H₂).¹⁰¹



Scheme 2.5: Synthesis of the pincer carbene (Ar = 2,6-*i*Pr₂C₆H₃).⁸⁹

in subsequent reactions; purification attempts led to decomposition, and NMR spectroscopy demonstrated that the crude material was sufficiently pure to use as-synthesised (Figure 2.9). The presence of two doublets in the aromatic region, along with loss of the signal for the acidic C2 proton (Figure 2.10), confirmed formation of the free carbene.

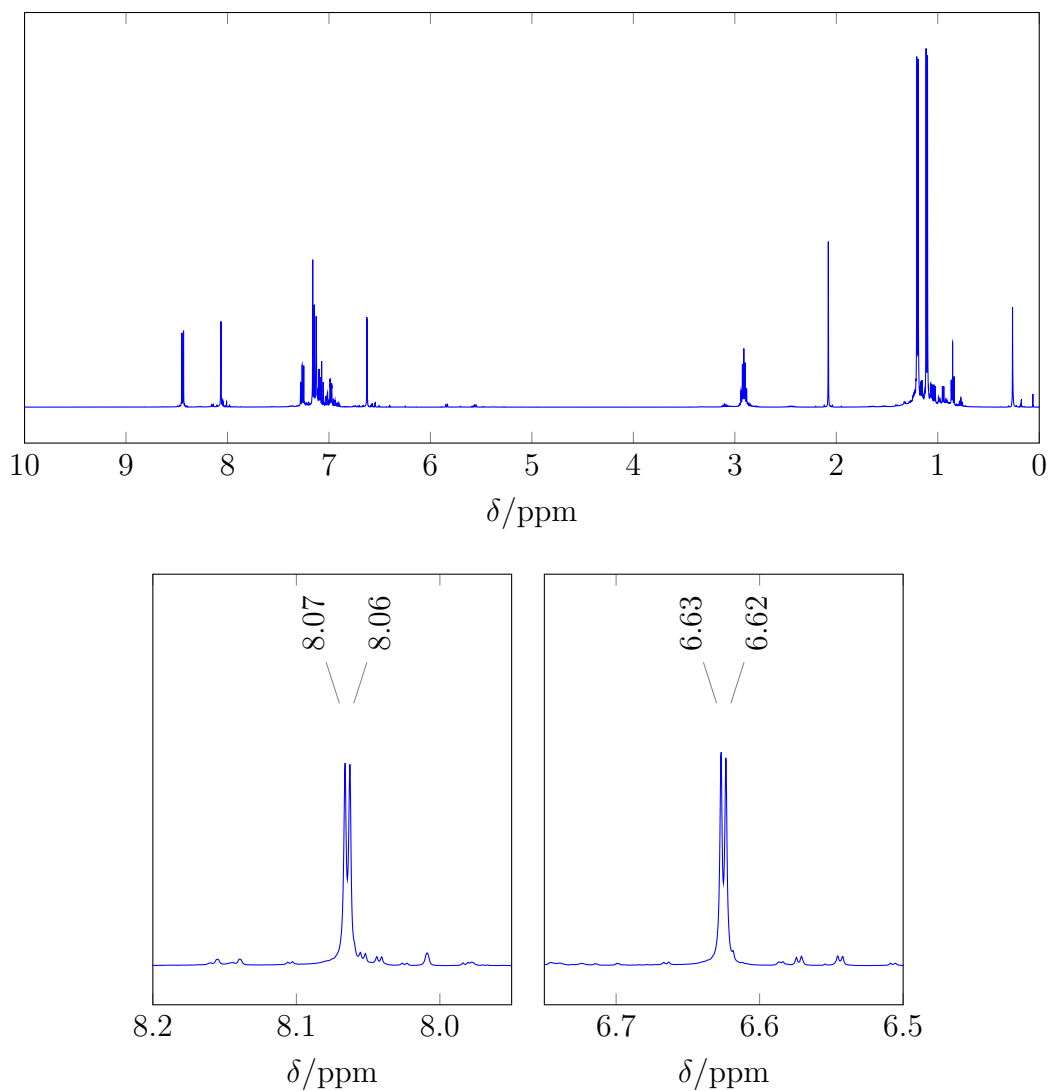


Figure 2.9: ^1H -NMR Spectrum of pincer dicarbene **34**; (top) Full spectrum; (bottom) expansions showing imidazole ring positions 4 and 5.

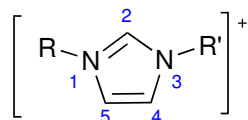
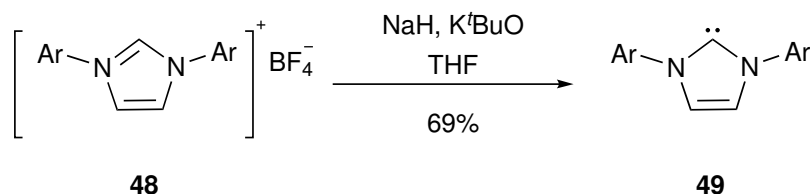


Figure 2.10: Generic structure of an imidazolium salt showing the atomic numbering

The monocarbene, **49**, was synthesised via deprotonation of oven dried IMes-HBF₄ by anhydrous sodium hydride in presence of potassium *tert*-butoxide catalyst (Scheme 2.6). This yielded the expected cream solid in good yield.



Scheme 2.6: Synthesis of monocarbene (Ar = 2,4,6-Me₃C₆H₂).¹⁰¹

2.2.3 Synthesis of molybdenum starting materials

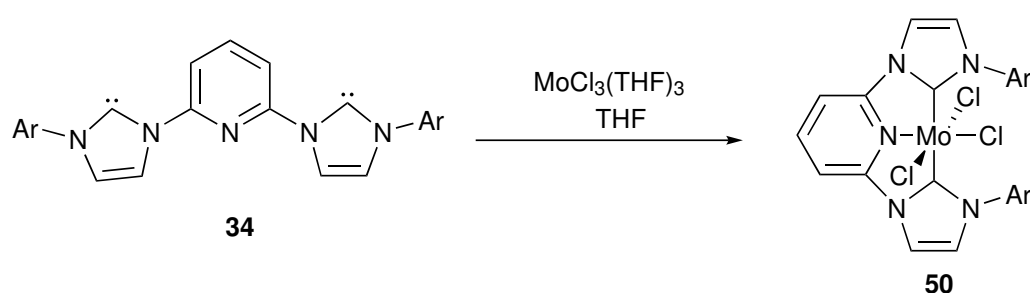
The purity of MoCl₃ · 3 THF is hard to determine: the complex is paramagnetic and offers no distinctive infrared bands. The routine method for determining the utility of material is therefore the colour of the solid; this is known to be beige in fresh samples.¹⁰² Stock of MoCl₃ · 3 THF in the laboratory was mustard-coloured, and fresh material was therefore prepared.

MoCl₃ · 3 THF was prepared from MoCl₅ in two steps following the procedure proposed by Poli.¹⁰² As MoCl₅ is a strong Lewis acid and a powerful oxidant, direct reduction in THF causes acid-catalysed ring opening polymerisation of THF.¹⁰² MoCl₅ was reduced to MoCl₄(OEt₂)₂ by metallic tin in ether and then reduced to MoCl₃ · 3 THF using tin granules in THF. The beige powder (like brick dust) was afforded in 63 % yield.

2.2.4 Exploring carbene complex synthesis

Ohki has synthesised Mo-N₂ complexes supported by monocarbene ligands using Mo(IV). They have carried out metal complexation and coordination of N₂ in a single step from MoCl₄ · 2 THF.⁸³ A similar approach was taken to seek access to Mo(III) complexes.

MoCl₃ · 3 THF was added to a solution of pincer dicarbene (**34**) in THF and stirred overnight to give a red-brown solution (Scheme 2.7). The putative product, **50**, was precipitated out with hexane and filtered. However, the precipitates were too fine and went straight through the filter frit. The resulting suspension was left standing overnight to allow the precipitate to settle. This gave a pink-red solution, from which dark red solid formed at the edge of the Schlenk flask. The solution was decanted and the solvent removed under vacuum. Attempts to grow single crystals by for example layering concentrated THF solutions with hexane were unsuccessful.

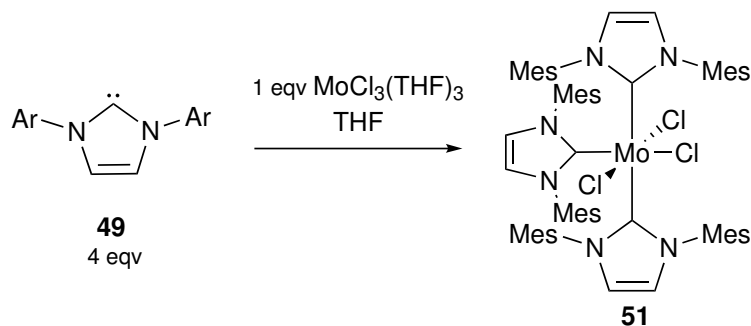


Scheme 2.7: Synthesis of Mo-pincer carbene complex (Ar = 2,6-^{*i*}Pr₂C₆H₃).

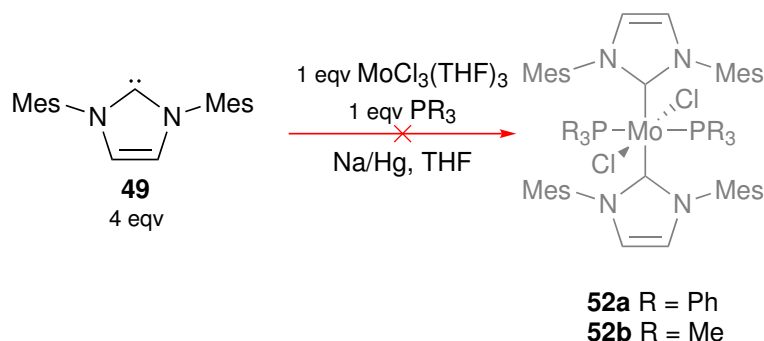
One equivalent of MoCl₃ · 3 THF was added to a solution of four equivalents of **49** in THF and stirred overnight to give a brown solution (Scheme 2.8). The putative product, **51**, was precipitated out with hexane as a brown solid formed from an orange solution. The precipitate was filtered and dried to afford a light brown solid. ¹H NMR spectroscopy revealed almost identical peaks to that of the the ligand **49** with a slight downfield shift. As the desired Mo(III) product would be paramagnetic, this suggests it is unlikely that significant amounts are present.

2.2.5 Toward mixed phosphine–carbene complexes

As molybdenum centres supported purely by *N*-heterocyclic carbene ligands could not be identified in a definitive way, the decision was made to explore routes to mixed phosphine–carbene systems. The general approach taken in this work is show in Scheme 2.9



Scheme 2.8: Synthesis of Mo-monocarbene complex (Ar = 2,4,6-Me₃C₆H₂).



Scheme 2.9: Synthesis of Mo carbene phosphine complex.

To attempt the synthesis of **52a**, MoCl₃(THF)₃ in THF was added to a solution of IMes in THF. This formed a dark red/brown solution. PPh₃ was added to the reaction solution before the reaction was transferred into a flask containing sodium amalgam to reduce Mo(III) to Mo(II) *in situ*. With a mixture of two donor ligands available, the stoichiometry of the putative product is speculative. Based on steric considerations, we anticipated that a maximum of two **49** ligands would bind to the metal in the presence of phosphine. The reaction was stirred for three days, whilst monitoring for IR peaks for any bound nitrogen after further reduction. No IR bands for this group were observed, and so the reaction was worked up after three days by decanting from the mercury and filtering through Celite. After removal of the solvent, the red residue was extracted with toluene and filtered through Celite for a second time. Layering with hexanes yielded a light orange solid, which on washing with further hexane and drying at reduced pressure became cream.

A similar approach was take using the more basic phosphine PMe₃, targeting

complex **52b**. This reaction gave a greenish brown solution, which again showed no signal for a bound nitrogen in the IR. The reaction mixture was worked up by filtering through Celite and removing solvent, before extracting it with toluene and filtering with Celite for a second time to give an olive green solution. Layering with hexane afforded a light yellow supernatant and a yellowy cream solid. Decanted the supernatant carefully without removing any solid, washed with hexane and dried under vacuum to yield a cream solid.

Visually, both of these reactions appeared to yield unreacted free carbene. This approach was therefore discontinued.

2.2.6 Summary

Attempts to access carbene-containing Mo(II)/Mo(III) complexes, either alone or supported by phosphines, were not successful. The challenge of accessing these systems is possibly due to the oxidation state targeted.

2.3 Molybdenum N₂ complexes bearing PNP ligands

2.3.1 Background

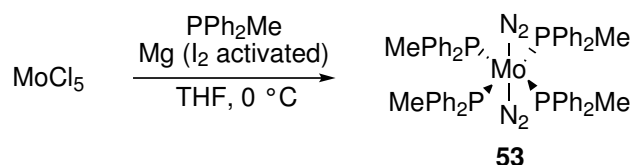
Whilst molybdenum *N*-heterocyclic carbene complexes supporting N₂ are extremely challenging to access, there are a large family of Chatt-type Mo(N₂)₂(PR₃)₄ complexes which feature mono-, bi- or tetradentate phosphines. We were particularly attracted in this area to systems features PNP ligands, in which a bis(phosphine) system contains a central amine, capable of acting as a proton relay to the bound dinitrogen.

As described above, Mock has explored the nitrogen activation ability of a range of molybdenum PNP complexes. Whilst Mock has reported both synthesis and protonation studies with both electron donating and electron withdrawing groups at

nitrogen, he has reported less variation at phosphorus. In particular, it is unclear to what extent changes in protonation chemistry can be attributed to change of a single substituent on phosphorus. Crucially, there is no published data in which electron rich phosphines are combined with simple alkyl and aryl groups at nitrogen. We therefore decided to pursue insight into exactly how these complexes behave under protonation conditions.

2.3.2 Synthesis of $\text{Mo}(\text{N}_2)(\text{PPh}_2\text{Me})_4$

Access to the target Mo-PNP complexes takes place via the precursor **53**. This material is synthesised directly from MoCl_5 under reducing conditions in the presence of the phosphine (Scheme 2.10).



Scheme 2.10: Synthesis of molybdenum dinitrogen tetrphosphine complex **53**.

Initial attempts to access this compound were severely hampered by yields in the region of 20%. Although an infrared peak was observed for the bound N_2 at 1929 cm^{-1} in reaction mixture, attempts to isolate it resulted in impure brown solid instead of a bright orange solid as expected from the literature. Therefore, various modifications were tried to improve the yield of the reaction.

Activation of magnesium was first carried out by stirring the dry solid under nitrogen overnight. The first improvement attempted was to activate the magnesium by heating it gently with iodine. Reactions involving Mg turnings are often accelerated by vigorous stirring.¹⁰³ A mechanical stirrer was used to facilitate most efficient saturation of nitrogen into the reaction mixture. These steps did not make a significant difference to the outcome of the reaction.

The final modification in the reaction set-up was use of a mercury bubbler. This

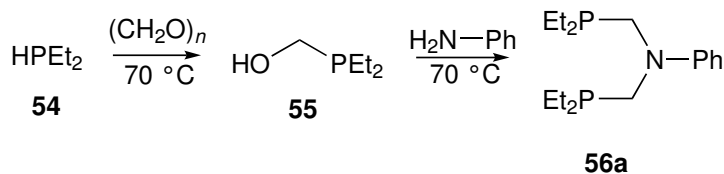
reaction was carried out under nitrogen pressure supported by a mercury bubbler: use of a silicon oil bubbler just did not generate enough pressure to keep the reaction mixture fully under nitrogen environment. Whilst nominally Schlenk apparatus operates under an atmospheric pressure of inert gas, the real internal pressure is dependent upon experimental setup. A slight over-pressure is ensured by the use of a bubbler and the exact value of this over-pressure is dependent on the density and depth of the fluid in the bubbler. Typically the depth of the displaced fluid is the same, independent of the use of silicone oil or mercury. The higher density of mercury therefore means that the real over-pressure is higher in the presence of mercury bubbler. This final adjustment allowed us to successfully isolate the bright orange product in 63% yield giving the expected IR band at 1929 cm^{-1} and ^{31}P NMR signal at 19.41 ppm in benzene.

2.3.3 Synthesis of PNP ligands

As described above, the Mock group have explored a variety of PNP ligands bound to group 6 metals. Whilst they have employed a range of R groups at phosphorus, the most significant results have involved at least some alkyl substituents on the phosphorus atoms.^{97,99} Our interest was therefore centred on PNP ligands containing PEt_2 group.

A series of PNP ligands were synthesised following literature methods.^{98,104} The literature method for making the phenyl-substituted PNP ligand uses neat reagents, but exploits a small amount of ethanol in the preparation of the *tert*-butyl substituted PNP ligand.¹⁰⁴ Literature methods of synthesis for various other substitution on nitrogen also uses a small amount of ethanol as a solvent. Therefore, to test the efficiency of the this reaction ‘neat’ against in solvent, this reaction was repeated two more times in two solvents: ethanol and methanol. Scheme 2.11 shows the synthesis of phenyl substituted PNP, which was used at the model reaction.

The results are summarised in Table 2.1. The conversion was calculated by



Scheme 2.11: Synthesis of PN^{Ph}P.

integrating the area under the ³¹P NMR signal at -29.8 ppm for expected product against that for the starting material at -23.3 ppm in the crude reaction mixture. Whilst integration of ³¹P NMR has low accuracy, it is selective for the species of interest. In particular, there is no need to remove the solvent, in contrast to ¹H NMR spectroscopy.

As it is clear from the table, the reaction is most efficient in no solvent, achieving the highest conversion, to PN^{Ph}P. It is unsurprising that the conversion rate is lowest in methanol, as the reaction could only be heated to 60 °C due to reaching the boiling point of methanol.

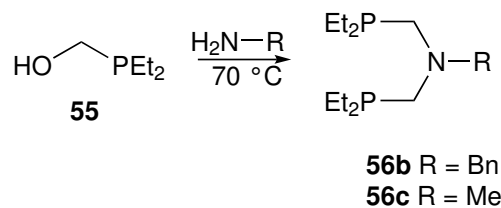
Table 2.1: Effect of solvent on the conversion of PN^{Ph}P.

Solvent	Temperature	Conversion
Neat	70 °C	78 %
Ethanol	70 °C	60 %
Methanol	60 °C	56 %

All reactions were for 16 hours; solution reactions were 0.56 M with respect to **55**.

The reactions were monitored by NMR spectroscopy and worked up when there were no further progress in conversion. Attempts were also made to increase the conversion by introducing additional equivalents of the amine during the heating stage. However, this did not seem to make a difference to the overall success of the reaction.

With the most efficient route to the ligand architecture established, attention shifted to the other desired substituent groups (Scheme 2.12). These were both obtained as colourless oils and were used without further purification. Purity was

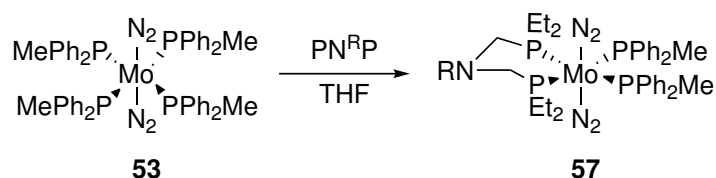


Scheme 2.12: Synthesis of $\text{PN}^{\text{R}}\text{P}$.

established by ^{31}P NMR spectroscopy. For ligand **56b**, the product peak was located at -34.5 ppm while for ligand **56c** it was located -33.5 ppm. In both cases, the purity established by NMR spectroscopy was 86 %.

2.3.4 Synthesis of mono(PNP) complexes

Ligand **56b** (1.2 eqv) in THF was added to a solution of one equivalent of complex **53** in THF to synthesise mono chelated molybdenum complex as shown in Scheme 2.13. Monitoring the reaction by IR, no change in the starting material was visible after 20 minutes, while after 100 minutes a small amount of the starting material could still be seen. The reaction was therefore left to stir overnight. After this time, the only N_2 peak visible was a new band at 1937 cm^{-1} .



Scheme 2.13: Synthesis of molybdenum mono(PNP) complexes (R = Bn, Me).

^{31}P NMR spectroscopy of the crude reaction mixtures showed three singlets around -20 ppm. This was quite inconclusive and it was difficult to identify any peaks with certainty. As fast exchange of bound and free phosphine was possible, low temperature NMR was carried out to obtain further information. This showed the presence of free phosphines in the crude solution. The reaction mixtures were therefore stirred with copper(I) chloride to remove the free phosphines.⁹⁷ After work-up by filtering it through a pad of neutral alumina, brown oils were obtained. ^{31}P

NMR spectroscopy of the reaction using **56b** showed two doublets at 7.25 ppm and 15.40 ppm (Figure 2.11). Layering the solution with ethanol yielded small amount of orange solid. However, this solid was extremely moisture sensitive and unstable, and further attempts to obtain product were hampered by decomposition during work-up.

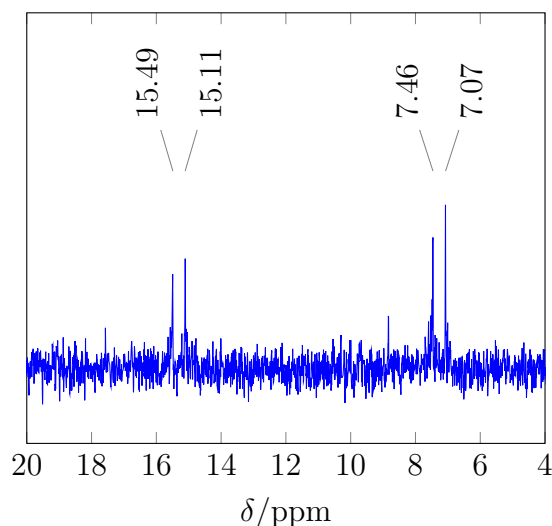


Figure 2.11: ³¹P-NMR spectrum of **57b**.

Reaction using ligand **56c** proceeded to give a product with IR peak at 1937 cm⁻¹ within 60 minutes. ³¹P NMR spectroscopy of the reaction mixture showed doublets at 9.75 ppm and 17.86 ppm, with ligand peak at -32.94 ppm and peak for free phosphines at -27.60 ppm (Figure 2.12). The orange brown residue was cleaned by stirring in a solution of CuCl in ether to remove excess phosphine and filtering through a column of neutral alumina. Removed the solvent from the bright yellowy orange filtrate to yield an orange solid.

Removal of the solvent gave a bright orange/brown oil which was filtered through neutral alumina. Layering with ether led to the formation of a small number of crystals suitable for X-ray analysis (Figure 2.13). This revealed that, surprisingly, the solid obtained comprised a mixture of **57c** and **58c** in a 2 : 1 ratio. The structure is otherwise unremarkable, with both complexes showing the anticipated *trans* disposition of N₂ groups and typical bond lengths and angles.

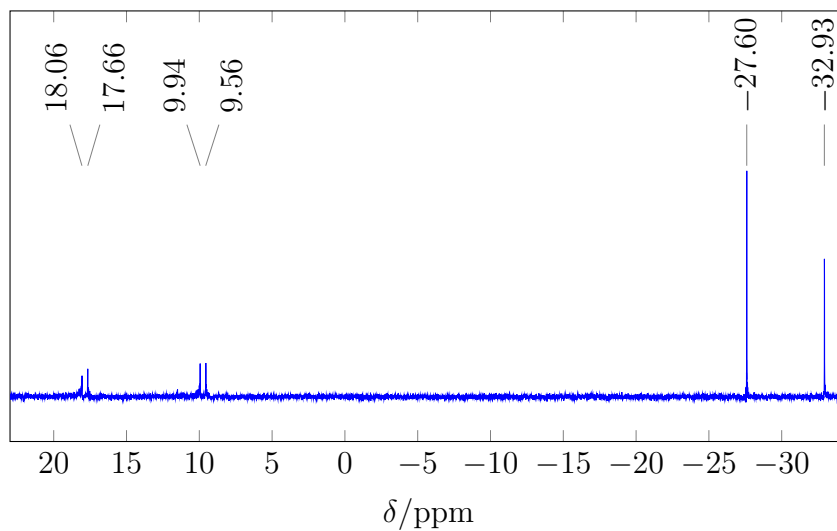


Figure 2.12: ^{31}P -NMR spectrum of **57c**.

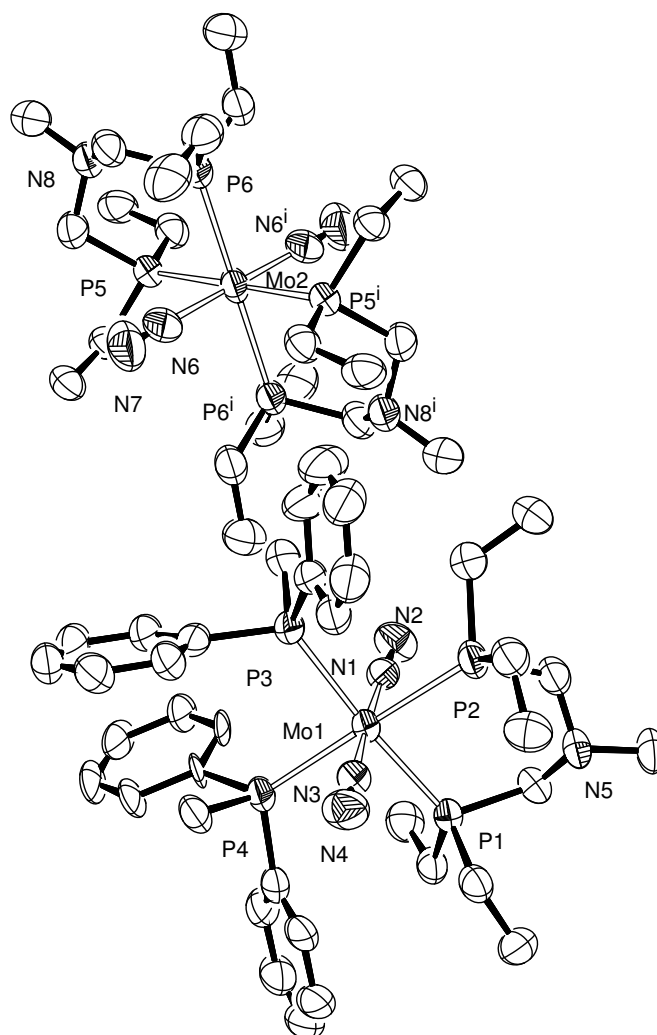


Figure 2.13: ORTEP representation of the structure of $2(\mathbf{57c}) \cdot \mathbf{58c}$ showing 50% probability ellipsoids; hydrogen atoms have been omitted for clarity.

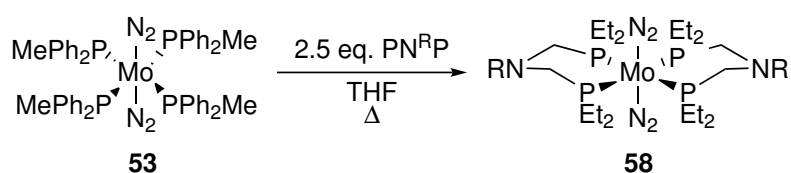
Reaction using **56a** gave a change in the bound nitrogen signal but did not exhibit the anticipated pair of doublets in the ^{31}P -NMR spectrum. As is detailed below, the bis ligand adduct is accessible: this may have formed preferentially even with the low ligand equivalence.

Whilst isolation of the mono(PNP) complexes was not successful, the IR evidence clearly showed that formation of novel N_2 species proceeded. Attention therefore switched to the bis(PNP) complexes, where the chelate effect is more pronounced and therefore isolation was anticipated to be more facile.

2.3.5 Synthesis of bis(PNP) complexes

Exploration of the synthesis of bis(PNP) complexes followed the same approach as described in Section 2.3.4 using twice the amount of chelating phosphine (Scheme 2.14).

Reaction using ligand **56a** at 60°C proceeded within one hour to give a bright brown solution showing a new peak in the IR at 1942 cm^{-1} . ^{31}P NMR spectroscopy showed no doublets (which correspond to mono(PNP) complexes), instead featuring a singlet at around 14 ppm as a minor component. The major signals in this spectrum corresponded to free phosphines. Removing solvent under reduced pressure yielded a brown oil; a pure solid could not be obtained from this material.



Scheme 2.14: Synthesis of molybdenum bis(PNP) complexes (R = Ph, Bn).

Again, reaction with **56b** was slower; after 80 minutes the starting material was still present although the IR peak was less intense than at the start of the reaction. After reaction overnight a single bound N_2 signal at 1941 cm^{-1} was present. In addition to free phosphine peaks, a single singlet at 8.8 ppm in the ^{31}P NMR spectrum was present, and consistent with formation of a bis(PNP) species.

2.3.6 Summary

Isolation of pure samples of the PNP complexes was not possible. A summary of the infrared data for all complexes positively identified is given in Table 2.2. Mono- and bis-phosphine complexes were only observable with ligand **56b**. This exhibits a small but real shift in the IR position of the bound N₂ when the two PNP ligands are present. This is surprising considering the additional electron-donating ability of the PNP ligands when compared to the PPh₂Me ligands present in the mono(PNP) systems. Alternatively, the coincident value for the IR stretches could be caused by the line broadening effect of the solvent. Polar solvents such as THF give significant broadening of IR stretches compared with lower polarity solvent such as heptane. This can lead to a loss of resolution.

Table 2.2: Comparison of IR frequencies for mono- and bis(PNP) molybdenum dinitrogen complexes.

R	$\tilde{\nu}_{\max}(\text{N}_2)/\text{cm}^{-1}$	
	Mono(PNP)	Bis(PNP)
Ph	–	1942
Bn	1937	1940
Me	1937	–

2.4 Conclusions

Attempts to isolate novel molybdenum N₂ complexes were met with limited success. Exploring routes to *N*-heterocyclic carbene systems, it became clear that the approaches undertaken were of limited utility in isolating useful materials. Little evidence for the desired bound N₂ states was obtained.

Formation of Mo(PNP) complexes was more successful, with novel ligands isolated and clear evidence for formation of the desired mono- and bis(PNP) species in solution. However, isolation of pure materials was problematic, possibly due to dynamic ligand exchange in solution. Further pursuit of this avenue was discontinued to allow focus

on other aspects of small-molecule activation using molybdenum centres.

Chapter 3

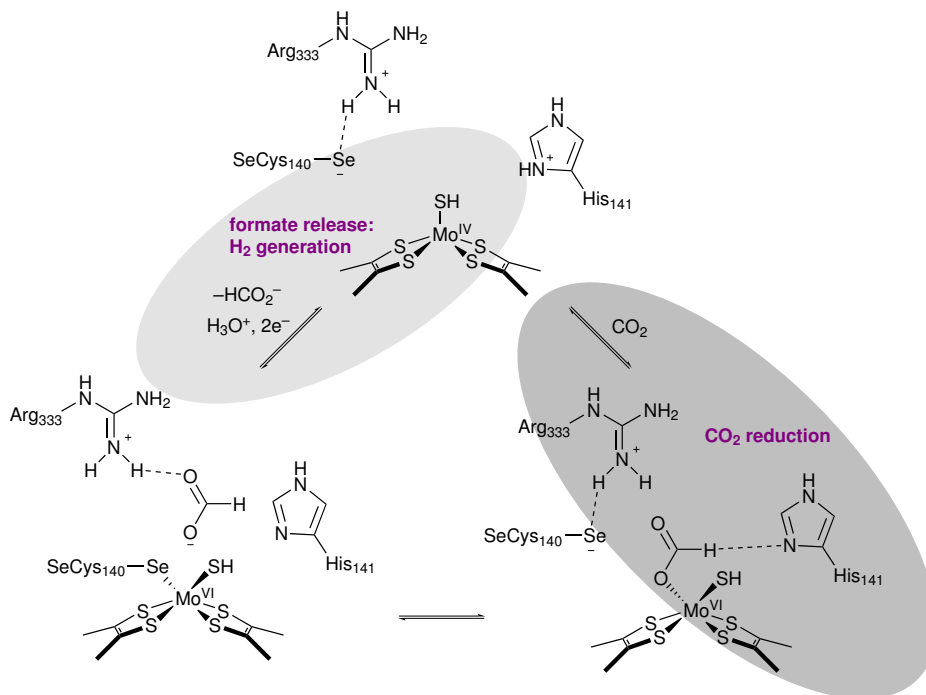
Synthesis of functionalised molybdenum dithiolene complexes

3.1 Introduction

3.1.1 Activity of FDH

In biological systems, FDH is capable of reversible reduction of CO₂ to formate. Metal-dependent FDHs are efficient in reversible electrocatalysis of CO₂ reduction.¹⁰⁵ There has been an increased interest over the past decade in using proton relays in synthetic systems to understand the catalytic cycle of FDH. A number of research groups have tried to mimic this biological system. It is highly disputed whether the primary molybdenum coordination sphere remains saturated during the catalytic cycle or one of the ligand dissociates to provide direct access to molybdenum centre during catalysis. Some authors believe that the metal bound selenocysteine (Sec) is hemi-labile while other groups suggest that the primary coordination sphere remains saturated throughout the catalytic cycle with a second coordination sphere mechanism that may involve hydride transfer.^{106,107} The mechanism for FDH catalysis is still under debate. One of the potential catalytic routes is shown in Scheme 3.1.

There are a very limited number of crystal structures available for FDH. These



Scheme 3.1: Potential catalytic cycle of FDH enzyme.

are of low resolution and cannot reveal either the charge on the metal or the redox state of the pterin ligand. Thus whilst significant progress has been reported in exploring the biological basis of FDH catalysis, access to active structural models will be essential in fully understanding how the enzyme functions.

3.1.2 Simple molybdenum dithiolenes

There are two types of dithiolenes as shown in Figure 3.1. Whilst various derivatives of **59** have been isolated, only a few derivatives of **60** are known. This might be due to the lack of an aromatic backbone to help stabilising the negative charges in the Sulphur.

The Holm group have done extensive research on synthesising the more complicated dithiolenes (**60**) with simple, symmetric R group as shown in Scheme 3.2.⁴⁸ Holm's work encompassed not only FDH models, but also extended to cover mimics of almost all molybdo- and tungsto- dithiolene enzyme active sites. In the synthesis of FDH analogues, Holm demonstrated that access to Mo(S)(dithiolene)₂ required

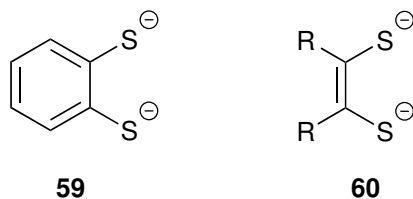
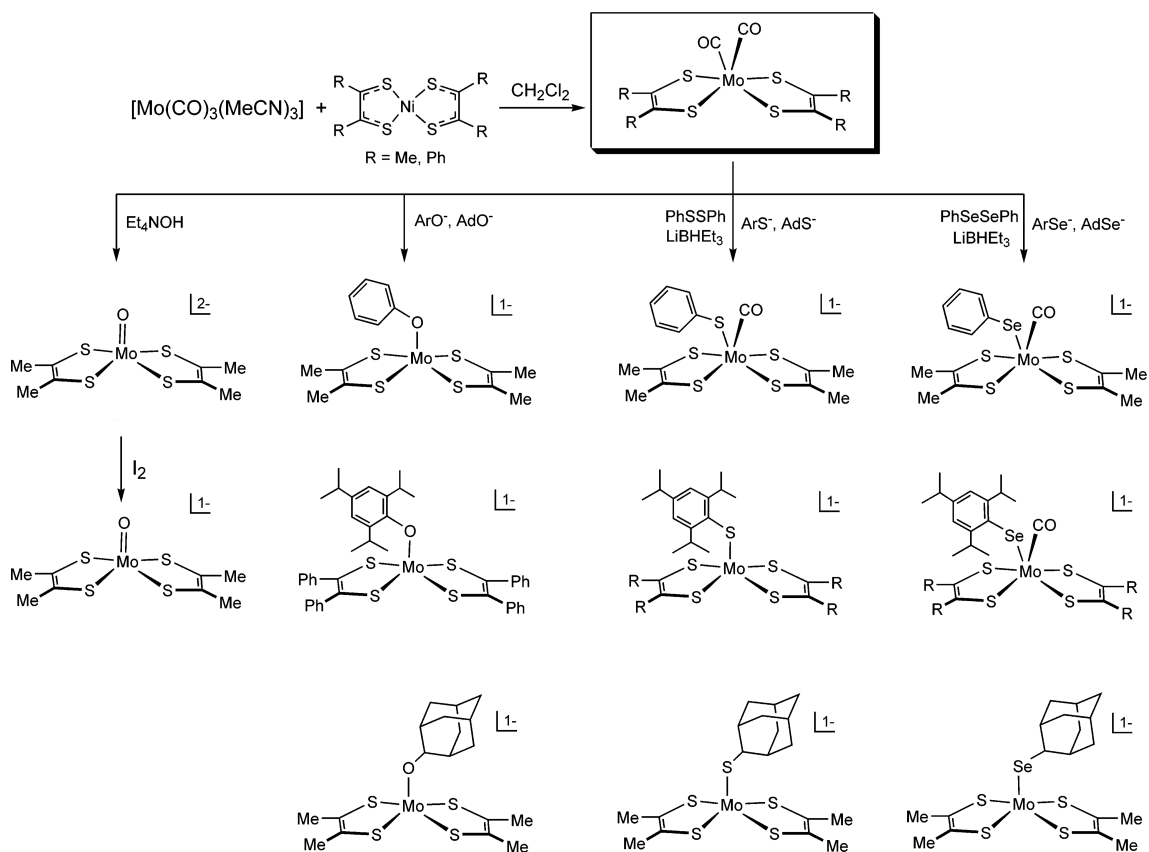


Figure 3.1: Two fundamental types of dithiolenes (In literature structures, R = H, Me, Ph, CN, CF₃).



Scheme 3.2: Synthetic pathways based on $[\text{Mo}(\text{S}_2\text{C}_2\text{R}_2)_2(\text{CO})_2]$ leading to oxo, desoxo, and thiolate and selenolate monocarbonyl bis(dithiolene) complexes. Modified with permission from reference [48]. Copyright © 2004 American Chemical Society.

reaction via the $\text{Mo}(\text{CO})_2(\text{dithiolene})_2$ precursor. Access to the latter have to date relied upon transmetalation from the equivalent square planar nickel precursors.^{108,109}

Exploration of the coordination chemistry of both molybdenum and tungsten by Holm has mapped out a good deal of the fundamental chemistry needed for biological modelling. However, these symmetrical systems featuring small non functionalised dithiolene ligands do not offer any catalytic potential. As such they can only be

regarded as the first generation of FDH mimics.

3.1.3 Functionalised mimics

The reactivity of molybdenum bis(dicarbonyl) complexes makes them challenging intermediates to synthesise. The ‘requirement’ to proceed via the nickel complexes means that there have been very limited attempts to produce more complex structures in this way. In contrast, molybdenum oxo dithiolenes are much more stable, and there are a variety of routes by which these may be formed (Scheme 1.10).

The Fontecave group has synthesised novel dithiolenes (Figure 3.2) which include a pyrazine ring fused with a pyran ring, carrying the dithiolene chelate.^{110,111} This mimics molybdopterin (MPT) present in the active site of FDH. They have subsequently used these dithiolene ligands to synthesise nickel bis(dithiolene) and molybdenum-oxo complexes, utilising the increased flexibility offered by the latter.

Whilst the nickel bis(dithiolene) complexes showed the potential to act as an efficient and stable catalyst for electroreduction of CO₂, the corresponding molybdenum oxo bis(dithiolene) complexes successfully catalysed the reaction with 100 turnovers in 8 hours. This was not only the first reported functional Mo(O)(bis-dithiolene), but also found to be catalytically active.

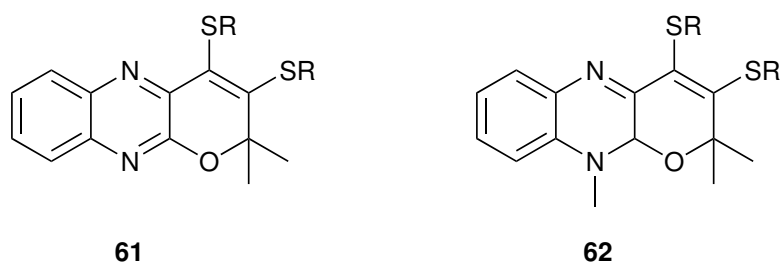


Figure 3.2: Functionalised dithiolenes synthesised by the Fontecave Group.^{110,111}

Although Fontecave uses a biomimetic ligand system, it does not introduce functionality proximal to the metal centre. Whilst the redox activity of the pterin ligand appears important, the lack of proton relay groups likely limits its catalytic

activity. Moreover, the plain nature of the pterin system makes it challenging to both introduce proton relays and retain the full heterocyclic ligand.

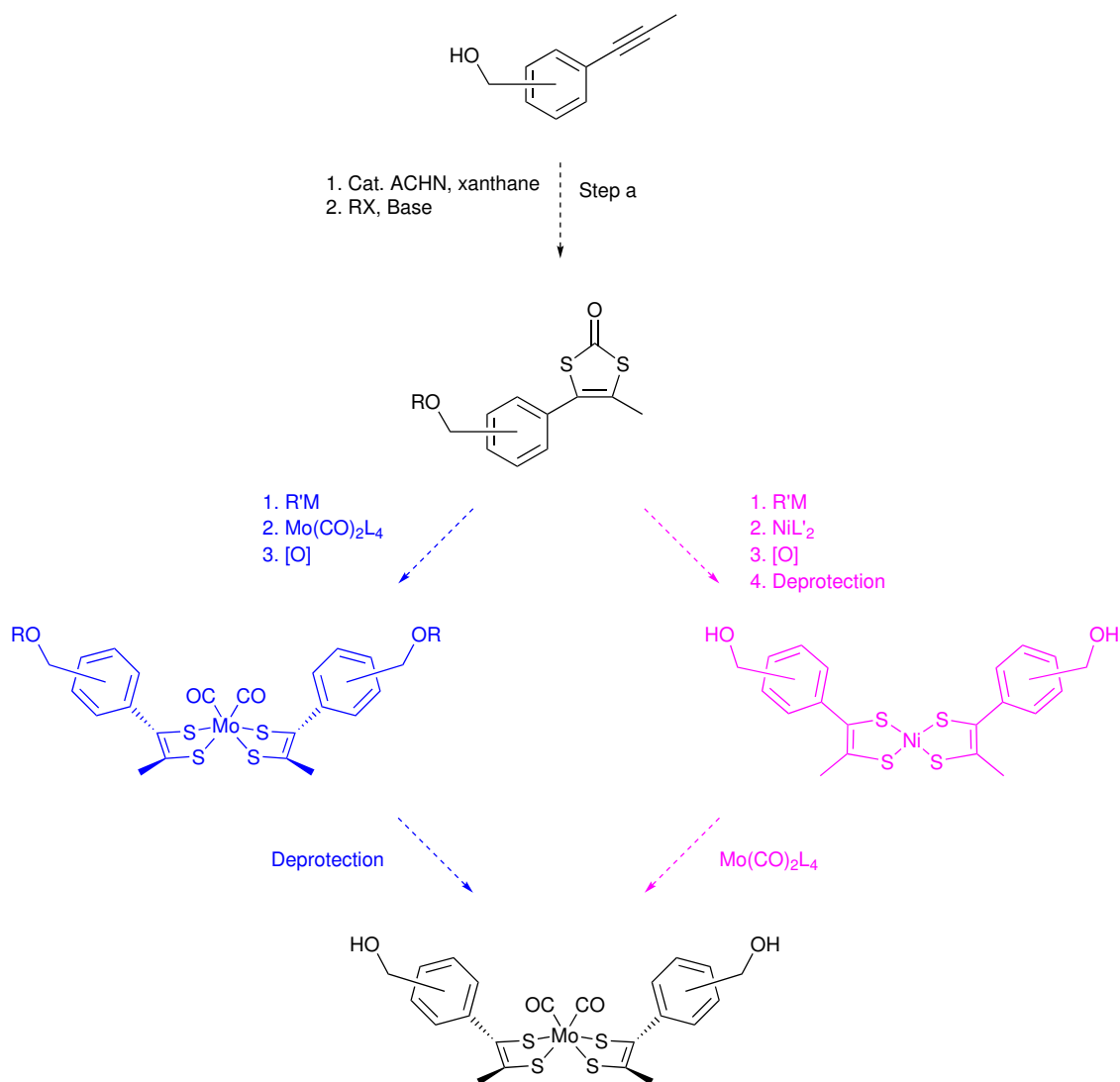
3.1.4 Our synthetic strategy

As detailed above, there have recently been significant progress in producing functional models of the FDH active site. However, it remains the case that none of these molecular systems is capable of reversibly interconverting CO₂ and formate. We have therefore decided to explore this still under-explored area of chemistry.

In common with many other metalloenzymes, the active site of FDH contains important protonatable residues, for example, amines and alcohols. These lead to high local concentration of protons near the active site during catalysis. They therefore act as proton relays, shuttling protons to the active site. These proton relays may have two effects: first, they can lower the kinetic barrier to reaction, making turnover rates more useful. Secondly, rapid reaction with proton may aid in minimising unwanted alternate pathways.

Our target was to access dithiolene complexes in which proton relay groups could be introduced in such a way that they could lie close to the metal centre during catalysis. In order to do that, we realised that we would need to develop new approaches to accessing molybdenum dithiolenes. At the same time, we wished to obtain a primary coordination sphere as close to that seen in the enzyme as we could. We reasoned that this should include the potential to introduce a dithiolene as the final ligand at the metal centre. This necessitated avoiding the more convenient molybdenum oxo systems and instead utilising the more versatile but more reactive molybdenum carbonyls.

We identified access to functionalised dithiolone as a possible route (Scheme 3.3). Radical cyclisation in ‘step a’ (Scheme 3.3) could be utilised for the synthesis of these precursors despite the presence of protic groups. We anticipated that this would minimise or avoid the necessity for protecting group manipulation. We then



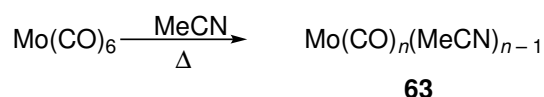
Scheme 3.3: A brief overview of our strategy where blue represents our original strategy and pink is revised strategy.

hoped to transfer to the metal either directly or via nickel and thus have a short and convenient route to the desired systems. For synthetic ease in this first generation strategy, we chose to target oxygen as the proton carrier.

3.2 Molybdenum carbonyl precursors

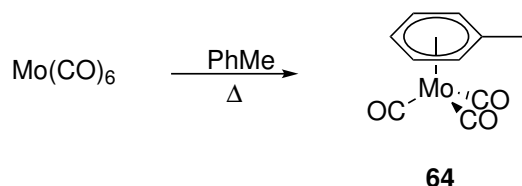
Molybdenum hexacarbonyl has low solubility in toluene and acetonitrile at room temperature. Therefore, in order to introduce the dithiolene ligand, more reactive and soluble molybdenum containing precursors were required.

The precursor explored was the acetonitrile adduct (Scheme 3.4). Freshly distilled acetonitrile and molybdenum hexacarbonyl were refluxed for 16 hours, affording an olive solution with a dark brown solid. This was filtered, evaporated and washed with ether to give pale yellow solid, **63**. When redissolved in acetonitrile, the infrared spectrum showed maxima at 1911 and 1841 cm^{-1} for the carbonyls. In contrast, when dissolved in dichloromethane, three bands were observed at 1980, 1946 and 1904 cm^{-1} . Whilst these spectra confirmed that some of the carbonyls had been substituted, it was not possible to ascertain the ratio of acetonitrile to carbonyl accurately.



Scheme 3.4: Synthesis of complex **63**.

The difficulty in determining the degree of substitution in **63** was mitigated by switching to the toluene adduct (Scheme 3.5).^{112,113} Molybdenum hexacarbonyl was dissolved in toluene and refluxed at 130 °C for five days, monitoring by IR. Three peaks were observed after one hour at 1989, 1975 and 1892 cm^{-1} . This was likely a mixture containing starting material and unidentified intermediates. The reaction was worked up when there were only two peaks in the IR spectrum, at 1970 and 1890 cm^{-1} . Re-dissolution of the pale yellow solid in dichloromethane gave signals at 1968 and 1885 cm^{-1} , in agreement with the literature.

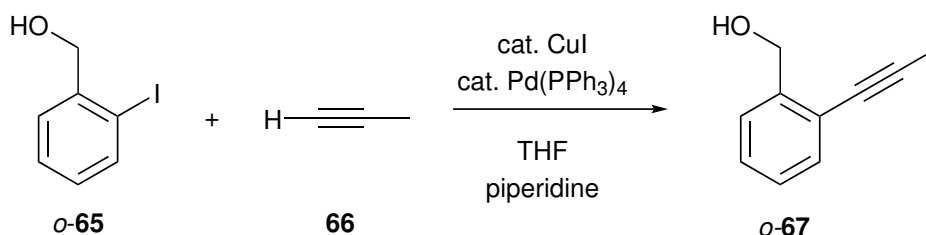


Scheme 3.5: Synthesis of complex **64**.

3.3 Functionalised dithiolone ligands

3.3.1 (Propyn-1-yl)benzyl alcohol

Previous work within the group had established the necessity of a methyl group on the alkyne as the terminal equivalence suffered from degradation likely linked to the reactivity of the alkyne proton. The first step in the synthesis of functionalised ligand was the Sonogashira coupling of *ortho*-iodobenzyl alcohol with propyne to give the known alkyne *o*-**67** (Scheme 3.6).^{114,115} Provided a significant excess of propyne was used, the reaction proceeded in very high yield (96%). The identity of the product was confirmed by ¹H and ¹³C NMR spectroscopy. It was important to ensure complete reaction as the product and starting material were inseparable by chromatography. Sublimation could be employed for purification provided the amount of residual iodide was small.

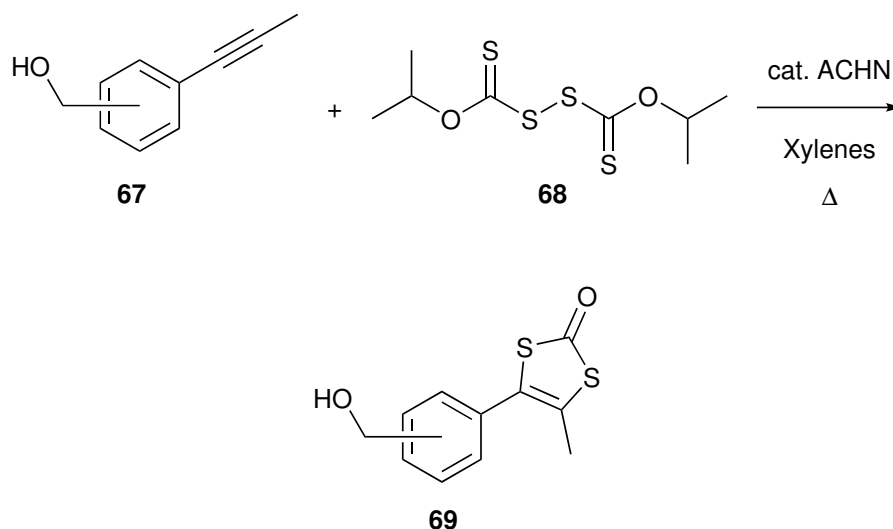


Scheme 3.6: Synthesis of *o*-**67**.

3.3.2 Unprotected dithiolone

Our first approach was to synthesise the dithiolone group prior to introduction of any protection on the pendent alcohol. This would allow us to use a small number of common intermediates and to access a much larger family of derivatives rapidly.

The family of dithiolones were synthesised following a method developed within our research group (Scheme 3.7). Diisopropyl xanthogen disulfide (**68**) and the respective alkyne were dissolved in xylenes and heated to 140 °C for 18 hours in the presence of radical initiator 1,1'-azobis(cyclohexanecarbonitrile) (ACHN). The



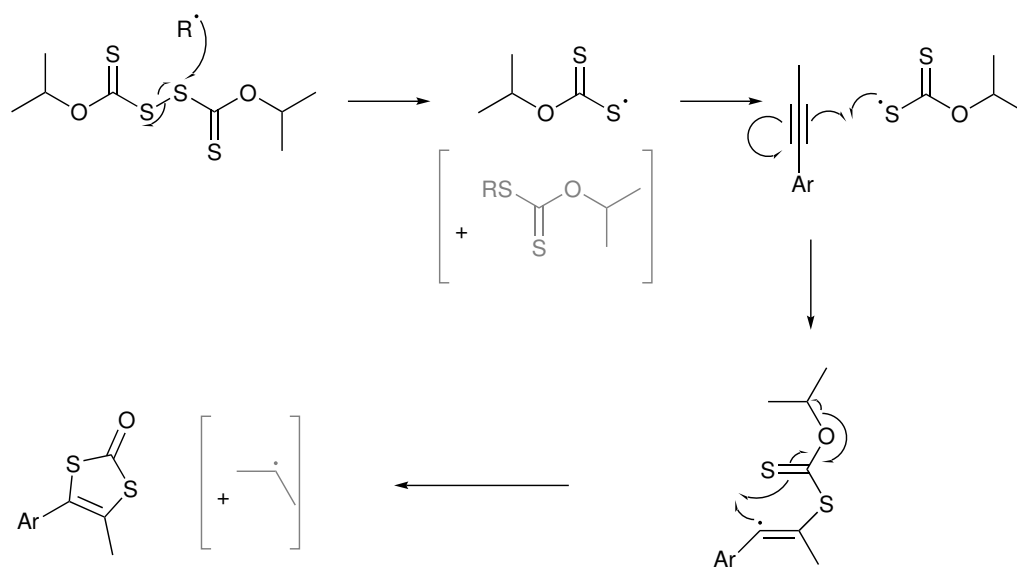
Scheme 3.7: Synthesis of the dithiolone family **69**.

reaction did not work well in the presence of the bulky radical initiator 2,2'-azobis(2-methylpropionitrile) (AIBN). Even when using the more powerful radical initiator ACHN, the reaction did not proceed to completion. However, it was possible to separate the unreacted alkyne from the desired product by chromatography. The recovered alkyne could then be used in repeated radical cyclizations. A suggested mechanism for radical cyclisation is given in Scheme 3.8.

Although there should be a unique C=O stretch in the IR for **69**, in our experience this band has extremely low strength and therefore is not viable diagnostic feature. ^{13}C NMR spectroscopy does differentiate between **67** and **69**, but this technique is ideally applied only after purification. The quaternary nature of the key carbon atoms also means that this spectroscopic method is less suited to monitoring the progress of reaction. As such, the success of these reactions were assessed by the changes in the proton NMR spectra of the products. These were supported by subtle alterations in the R_f values of the products when compared to the starting materials.

3.3.3 TIPS-protected *o*-dithiolone

With the alcohol functionalised dithiolones in hand, we were free to choose protecting groups. One major family of protecting groups are the silyl systems.¹¹⁶ We selected

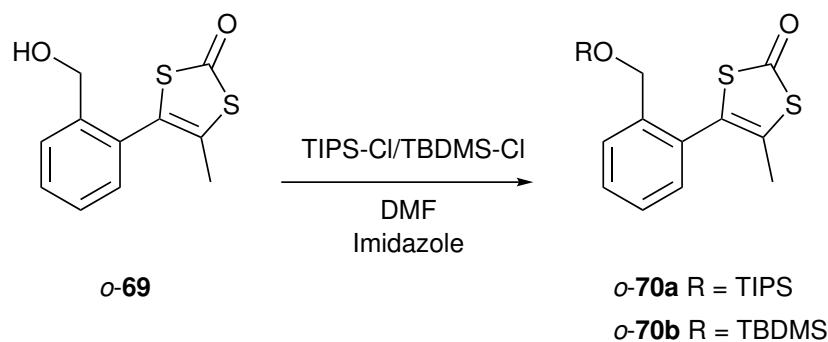


Scheme 3.8: Suggested mechanistic scheme of the radical reaction to form dithionones: R^\bullet represents the radical derived from the initiator (in the first cycle) or the secondary isopropyl radical (in subsequent cycles).

the triisopropylsilyl (TIPS) group as this is moderately bulky and widely used in synthetic strategies.

The ligand *o*-**69**, imidazole and TIPS-Cl were stirred in DMF for 16 hours (Scheme 3.9). After aqueous work-up, a teal oil was obtained. Thin layer chromatography was carried out in 3:1 hexane–ethyl acetate by spotting the unprotected starting material against the protected compound and also co-spotting them both. The protected compound *o*-**70a** had an R_f value of 0.78 and unprotected starting material had an R_f value of 0.30. As expected, the combined spot showed the presence of both the starting material and expected product. Confirmation of incorporation of the TIPS group was obtained in the proton NMR spectrum, which contained a broad multiplet in region of 1.03–1.12 ppm for the silyl group. The starting material contains a triplet for the alcohol group at 1.70 ppm which was absent in the product.

The oily product was not very stable and had a shelf life of a few days. Therefore, in practice, the protection was carried out just before it was used in the next step of the reaction.



Scheme 3.9: Synthesis of *o*-70.

3.3.4 TBDMS-protected *o*-dithiolone

The second silyl group we chose to explore was the bulkier *tert*-butyldimethylsilyl (TBDMS) moiety. This is known to be more resistant to hydrolysis/removal than TIPS.¹¹⁶ We reasoned that this could be advantageous in establishing a synthetic route, although we were mindful that it could impede unveiling of the free alcohol on the metal centre. The reaction was carried out following the same procedure as for *o*-70b (Scheme 3.9). We chose to carry out the protection step just prior to subsequent chemistry to avoid any issues with decomposition (as observed with *o*-70a).

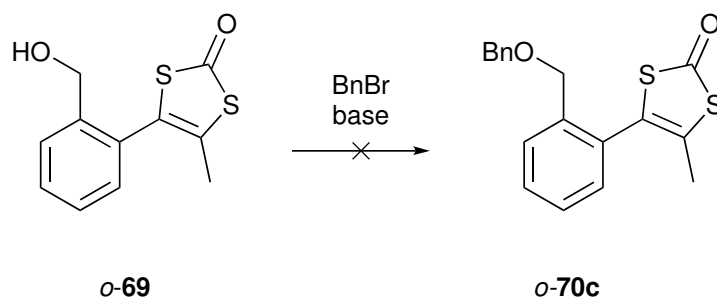
As above, thin layer chromatography was carried out in 4 : 1 hexane–ethyl acetate. The protected compound had an R_f value of 0.70 and unprotected starting material had an R_f value of 0.17. As expected, the combined spot showed the presence of both the starting material and expected product. As in the synthesis of *o*-70a, the key spectroscopic confirmation was the disappearance of the alcohol proton at 1.70 ppm.

3.3.5 Benzyl-protected *o*-dithiolone

The other major protecting strategy for alcohols is to use a benzyl (or benzyl derivative) group.¹¹⁶ We therefore sought to protect *o*-69 under standard conditions (DMF, benzyl bromide, room temperature) (Scheme 3.10). However, multiple efforts to protect the alcohol on the dithiolone were unsuccessful (Table 3.1).

Table 3.1: Reaction conditions for attempted protection of *o*-**69**.

Base	Solvent	Conditions
Potassium carbonate	acetone	Reflux
Imidazole	DMF	Ar
Sodium hydride	THF	Ar
Lithium diisopropylamide	THF	Ar



Scheme 3.10: Failed synthesis of *o*-**70c**.

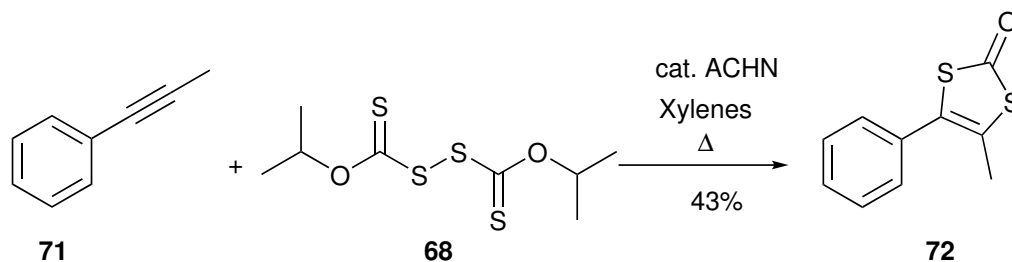
We chose to discontinue efforts in this area, instead focussing on benzyl protection prior to formation of the dithiolone ring (see below).

3.3.6 Unsubstituted dithiolone

In order to compare the effect on functionalised ligand on our envisaged molybdenum system, we decided to synthesise a version lacking any substitution on the phenyl ring. The reaction starting from 1-phenylpropyne (**71**) was carried out as for *o*-**69** (Scheme 3.11), with purification using hexane–EtOAc 9 : 1. In addition to ¹H NMR spectroscopy, the identity of the product was confirmed by high resolution mass spectrometry. This gave an ion at 209.0098 Da, consistent with the desired parent ion.

3.4 Alkynes bearing protected alcohols

As detailed above, our initial aim was to protect the alcohol at the latest step of the synthesis possible. However, failure to obtain the benzyl protected *o*-**70c** forced us



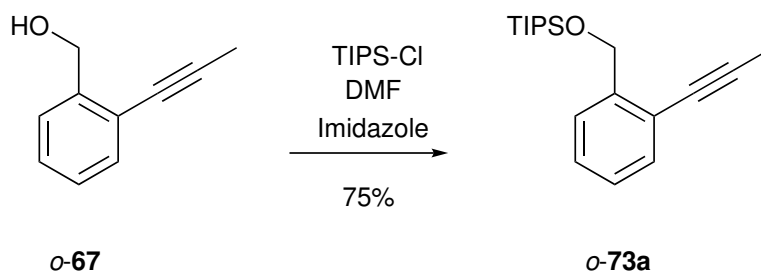
Scheme 3.11: Synthesis of the unsubstituted **72**.

to explore the alternative route: protecting the alcohol group at the alkyne stage, before reacting with disulphide to make the benzyl-protected dithiolone.

In the interest of comparison we decided to do two parallel reactions and protect the alcohol group with both TIPS and benzyl at the alkyne stage in turn, before the carrying it through to dithiolone stage.

3.4.1 TIPS-protected *o*-alkyne

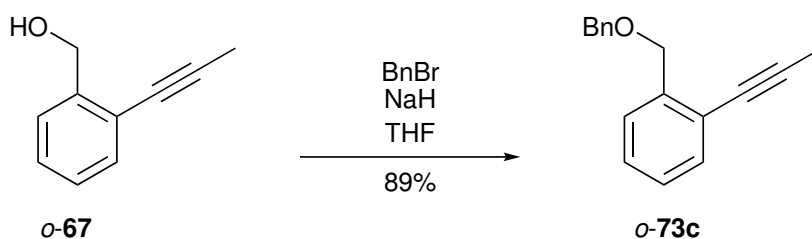
Imidazole and TIPS-Cl were dissolved in DMF along with *o*-**67** and stirred for 16 hours (Scheme 3.12). The progress of the reaction was monitored with thin layer chromatography with 3 : 1 hexane–ethyl acetate as mobile phase ($R_f = 0.73$). Aqueous work-up afforded a light yellow oil in good yield and the identity of the product was confirmed by ^1H , ^{13}C NMR spectroscopy and high resolution mass spectrometry.



Scheme 3.12: Synthesis of *o*-**73a**.

3.4.2 Benzyl-protected *o*-alkyne

NaH was used to deprotonate 2-(propyn-1-yl)benzyl alcohol *o*-**67** in THF at 0 °C. Benzyl bromide was added to this suspension and stirred at room temperature for 16 hours (Scheme 3.13). The yellow oil afforded after organic work-up was purified by flash chromatography on silica gel in hexane–EtOAc (9 : 1) yielding the product as a white solid. The identity of the product was confirmed by ¹H, ¹³C NMR spectroscopy and high resolution mass spectrometry.



Scheme 3.13: Synthesis of *o*-**73c**.

3.5 Dithiolone formation: from protected alkyne

3.5.1 Benzyl-protected *o*-dithiolone

The benzyl protected dithiolone was obtained via the previously used radical initiator method along with the benzyl protected alkyne (Scheme 3.14). The product was purified by flash chromatography in hexane–EtOAc 20 : 1. In the ¹³C NMR spectrum, the presence of the C=O group could be confirmed by a signal at 191.99 ppm. The identity was confirmed by high resolution mass spectrometry, with molecular ion at 329.0667 Da.

3.5.2 TIPS-protected *o*-dithiolone

The previously-described TIPS-protected dithiolone can be accessed by a similar route. This gave a material with identical spectroscopic properties to that obtained

solvent under reduced pressure. The crude material was purified by chromatography (hexane–CH₂Cl₂ 4 : 1). Two fractions were obtained, the first as small amount of reactive purple solid, followed by the tris(ligand) by-product as a green solid. The target complex had infrared peaks at 2038 and 1995 cm⁻¹ in toluene, while there were no carbonyl bands present in the infrared of the green solid. The identity of the desired material was confirmed by mass spectrometry, which showed the parent ion at 1196.3591 Da.

The colouration of the two products is a general feature of the target molybdenum dithiolenes. The purple target complexes were also unstable with respect to the tris(dithiolene) adducts. Whilst in the case of the TIPS adduct we were unable to obtain either mass spectral data or single crystals, other reactions yielded clear evidence for our assignment of the metal ligand sphere (see below).

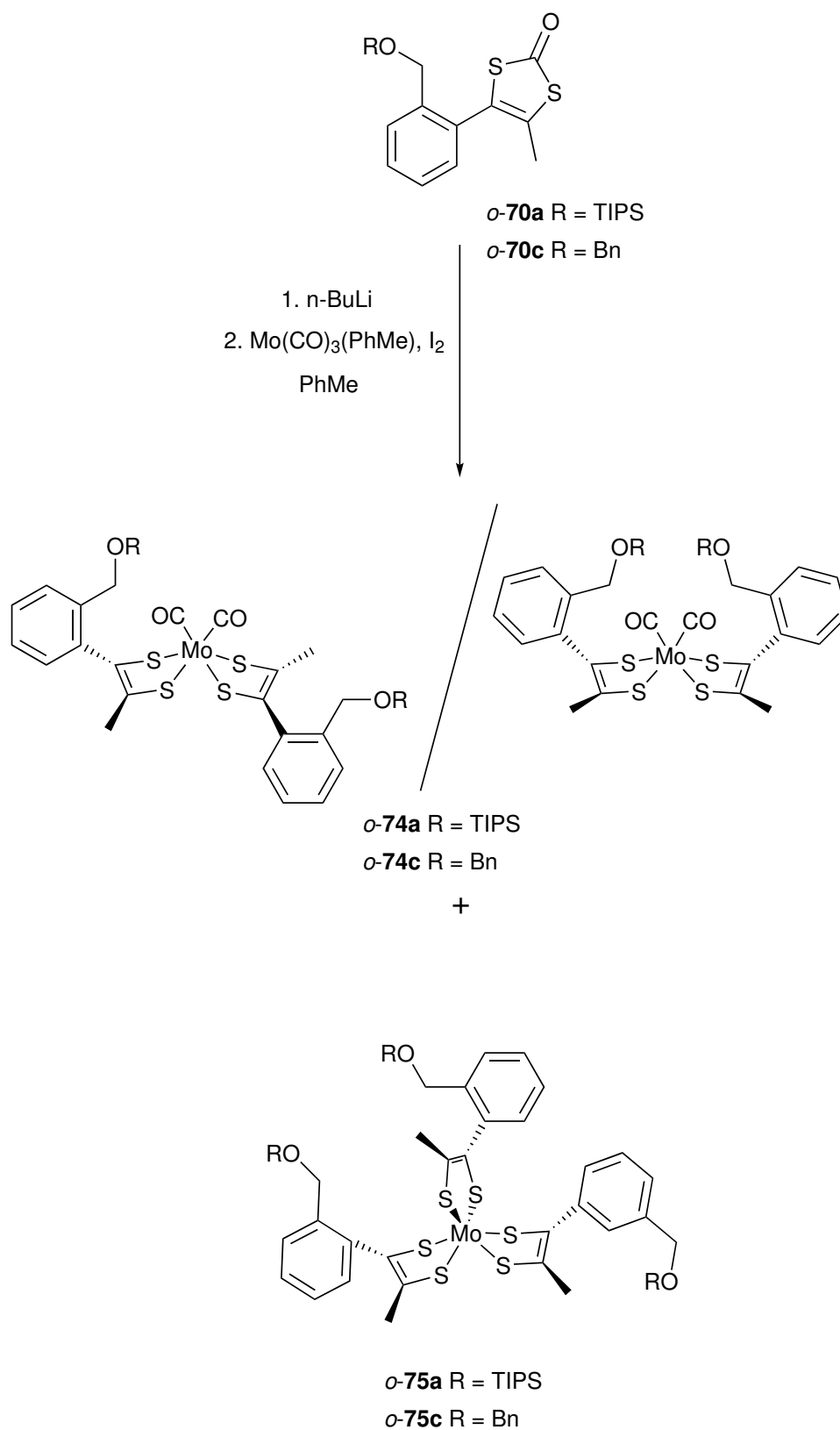
As illustrated in Scheme 3.15, the coordination geometry in these compounds is anticipated to be trigonal prismatic. This is a well-established general feature of metal dithiolene complexes,^{117,118} and has been demonstrated by Holm in simple symmetrical systems.¹¹⁹ The relative disposition of the aromatic groups may be *cis* or *trans*, and fluxional behaviour is likely. This is further explored in Chapter 4.

3.6.2 Benzyl-protected molybdenum complex

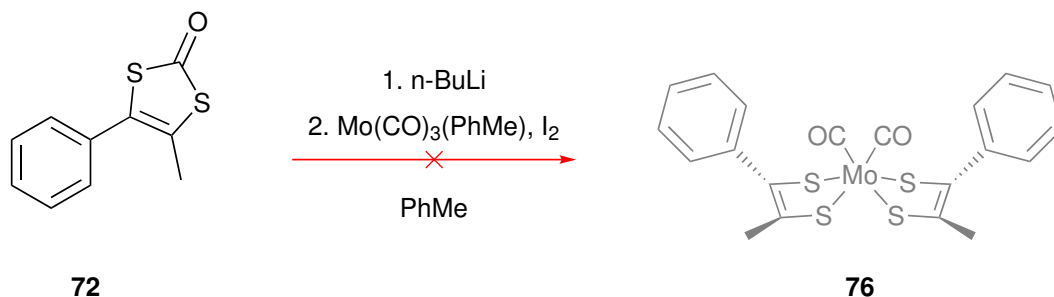
Reaction was carried out by the same method as for the synthesis of complex *o*-**74c** (Scheme 3.15). This gave a small amount of purple material which decomposed rapidly.

3.6.3 Unfunctionalised molybdenum complex

Reaction was carried out using the same method as for complex *o*-**74c** (Scheme 3.16). The dark brown solution in which the only observable infrared maxima for CO were at 1983 and 1941 cm⁻¹ in toluene. These correspond to the starting material.



Scheme 3.15: Synthesis of molybdenum dithiolene complex from protected ligand.



Scheme 3.16: Attempted synthesis of molybdenum dithiolone complex with unfunctionalised ligand.

3.7 Deprotection

Upon successful coordination of protected dithiolone onto molybdenum, the natural next step of the synthetic route was to deprotect the alcohol. Various literature methods are available for this process. Here, we have attempted deprotection in three different ways.

3.7.1 Deprotection of *o*-74a using TASF

Complex *o*-74a was dissolved in THF and cooled to 0 °C. To the resulting purple solution, TASF (tris(dimethylamino)sulfonium difluorotrimethylsilicate) was added.¹²⁰ The solution immediately turned green then black within 5 minutes. An infrared spectrum of the crude reaction mixture showed no CO bands.

3.7.2 Deprotection of *o*-74a using Et₃N · 3 HF

Complex *o*-74a was dissolved in THF and cooled to 0 °C as before. Et₃N · HF was added to this purple solution.¹²¹ The solution immediately turned brown then green. An infrared spectrum of the crude reaction mixture showed no CO bands.

3.7.3 Deprotection of *o*-74a using TBAF

As before, complex *o*-74a was dissolved in THF and cooled to 0 °C. TBAF (tetrabutylammonium fluoride) was added to the purple solution.¹²² The solution imme-

diately turned black. An infrared spectrum of the crude reaction mixture showed no CO bands.

3.7.4 Summary

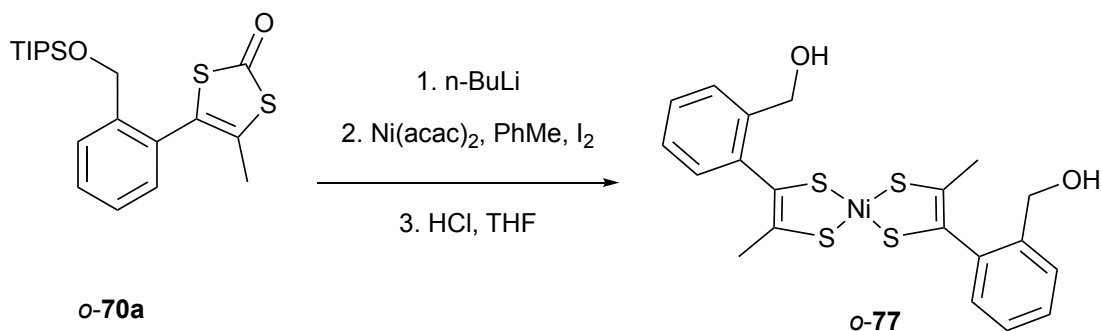
A green solution is indicative of formation of the homoleptic molybdenum tris(dithiolene) complexes **75**, consistent with the loss of CO bands. Parallel work in the Wright group have proved that by obtaining crystal structure of the complex after a deprotection attempt. The crystal structure shows tris coordinated dithiolene with unprotected alcohol on molybdenum centre. Therefore, it seems that the any deprotection step of the bis coordinated metal complexes leads to rapid formation of the tris-coordinated complex before decomposing completely. There are two possible causes for this: attack on the metal centre by free fluoride, or ligand rearrangement due to hydrogen bonding.

3.8 Formation of molybdenum dithiolene complexes via nickel

Since it proved impossible to deprotect the alcohol once on the molybdenum centre, we chose to revise our synthetic route. We decided to access the molybdenum complex via nickel. The revised route included coordinating the protected ligand onto nickel first, and then deprotecting it to give unprotected bis nickel complex, followed by transmetalation onto molybdenum centre.

3.8.1 *Ortho*-nickel complex using TIPS-protected proligand

The bis(dithiolene) nickel complex *o*-**77** was synthesised following Scheme 3.17. *n*-BuLi in hexanes was added to *o*-**70c** in PhMe at 0 °C and stirred for 16 hours to give a yellow solution. This was then added drop wise to Ni(acac)₂ in PhMe. I₂ was



Scheme 3.17: Synthesis of nickel dithiolone complex.

added to the solution after two hours and stirred for another 16 hours. I₂ was added to oxidise the initial diionic product.¹⁰⁹ The solvent was removed at reduced pressure. The residue was taken up in THF prior to addition of aq. HCl. The reaction was stirred for one hour, diluted with EtOAc before aqueous work-up to afford brown oil. An acidic work-up was used such that the silyl group were removed without requiring a second synthetic step. Complete removal of the TIPS–OH by-product was not possible; as a result calculation of yield is inappropriate in this instance.

3.8.2 *Ortho*-nickel complex using TBDMS-protected proligand

Reaction was carried out following the same method as starting from the TIPS-protected proligand. After removal of the protective group using HCl, the reaction solution was dark purple. This was then purified by chromatography on silica using hexane–EtOAc 1 : 1 as the mobile phase. The product was obtained as a dark green oily solid.

Crystals of *o*-77 suitable for X-ray diffraction were obtained from a concentrated solution of the complex (Figure 3.3). This confirmed the identity of the product and the square planar nature of the nickel centre.

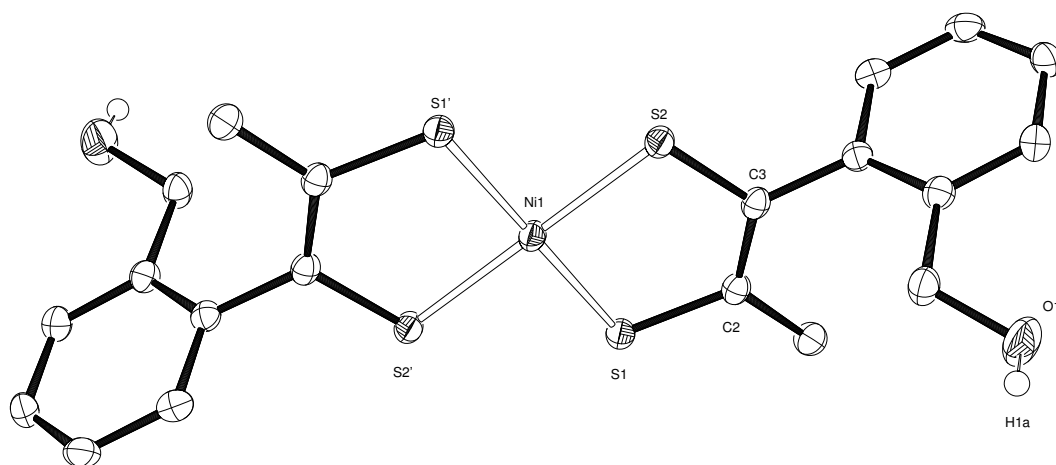
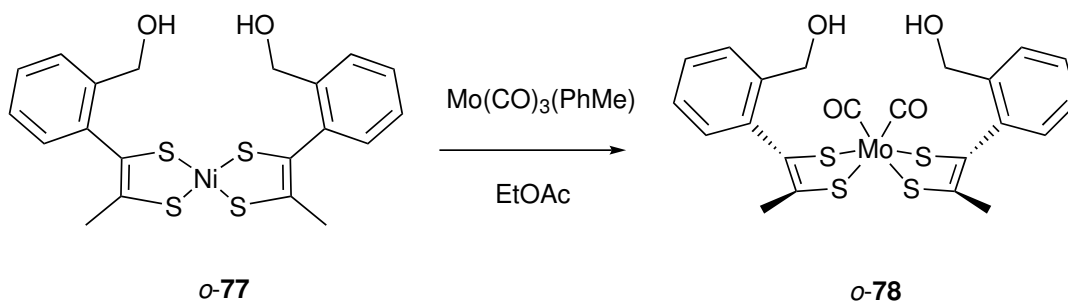


Figure 3.3: ORTEP representation of the structure of *o*-77 showing 50 % probability ellipsoids; protons bound to carbon have been omitted for clarity.

3.8.3 *Ortho*-molybdenum complex

Complex *o*-77 was dissolved in EtOAc and added rapidly to $\text{Mo}(\text{CO})_3(\text{PhMe})$ in EtOAc (Scheme 3.18). The reaction was stirred for 16 hours then the solvent was removed at reduced pressure. Purification on silica, using hexane–EtOAc 1 : 1 as the mobile phase, gave *o*-78 as a purple solid along with the tris(ligand) adduct as a green solid. Infrared of the solution of the purple solid in EtOAc showed peaks for the bound carbonyls at 2035 and 1983 cm^{-1} . Although this material decomposed on silica, rapid column chromatography was possible to give a small amount of purple material. Notably, this reaction demonstrated that the bis(dithiolene) complexes barring free alcohol groups are accessible.



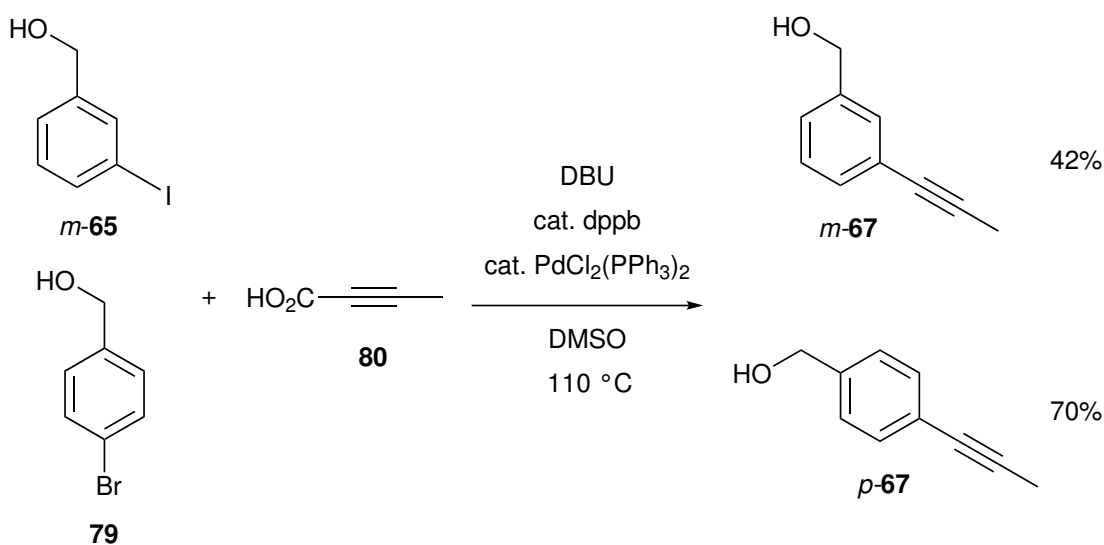
Scheme 3.18: Synthesis of molybdenum dithiolone complex via transmetalation.

3.9 Side chain position

Following the successful synthesis molybdenum dithiolone complex via transmetalation, we decided to explore the chemistry of this metal complex at different positions of the functionalised group. This entailed synthesising *meta* and *para* alkynes followed by synthesis of dithiolones.

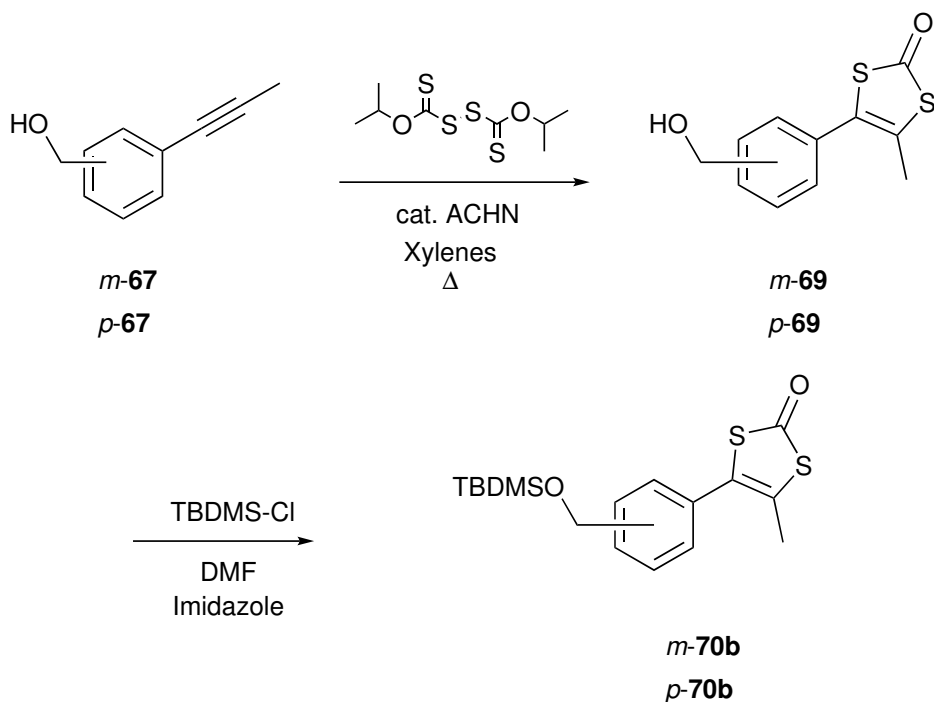
3.9.1 Ligand preparation

In contrast to the synthesis of *o*-**67**, Sonogashira coupling using propyne gas worked poorly for formation of the *meta* and *para* isomers. Therefore an alternative route was used for the synthesis of *meta* and *para* alkynes (Scheme 3.19).¹²³ This method exploits the reactivity of 2-butynoic acid, which acts to provide a propyne equivalent in situ. The reaction proceeds in good yield for the *meta* and *para* isomers, but was not successful when applied to the synthesis of *o*-**67**.



Scheme 3.19: Synthesis of *m*-**67** and *p*-**67** (dppb = 1,4-bis(diphenylphosphino)butane, DBU = 1,8-diazabicyclo[5.4.0]undec-7-ene).

Following the same route as described for *o*-**70b** (Scheme 3.20), radical cyclisation to the dithiolones followed by protection with TBDMS-Cl gave the desired proligands. All compounds on these routes gave satisfactory proton NMR spectra.



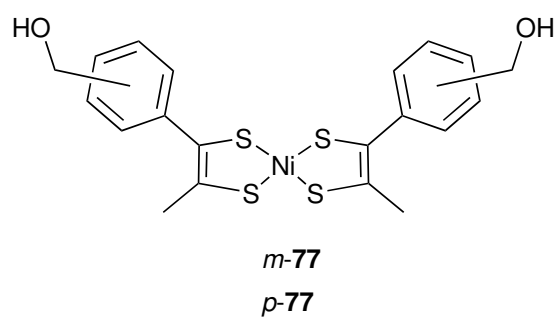
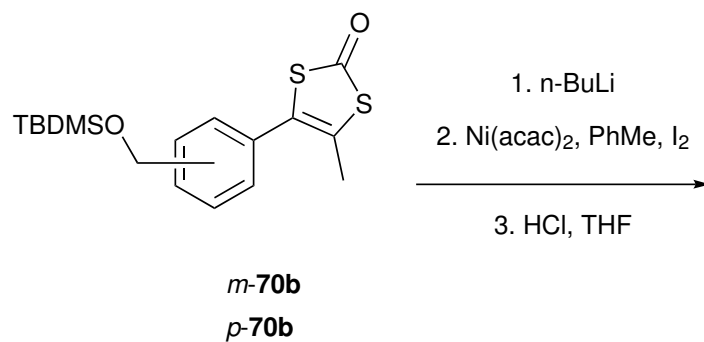
Scheme 3.20: Synthesis of proligands *m*-**70b** and *p*-**70b**.

3.9.2 Metal complex formation

Reaction of the proligands with nickel followed the same approach as used before (Scheme 3.21). As for the *ortho* isomer, workup conditions were used to remove the protecting group, giving the unprotected nickel complexes in excellent yield (99%).

Crystals suitable for X-ray diffraction were grown for *p*-**77** (Figure 3.4). The metrical parameters of the structure are unremarkable, confirming square planar nature of the nickel and the identity of the ligand. Low resolution mass spectrometry confirmed parent ion was present for both the meta and para isomers.

Transfer of the ligands onto molybdenum occurred smoothly (Scheme 3.22). In both cases reaction mixtures yielded purple solids identified as the bis(ligand) adducts, along with the green tris(dithiolene) complexes. These could conveniently



Scheme 3.21: Synthesis of nickel complexes *m-77* and *p-77*.

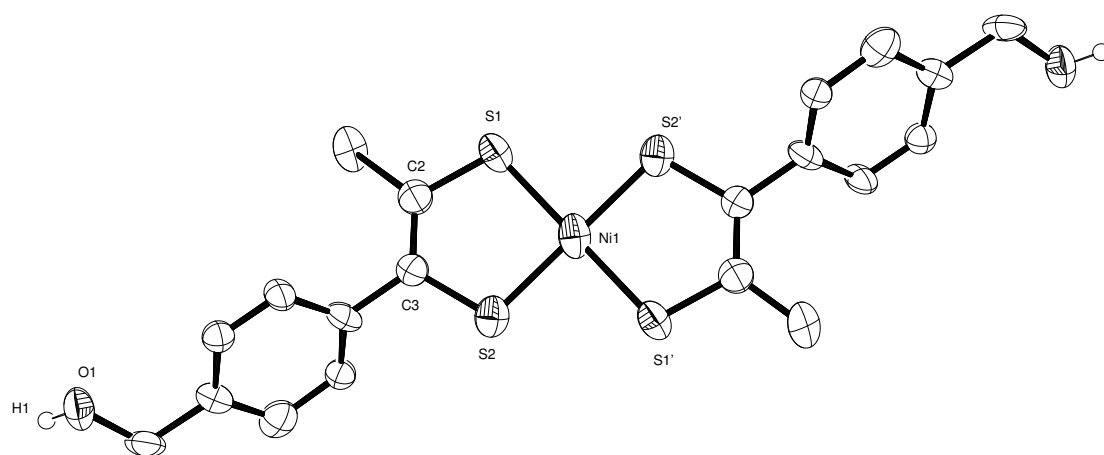
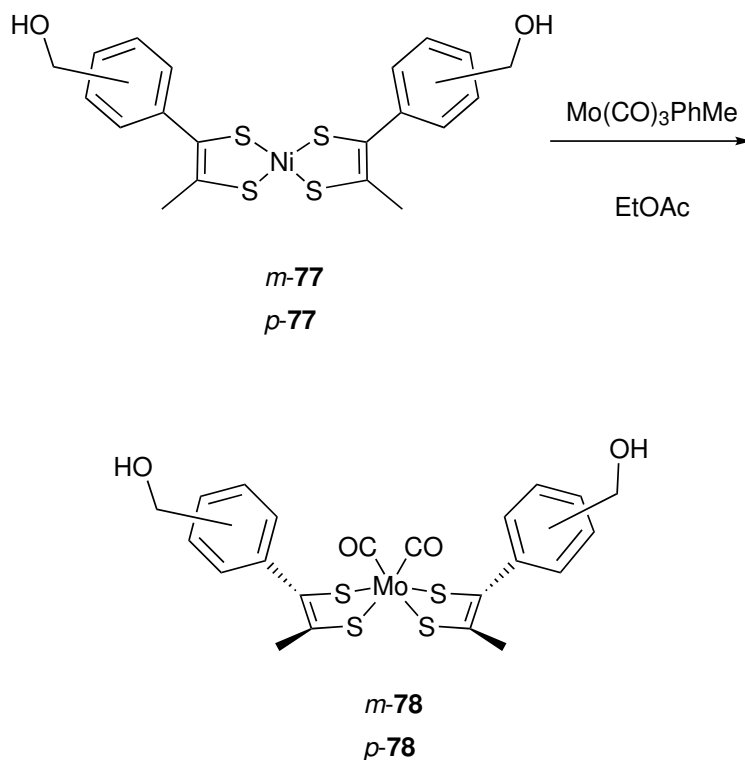


Figure 3.4: ORTEP representation of the structure of *p-77* showing 50% probability ellipsoids; protons bound to carbon have been omitted for clarity.



Scheme 3.22: Synthesis of molybdenum complex *m-78* and *p-78*.

be separated by column chromatography. Formation of the target compounds was confirmed by infrared spectroscopy (Table 3.2). In the case of *m-78*, the presence of starting material obscured the lower energy band for the product. Whilst the use of different solvents preclude detailed comparison, it is clear that the CO stretching frequencies are broadly similar in all of these compounds.

Table 3.2: Positions of CO bands in Mo(dithiolene)₂(CO)₂.

Compound	$\tilde{\nu}_{\max}/\text{cm}^{-1}$	Solvent
<i>o-74a</i>	2038 1995	PhMe
<i>o-78</i>	2035 1983	EtOAc
<i>m-78</i>	2039 –	CH ₂ Cl ₂
<i>p-78</i>	2044 1983	EtOAc

3.10 Summary

A novel route has been developed to access alcohol functionalised dithiolene ligands. This can be used to synthesise complexes of the form $\text{Mo}(\text{CO})_2(\text{dithiolene})_2$. Formation of these complexes directly was hindered by attack on the metal centre under deprotection conditions. This required us to use transmetallation route via nickel with inevitable loss of half of the proligands.

The range of protecting groups which could be used was surprisingly limited. Only TBDMS gave proligands with reasonable lifetimes, while TIPS protection gave surprisingly unstable intermediates. Access to benzyl-protected proligands proved frustrating impossible.

The target bis(dithiolene) complexes are extremely sensitive to CO loss. Even under most successful conditions, significant amounts of tris(dithiolene) complexes were formed. Ligand redistribution from bis to tris dithiolene complexes, with formation of unidentified decomposition product, must be responsible. This suggests that alternative molybdenum supporting ligands need to be explored in the future.

Chapter 4

Density functional theory

4.1 Introduction

4.1.1 Computational methods

Computational methods allow us to examine systems which are otherwise inaccessible, to confirm experimental data for challenging molecules and to probe reaction pathways. For organic and organometallic systems of up to around 50 atoms, Density functional theory (DFT) is today the dominant computational approach employed. It occupies this position as it offers a good balance between complexity and accuracy. Ground state calculations, which yield optimised geometries, thermochemistry and spectra, are in many ways a routine part of the small molecule chemistry today.

Whilst the theory of DFT was established in the 1960s,^{124,125} it was not available for ‘daily’ use until about early 2000s. A detailed overview is given by Koch and Holthausen.¹²⁶ In earlier studies, it was necessary to significantly simplify the structure of target molecules in order to make them accessible. With the increased processing power of the modern computers, DFT has become much more accessible and it has been possible to simulate ‘bigger’ side chain than hydrogen.

Modern (commercial) DFT packages provide interfaces which require only minimal understanding of the underpinning physics and mathematics. Although it is necessary

to have an appreciation of the key concepts involved. The aim in all computational chemistry is to find approaches which address the fact that the Schrödinger equation can not be solved analytically. In DFT, we utilise the fact that molecular properties are completely determined by electron density, rather than needing to calculate wavefunctions.¹²⁵ To address electron-electron interactions, a set of effective orbitals are used which move the problematic physics to a so called exchange-correlation functional.¹²⁴ There are a number of the latter, but key is that they can be used in iterative numerical calculations.

The net result of this approach is that in order to calculate molecular properties, we require the following

- An initial set of coordinates
- A choice of level of theory, typically guided by reference calculations benchmarked against known molecules, or against high level computational models.
- A description of the molecular orbitals of the atoms involved, which for heavier atoms typical requires that core electrons are treated as a single ‘frozen’ unit

4.1.2 Previous modelling

There are very limited reports of previous DFT studies of molybdenum bisdithiolene complexes. This is likely in part due to the fact that only a few groups have published experimental data for molybdenum dithiolene CO complexes.

The most significant publication featuring DFT studies directly relevant here was reported by Holm in 2001.¹¹⁹ In this report the ADF program^{127–129} was used for a detailed study of the orbital contributions in the simple symmetrical dithiolene **81**. Whilst this paper demonstrated that insight into molybdenum dithiolenes is obtainable by DFT, there has been very little following work. Most notably, there is no DFT data reported on the closely related system **82**.

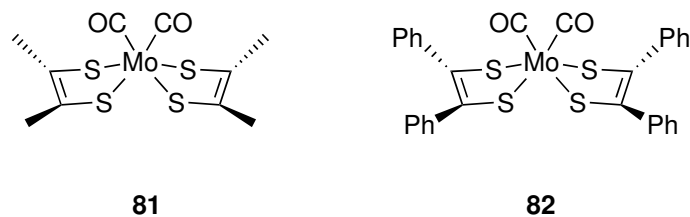


Figure 4.1: Model compounds for DFT.

Dithiolene complexes of other metals and molybdenum tris(dithiolene) systems have been examined by DFT. However the relevance of these results to our studies is limited as they lack the crucial CO groups. For example, the Hall group published an extensive study on nickel bis(dithiolenes),¹³⁰ but their approach did not yield useful results when applied to our systems (see below).

4.2 Selection of approach

Given the limited number of DFT studies on molybdenum dithiolenes, before investigating our novel systems, we first needed to establish an appropriate computational setup. We chose synthetically established compounds **81** and **82** (Figure 4.1) as our trial systems and compared the outputs against published experimental values.

The most widely used DFT package in the group is Gaussian.¹³¹ It was also used by the Hall group in an extensive study of nickel dithiolenes.¹³⁰ Therefore Gaussian was our first port of call when choosing a package for DFT. We attempted to optimise the geometry of **81** using both B3LYP¹³² and TPSS¹³³ levels of theory. In the case of B3LYP, the geometry was distorted significantly from the crystal structure and the simulated infrared stretches were out by around 40 cm^{-1} from experimental values. In the case of TPSS, calculations failed to yield a self-consistent field. Given these issues, we decided to investigate the other computational package available to us: ADF.

The Holm group used a version of ADF in their early studies of **82**.¹¹⁹ Using ADF and a triple ζ basis set, we explored three different functionals. We again

used B3LYP, along with the related BP86 approach.^{134,135} We also attempted to use ω B97X.¹³⁶ All three functionals gave good geometry conversion for **81** but we were unable to obtain simulated infrared using ω B97X. For the larger substrate **82**, only BP86 gave successful geometry optimisation.

Following geometry optimisation, ADF calculations were carried out to generate vibrational modes and associated dipole moment changes for the minimised structures. A comparison of the predicted infrared bands with the experimental values is given in Table 4.1. It is clear that the absolute position of the CO bands is not well reproduced in these simulations. However, they do give us some sense of the correction required to map computational values to those obtained experimentally. Crucially, we were only able to get reasonable geometry using BP86. We therefore chose to use this approach for subsequent calculations, subject to the need to treat absolute infrared shifts cautiously.

Table 4.1: Computational results for **81** and **82**.

Entry	Compound	$\tilde{\nu}_{\max}/\text{cm}^{-1}$		
		Experimental ¹³⁷	BP86	B3LYP
1	81	1983, 2032	1948, 1988	–
2	82	1964, 2025	1941, 1985	2028, 2068

4.3 Simulation of dithiolene isomers

4.3.1 Detailed analysis of *ortho* isomers

With the computational approach ‘optimised’, we turned to the detail of possible geometric isomers of our target systems. Initial efforts focused on the geometric isomers of the *o*-**78** (Figure 4.2). It is possible for the two methyl groups to be either relatively *cis* or *trans*. It is also possible for the hydroxy groups to be on the same side as the CO group; we chose to describe this arrangement as up and down for the opposite arrangement. Thus there are a total of six geometrical isomers to be

studied.

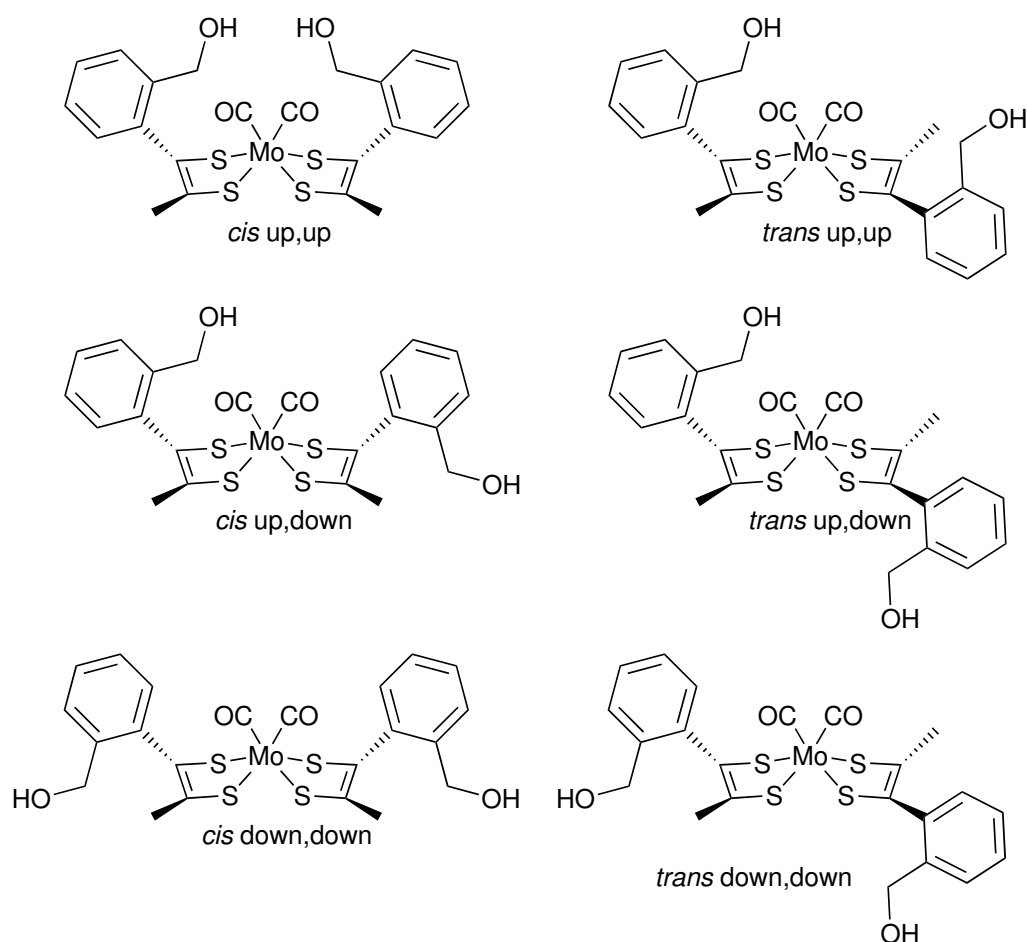


Figure 4.2: Isomers of the *o*-78 used to evaluate DFT.

Simulations of all six isomers proceeded smoothly (Table 4.2). The target geometry was retained throughout the isomers. The relative energies of the different isomers varied by only 3.3 kJ mol^{-1} . This is within the range typically regarded as insignificant in DFT calculations, meaning that none of the isomers can be regarded as either dominant or excluded on the basis of the simulation. This suggests that it is likely there is a dynamic equilibrium in solution.

Potential hydrogen bonding is of particular interest in these systems. One obvious concern is whether the two hydroxy groups are sufficiently close to hydrogen bond to each other, hindering their ability to interact with a substrate. The two systems with the greatest potential for hydrogen bonding in this way are the *cis* systems with

Table 4.2: Computational results for *o*-**78**. Energies are given relative to the *cis* down,down isomer.

Entry	Isomer		$E/\text{kJ mol}^{-1}$	$\tilde{\nu}_{\text{max}}/\text{cm}^{-1}$	
1	<i>cis</i>	up up	3.3	1953	1993
2	<i>cis</i>	up down	2.7	1951	1992
3	<i>cis</i>	down down	0.0	1950	1991
4	<i>trans</i>	up up	1.6	1945	1986
5	<i>trans</i>	up down	0.4	1945	1986
6	<i>trans</i>	down down	0.2	1950	1991

hydroxy group on the same side of the metal. The simulated systems are shown in Figure 4.3 and Figure 4.4.

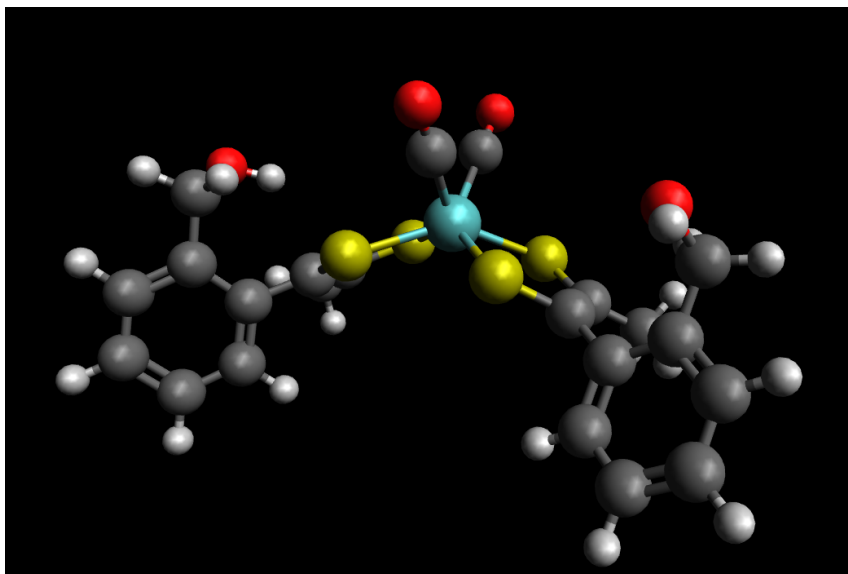


Figure 4.3: Ball and stick representation of the energy minimised geometry of *cis* up,up *o*-78.

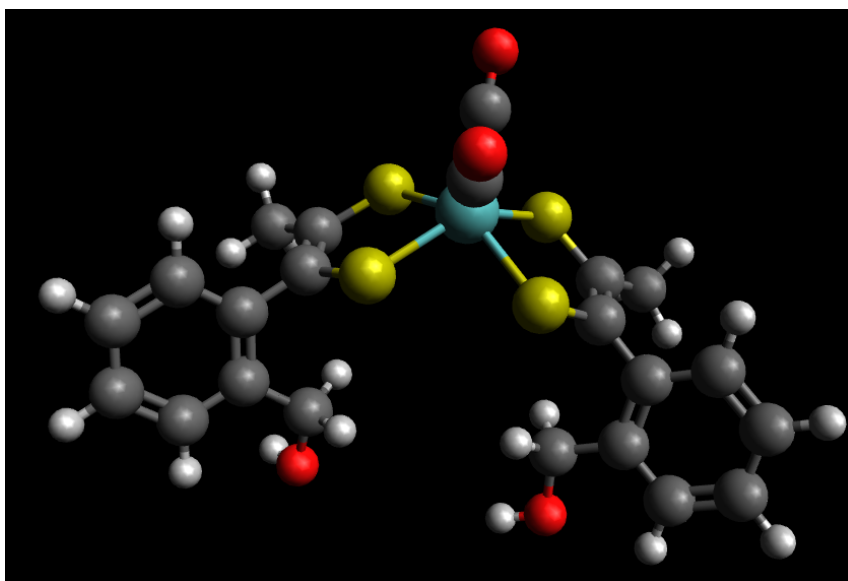


Figure 4.4: Ball and stick representation of the energy minimised geometry of *cis* down,down *o*-78.

It is apparent that in the up,up isomers there is no possibility of hydrogen bonding. However, whilst hydrogen bonding seem to look possible in the down down isomer, the distance between the closest hydrogen and oxygen atoms is 4.452 Å. Thus there is very little danger of intramolecular hydrogen bonding, deactivating the proton donors.

4.3.2 Comparison of isomers

With the initial survey of all of the geometric isomers of *o*-**78**, we turned our attention to *meta* and *para* isomers. As detailed above, there is negligible energy difference between all the isomers. As we are most interested in the *cis* up,up configuration, we chose to explore this arrangement in the *meta* and *para* isomers. Table 4.3 shows the CO stretches in the positional isomers; plots of the simulated infrared spectra are shown in Figure 4.5, with the real data for comparison in Figure 4.6. All three show the expected asymmetrical two peak structure typical for a *cis* CO arrangement. It is notable that the spectra for the *meta* and *para* isomers are virtually identical. There is no significant difference between the metal geometry in the three systems (Figures 4.3, 4.7 and 4.8). It is therefore difficult to assign the change in IR to a specific molecular feature. Notably, the simulated IR data show a higher intensity for the symmetric stretch. This contrasts with the typical expectation, where the antisymmetric stretch is expected to be more intense.

Table 4.3: Computational results for positional isomers of **78**.

Entry	Isomer	$\tilde{\nu}_{\max}/\text{cm}^{-1}$			
		Simulated		Experimental	
1	<i>ortho</i>	1953	1993	1983	2035
2	<i>meta</i>	1947	1988	—	2039
3	<i>para</i>	1948	1989	1983	2044

Table 4.3 compares simulated data with the experimental data reported in Chapter 3. As anticipated from the simulation of model systems (Table 4.1), the

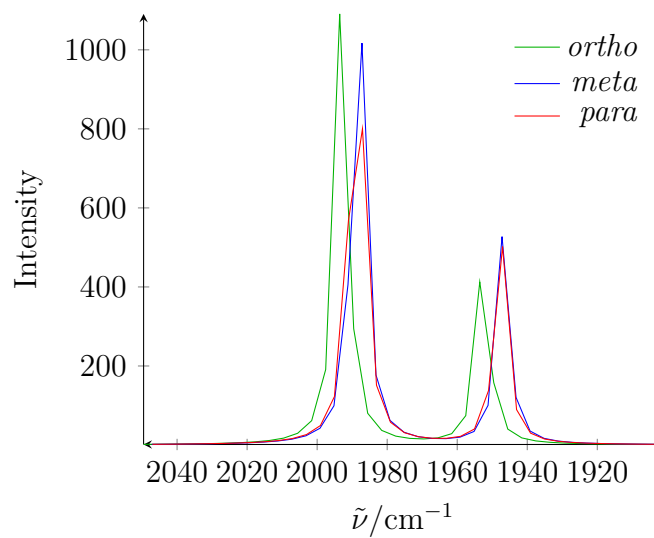


Figure 4.5: Simulated IR spectra for positional isomers of **78**.

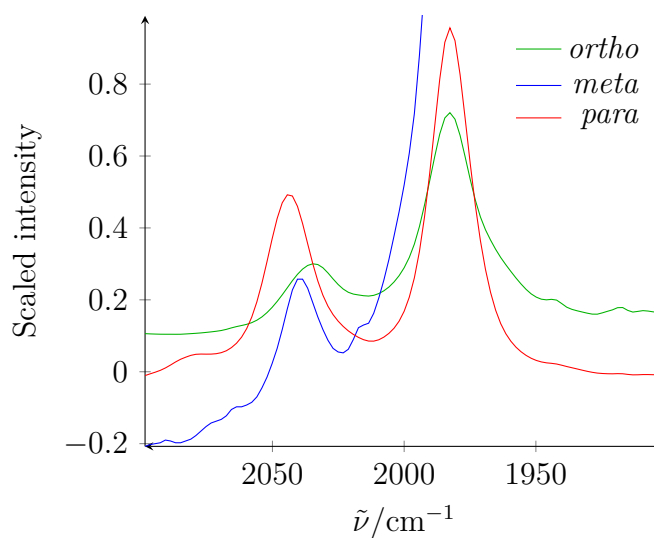


Figure 4.6: Experimental IR spectra for positional isomers of **78**; data for *meta* isomer are truncated due to the presence of large amounts of unreacted starting material.

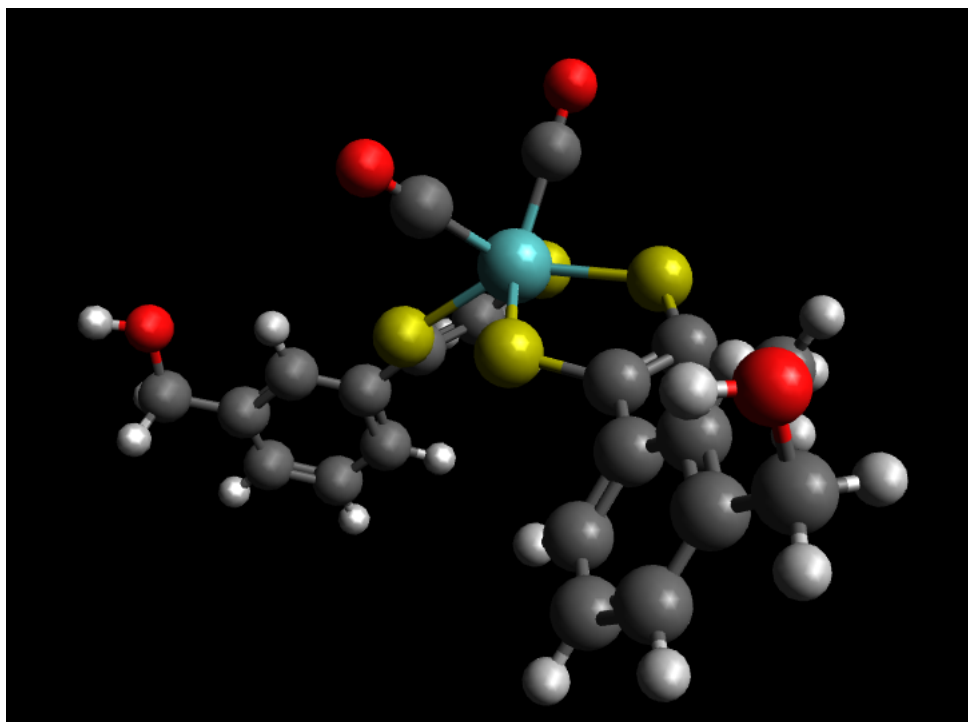


Figure 4.7: Ball and stick representation of the energy minimised geometry of *cis* up,up *m*-78.

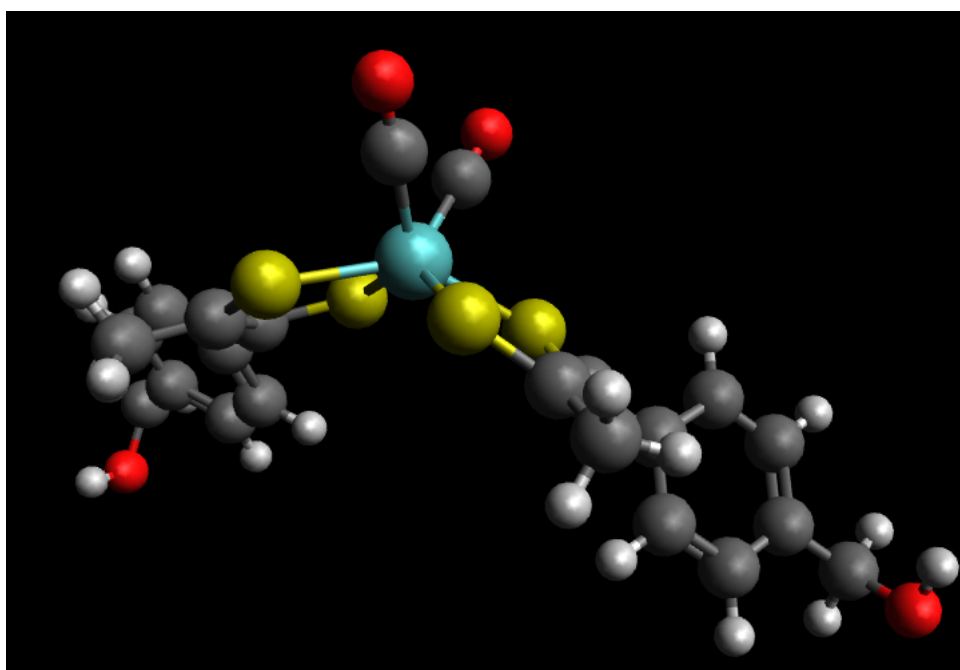


Figure 4.8: Ball and stick representation of the energy minimised geometry of *cis* up,up *p*-78.

absolute values are significantly displaced. However the correlation between simulated and experimental values as shown in Figure 4.9 is linear with $R^2 = 0.9698$. For the *meta* isomer only one band was visible experimentally due to the presence of unreacted starting material; it was correlated to the higher energy simulated band. This is good evidence that the earlier synthetic work was successful, and suggests that the calculations here are useful in identifying future targets.

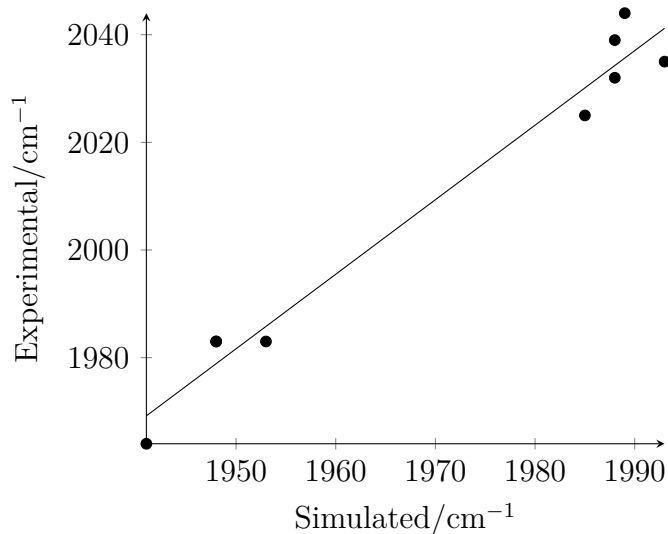


Figure 4.9: Comparison for simulated and experimental infrared values.

4.3.3 Reduced states

In order for catalysis to occur, electron transfer will be required to the neutral dithiolene molecules. To explore the impact of this process on the geometry of our complexes, we extended our DFT calculations to the reduced states.

Reduction to both the one-minus and two-minus states could be simulated by minor adjustment of the previously obtained neutral structures. In the one-minus case, this necessitated use of an unrestricted functional due to the unpaired electron density. The resulting infrared is summarised in Table 4.4, and key geometric parameters are listed in Table 4.5.

As anticipated, reduction of the metal centre leads to a significant shift in both the metal geometry and resulting infrared stretching frequencies. As was the case in the

Table 4.4: Computational results for reduced states of **78**.

Entry	Isomer	$\tilde{\nu}_{\max}/\text{cm}^{-1}$			
		one-minus		two-minus	
1	<i>ortho</i>	1874	1934	1794	1873
2	<i>meta</i>	1866	1928	1789	1870
3	<i>para</i>	1868	1929	1791	1870

Table 4.5: Computational results for different states of *o-78*, *m-78* and *p-78*.

Entry	Charge	Isomer	CO bond length/Å		C–Mo–C Angle/°
1	0	<i>ortho</i>	1.159	1.159	82.4
2	0	<i>meta</i>	1.160	1.160	82.3
3	0	<i>para</i>	1.160	1.160	82.3
4	−1	<i>ortho</i>	1.170	1.171	78.2
5	−1	<i>meta</i>	1.171	1.172	78.1
6	−1	<i>para</i>	1.171	1.171	78.2
7	−2	<i>ortho</i>	1.183	1.184	74.4
8	−2	<i>meta</i>	1.186	1.183	73.6
9	−2	<i>para</i>	1.186	1.183	74.1

neutral systems, the *meta* and *para* isomers have very similar infrared values, while those for the *ortho* systems are very slightly higher. This change in spectroscopic data is entirely consistent with bond length simulated which are elongated on reduction. The changes in the C–Mo–C bond angle are a consequence of broader changes in the geometry of the metal centre. The reduced states for *o-78* are illustrated in Figures 4.10 and 4.11. In the neutral and one-minus structure, the four sulphurs are essentially coplanar. In contrast, reduction to the two-minus state leads to significant distortion in the direction of octahedral coordination.

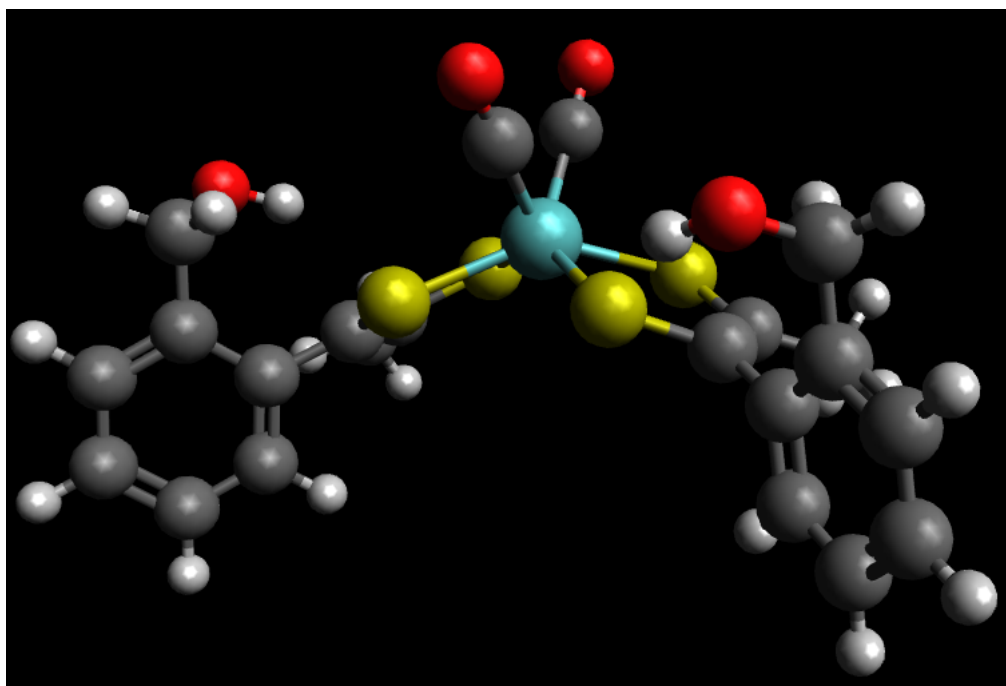


Figure 4.10: Ball and stick representation of the energy minimised geometry of *cis* up,up $o\text{-}78^-$.

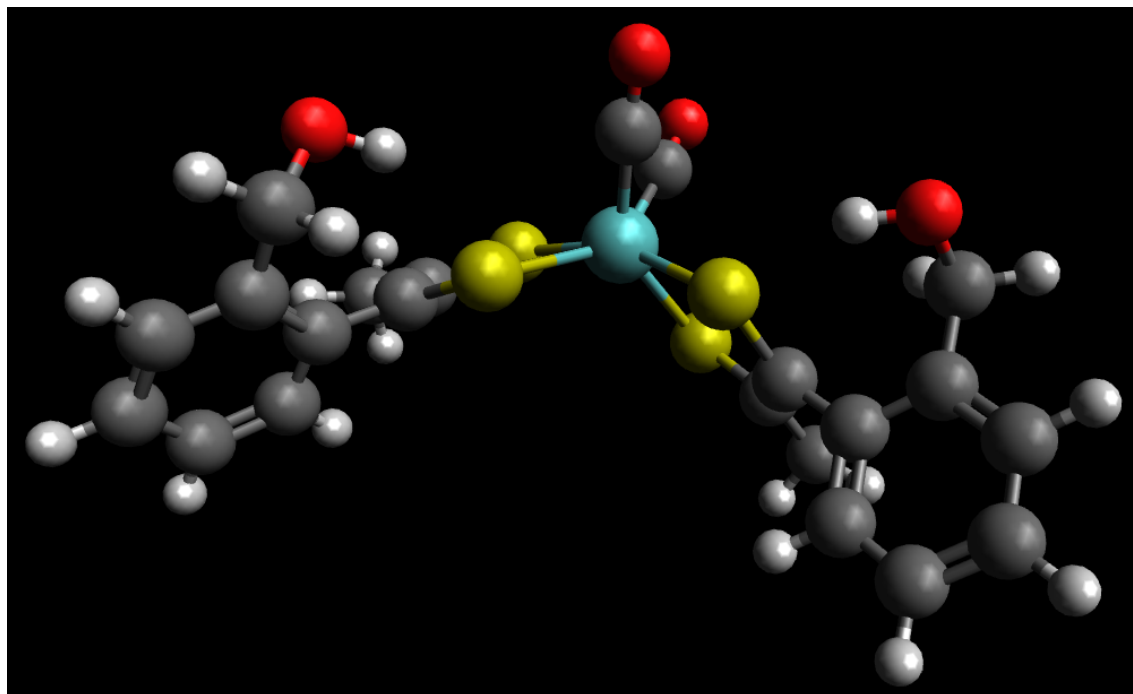


Figure 4.11: Ball and stick representation of the energy minimised geometry of *cis* up,up $o\text{-}78^{2-}$.

Following our observation of the change in geometry, we considered the possibility that this could lead to intramolecular hydrogen bonding in the *cis* down,down isomer. To investigate this we decided to simulate for the reduced states of *o*-**78** *cis* down down systems (Figures 4.12 and 4.13). The distances between the two oxygens and oxygen and hydrogen are clearly within the range for a hydrogen bond as shown in Table 4.6, notably shorter than the corresponding neutral complex. This may suggest that a a more rigid ligand framework may be required to avoid any intramolecular hydrogen bonding.

Table 4.6: Hydrogen bonding distance for *cis* down,down *o*-**78**.

Entry	Charge	Distance/Å	
		O · · · O	O · · · H
1	0	5.326	4.452
2	-1	2.950	1.970
3	-2	2.796	1.813

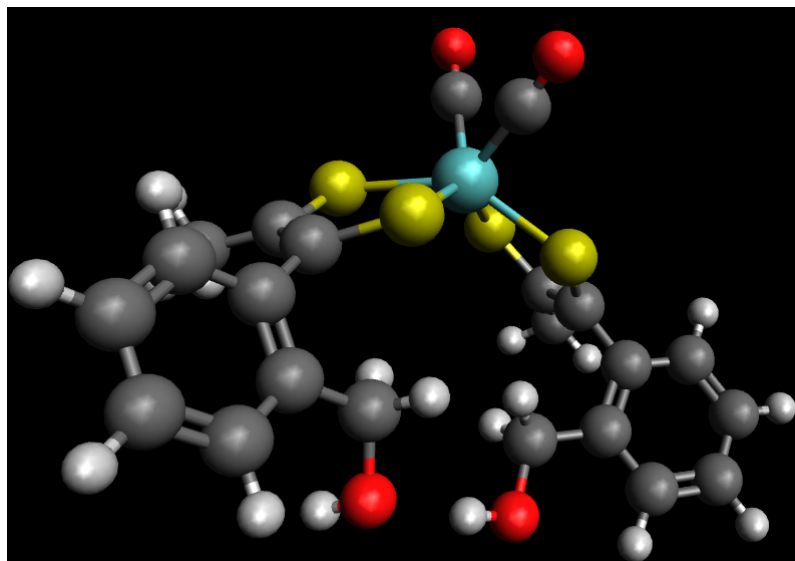


Figure 4.12: Ball and stick representation of the energy minimised geometry of *cis* down,down $o\text{-78}^-$.

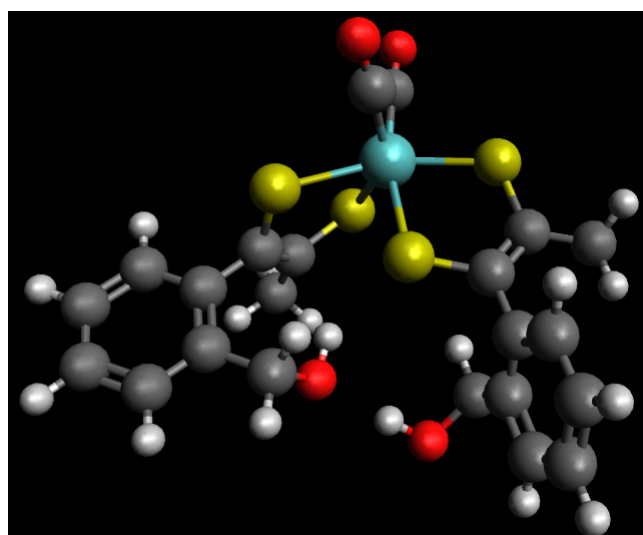


Figure 4.13: Ball and stick representation of the energy minimised geometry of *cis* down,down $o\text{-78}^{2-}$.

4.3.4 Additional carbon chain length

The final area investigated by DFT was the possibility that a longer alkyl chain could place the hydroxy group in optimal location close to the metal centre. Two isomers were investigated: cis up up and cis down down, **83** (Figure 4.14). These required more computational cycles to reach convergence, particularly for the up,up isomer. The optimised geometries show that in the up up case neither hydroxy group approaches the metal centre closely (Figure 4.15). In the absence of a bound substrate this may be unsurprising. For the down down isomer, there is clear evidence for hydrogen bond between the two side chain; the O · · · O distance is 2.894 Å and O · · · H distance is 1.912 Å (Figure 4.16). The down,down isomer is favourable by around 7 kJ mol⁻¹, unlikely to exclude either isomer in solution.

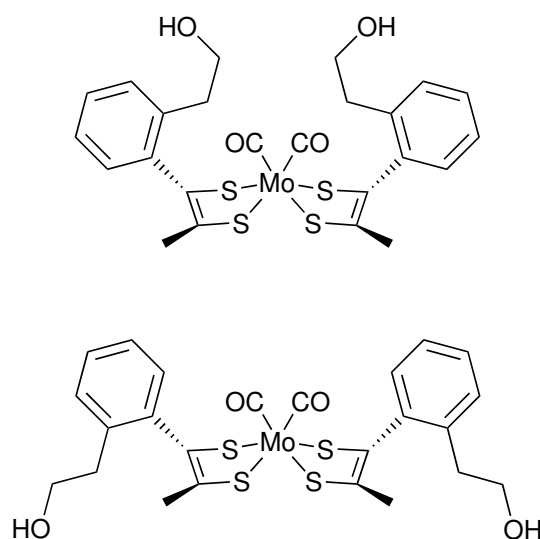


Figure 4.14: Molybdenum dithiolene with extended chain length (**83**).

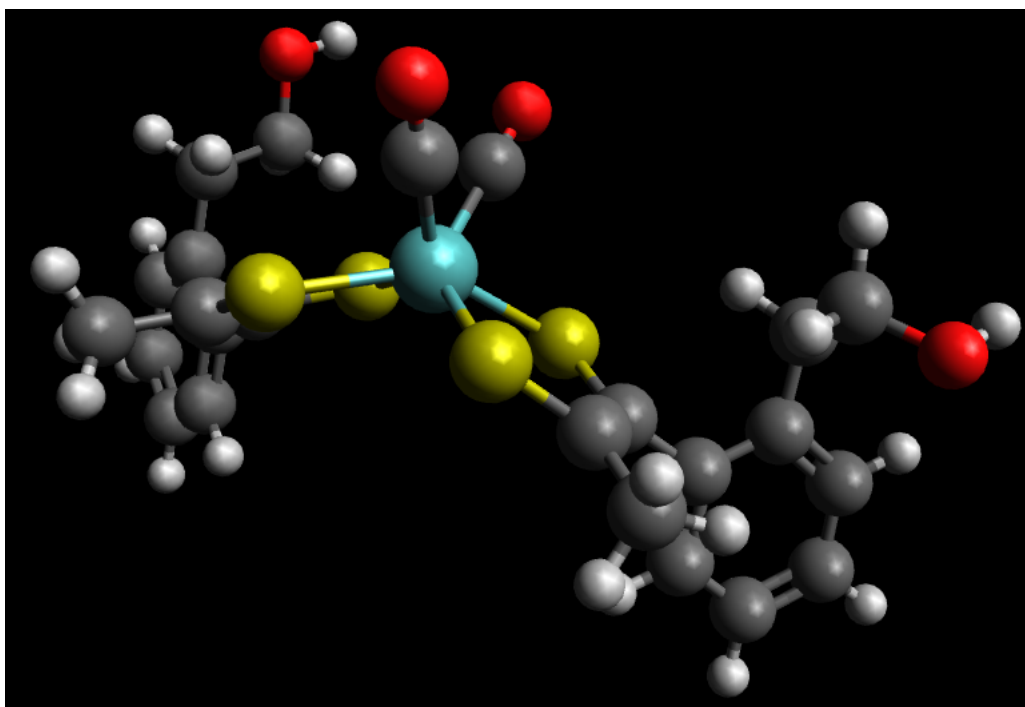


Figure 4.15: Ball and stick representation of the energy minimised geometry of *cis* up,up **83**.

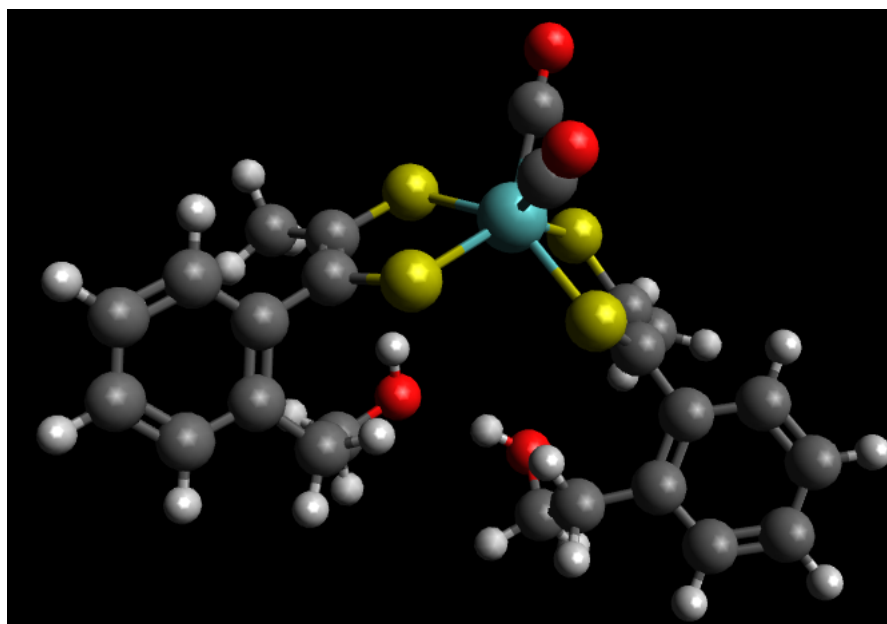


Figure 4.16: Ball and stick representation of the energy minimised geometry of *cis* down,down **83**.

4.4 Conclusions

Computational simulations of a range of molybdenum dithiolenes can be achieved using the ADF package and BP86 functional. The optimised geometries for the hydroxylated systems appear reasonable. Simulated infrared frequencies are systematically displaced from the experimental values but correlation is good. This suggests that prediction of the structures and spectra of other potential targets should be achievable.

Reduction of the neutral complexes leads to the anticipated shift in IR peaks. In the two-minus state the geometry of the metal centre distorts toward octahedral. This allows for hydrogen bonding in the *cis* down,down isomer. However, energy differences between isomers appear to be small and so in solution, it is likely that the desired up,up arrangements exist in equilibrium.

Chapter 5

Electrochemistry of nickel and molybdenum dithiolene complexes

5.1 Introduction

5.1.1 Electrochemical methods

Electrochemistry is a powerful way to examine behaviour of redox active species, from molecular organic systems through transition metal complexes to inorganic solids.¹³⁸ Solution electrochemistry is a versatile technique as fundamentally it requires only that two electrodes can be introduced into a conductive solution.

Possibly the most widely used electrochemical method for molecular species is cyclic voltammetry (CV). The core idea of this approach is to apply a linear potential sweep and to observe the resulting current. The total amount of material required is minimal as the redox processes only take place within the diffusion layer around the working electrode. This electrode is normally a disc with a diameter of the order of couple of millimetres.

In a standard CV experiment, the linear potential sweep runs from a starting potential to a vertex at which point the sweep is reversed and the potential returns to the starting point. Provided the scan rate is sufficiently high, the result is

that electrochemical change can be fully reversible. The dependence of current response on scan rate therefore carries important information about the lifetimes of electrochemically generated species.

The model fully reversible redox couple in non-aqueous solvent is ferrocenium/ferrocene (Figure 5.1). This illustrates the standard features of a solution CV. The forward and reverse peaks are separated by around 60 mV at room temperature, and the peaks have an asymmetrical shape due to diffusion control.

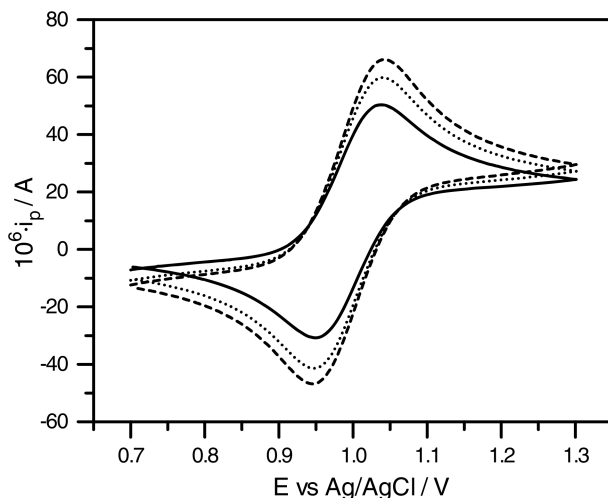


Figure 5.1: Cyclic voltammogram of ferrocene in MeCN at a range of scan rates. Modified with permission from reference [139]. Copyright © 2007 Springer

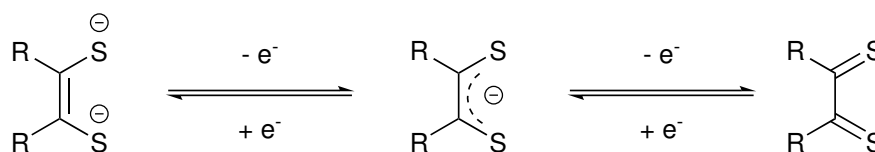
Where chemical change takes place following a redox process, the reverse wave will either shift or be reduced in magnitude/disappear. Commonly, the rate of chemical change is comparable to the time taken to reverse the CV sweep. This means that the size and position of the reverse wave will show a dependence on scan rate. It is therefore very common to assess reversibility by plotting peak currents against square root of scan rates. The square root dependence arises from the Randles–Ševčík equation

$$i_{\text{peak}} = -0.4463nF \left(\frac{nF}{RT} \right)^{\frac{1}{2}} c_0^{\infty} \sqrt{D\nu}$$

where i_{peak} is the peak current, n is the number of electrons passed, F is the Faraday constant, R is the gas constant, T is the temperature, D is the diffusion coefficient, c_0^{∞} is the bulk concentration and ν is the scan rate.

5.1.2 Nickel dithiolenes

The term dithiolene is commonly used to refer to three possible redox states of the same core structure (Scheme 5.1).^{117,140} The redox non-innocence of the dithiolenes means that their transition metal complexes have the potential for rich electrochemical behaviour. Identifying the redox state of the metal in these complexes is not always straight forward and often relies on supporting evidence such as DFT, electron paramagnetic resonance (EPR) or crystal structures.^{119,141}



Scheme 5.1: Redox states of dithiolene

Early studies on simple nickel palladium and platinum dithiolenes were carried out by Boyd and co-workers.¹⁴² Reduction of Ni(Ph₂C₂S₂)₂ (**84**, Figure 5.2) shows two (quasi)reversible reduction waves (Figure 5.3). The first reduction wave leads to an unpaired electron delocalised over both ligands and to some extent the central metal ion. The second reduction is also assigned as ligand based, and so nickel remains in oxidation state two. The electrochemistry of other simple nickel dithiolenes follows a similar pattern.

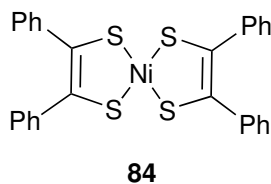


Figure 5.2: Simple nickel bis(dithiolene) used by Bowmaker.

More recently Artero has explored electrochemical proton reduction at **84** and more elaborate nickel bis(dithiolene) centres (Figure 5.4).^{143,144} In all these systems, electrocatalysis occurs at potentials more negative than the second ligand based wave, suggesting that it occurs at the metal centre (Figure 5.5).

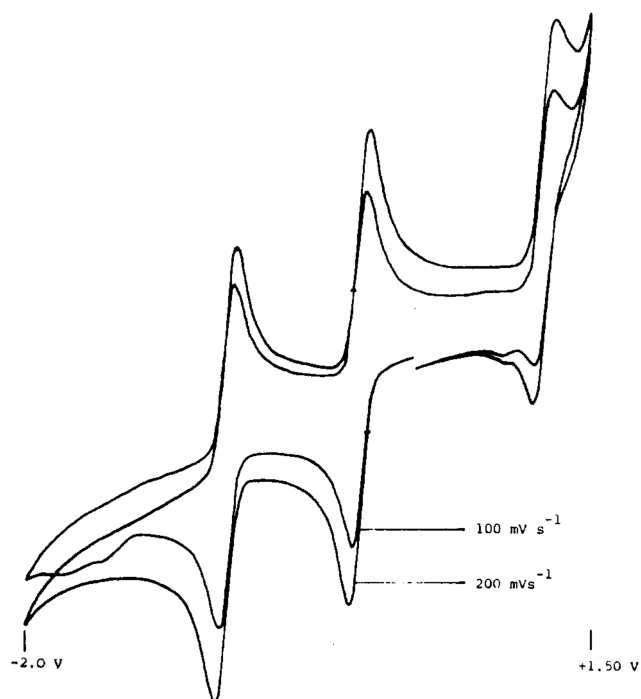
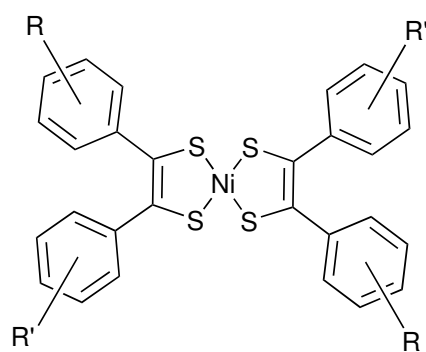


Figure 5.3: Cyclic voltammogram of the redox processes for **84** at 100 mV s^{-1} and at 200 mV s^{-1} . Modified with permission from reference [142]. Copyright © 1983 American Chemical Society



85a $R = \text{H}, R' = \text{OMe}$
85b $R = R' = \text{OMe}$

Figure 5.4: Nickel bis(dithiolenes) used by Artero.

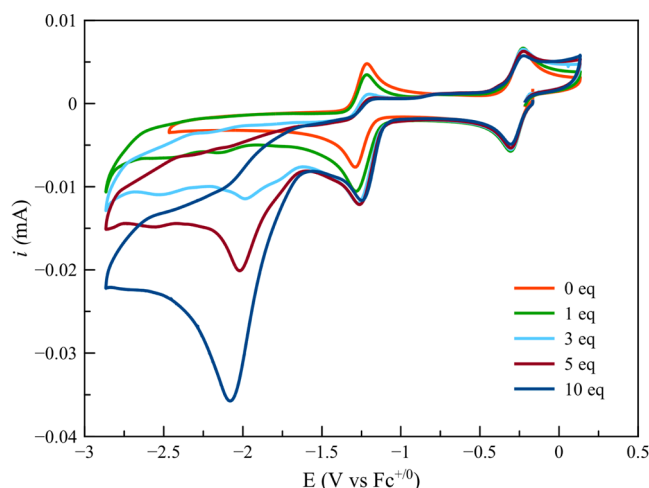


Figure 5.5: Cyclic voltammogram of **85** in the presence of increasing amount of acid. Modified with permission from reference [144]. Copyright © 2015 American Chemical Society

5.1.3 Molybdenum dithiolenes

There is very limited literature on the electrochemical behaviour of molybdenum dithiolene bis carbonyls. This reflects the narrow range of published structures available for comparison.

Holm has reported electrochemical studies on $M(\text{CO})_2(\text{Me}_2\text{C}_2\text{S}_2)_2$ (Figure 5.6) for both molybdenum and tungsten.¹¹⁹ As for nickel, reduction of these species show two reversible waves (Figure 5.7). On the basis of DFT and EPR, Holm assigns the reduction to orbitals of principally ligand character. He states that

We are inclined to the view that metal oxidation state descriptions in molecules such as $[\text{M}(\text{CO})_2(\text{S}_2\text{C}_2\text{Me}_2)_2]^{0.1-}$ and $[\text{M}(\text{S}_2\text{C}_2\text{Me}_2)_3]^{0.1-}$ are of questionable heuristic value.

In the same paper, Holm also reports the electrochemistry of the corresponding tris dithiolene complexes. The same largely ligand based behaviour is observed (Figure 5.8).

Beyond the bis CO complexes, there has been some examination of molybdenum oxo bis(dithiolenes). Most notably Fontecave and co-workers have reported photo- and electroreduction of protons using a molybdenum oxo complex featuring two

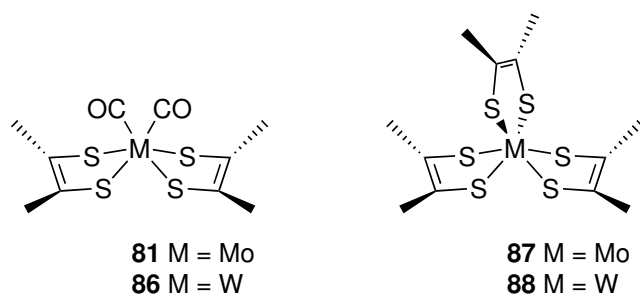


Figure 5.6: Symmetrical molybdenum and tungsten complexes studied electrochemically by Holm.

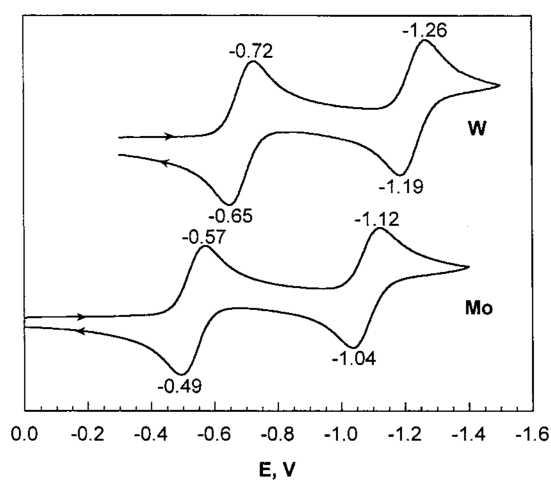


Figure 5.7: Cyclic voltammogram of $M(\text{CO})_2(\text{Me}_2\text{C}_2\text{S}_2)_2$, produced by the Holm group. Modified with permission from reference [119]. Copyright © 2001 American Chemical Society.

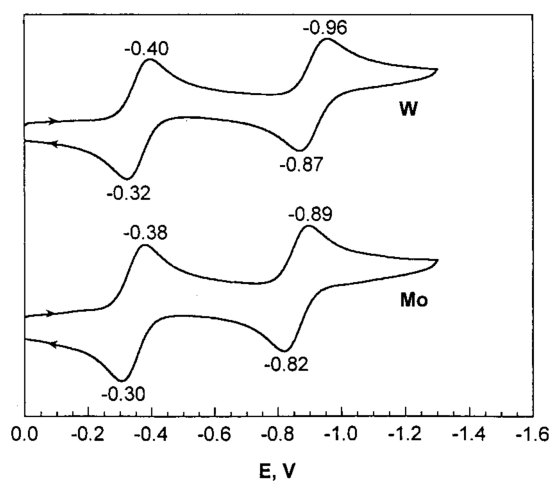


Figure 5.8: Cyclic voltammogram of $M(\text{Me}_2\text{C}_2\text{S}_2)_3$, produced by the Holm group. Modified with permission from reference [119]. Copyright © 2001 American Chemical Society

ligands which mimic the dithiolenes present in the active site of FDH (Figure 3.2).¹⁴⁵ This system shows only one reversible reduction wave (at -0.19 V vs Ag/AgCl) assigned as the Mo(V)/Mo(IV) couple (Figure 5.9). Electrocatalysis in this system occurs at potential significantly below that of the reversible wave.

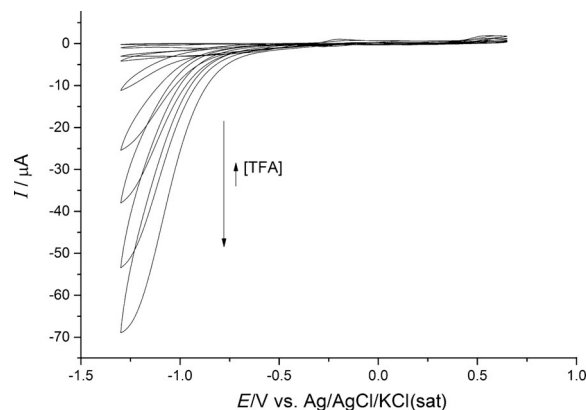


Figure 5.9: Cyclic voltammogram of Fontecave's catalyst in the presence of increased concentration of acid. Modified with permission from reference [145]. Copyright © 2015 Wiley-VCH/GDCh

5.2 Nickel bis(dithiolenes)

5.2.1 *Ortho* complex

As detailed above, nickel bis(dithiolenes) show varied electrochemical behaviour on reduction. The formally nickel(IV) centre can be reduced to formally nickel(II), although the involvement of the dithiolenes means that the true state is more complex. With three novel nickel complexes synthesised, we decided to explore their electrochemistry. All three complexes are readily soluble in acetonitrile and show some solubility in dichloromethane. This has allowed us to explore the effect of solvents on these systems.

Reduction of *o*-**77** in MeCN gave two reduction waves as anticipated (Figure 5.10). The first reduction wave occurs at -0.395 V vs Fc^+/Fc and shows reversible behaviour across a range of scan rates. The second wave occurs at -1.226 V vs Fc^+/Fc and is

quasi reversible. At higher scan rates, the forward and reverse waves are of similar height. But at lower scan rates it is clear that the reverse wave is much smaller than the forward one. This suggests that decomposition of the reduced species takes place on the seconds time scale. Plots of peak currents against the square root of scan rate shows both peaks are diffusion controlled, demonstrated by the linear relationship (Figure 5.11).

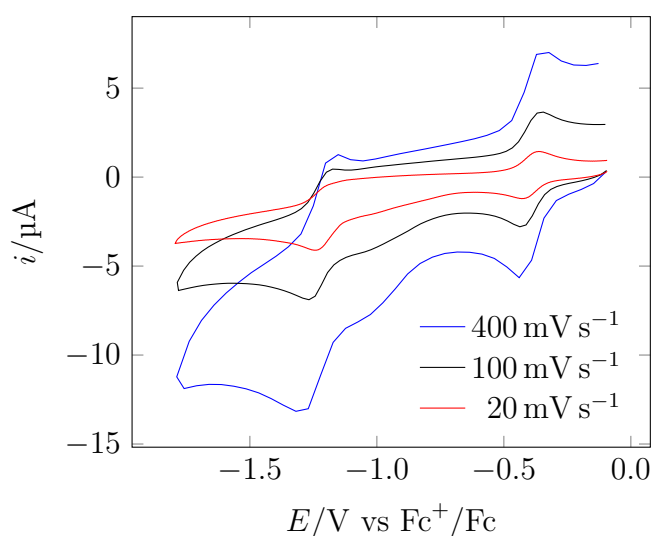


Figure 5.10: Cyclic voltammogram of *o*-**77** in MeCN/ NBu_4BF_4 (100 mM).

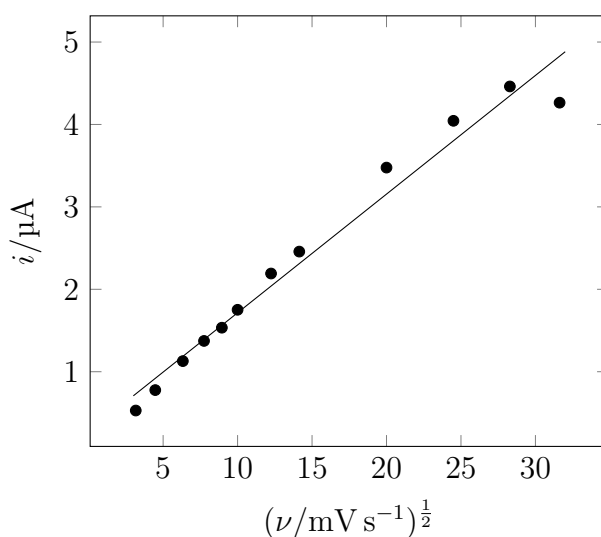


Figure 5.11: Plot of absolute peak current against square root of scan rate for the first reduction wave of *o*-**78** in MeCN/ NBu_4BF_4 (100 mM).

Switching to dichloromethane, the first wave (-0.480 V) remains fully reversible

as in acetonitrile (Figure 5.12). The second wave retains some evidence for quasi reversibility. However, this is less pronounced than in acetonitrile. This may suggest that decomposition can occur via a solvent dependent pathway.

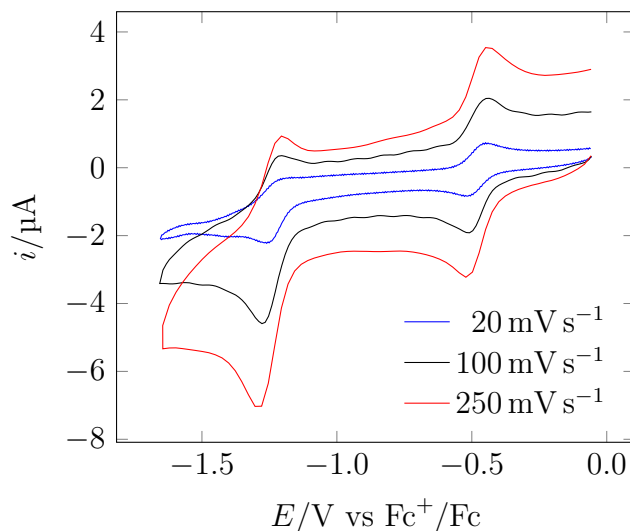


Figure 5.12: Cyclic voltammogram of *o*-**77** in $\text{CH}_2\text{Cl}_2/\text{NBu}_4\text{BF}_4$ (100 mM).

5.2.2 *Meta* complex

In acetonitrile the *meta* complex behaves similarly to the *ortho* (Figure 5.13) with two reversible peaks: the first wave at -0.384 V and second wave at -1.274 V . In contrast, three reversible peaks were observed for the same sample when the CV was obtained in dichloromethane (Figure 5.14). The positions of the peaks corresponding to the acetonitrile are at ‘first’ wave at -0.506 V and ‘second’ wave at -1.297 V . The additional peak falls around zero and is clearly of the same order of magnitude as the two other peaks. Therefore, it is unlikely to have originated as a result of foreign materials. As the metal centred waves seem unaffected, the most likely location for this reduction is the pendent hydroxy group.

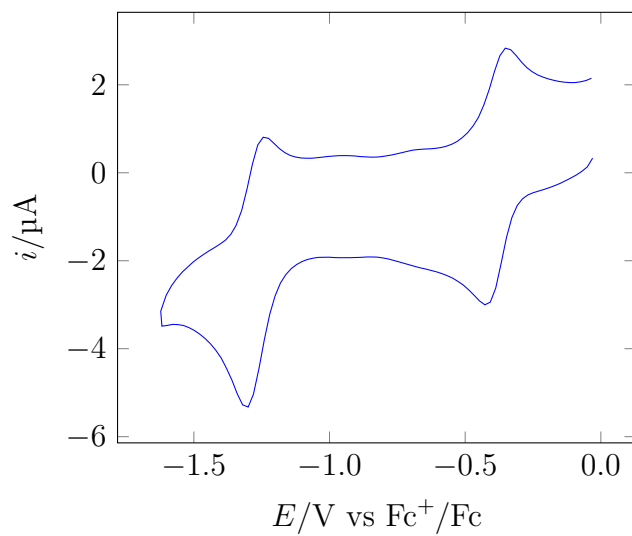


Figure 5.13: Cyclic voltammogram of *m*-**77** in MeCN/ NBu_4BF_4 (100 mM) at 100 mV s^{-1} .

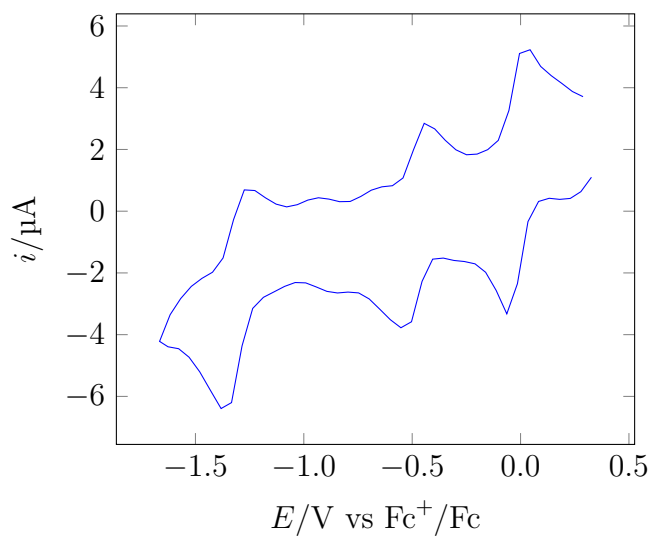


Figure 5.14: Cyclic voltammogram of *m*-**77** in $\text{CH}_2\text{Cl}_2/\text{NBu}_4\text{BF}_4$ (100 mM) at 200 mV s^{-1} .

5.2.3 *Para* complex

Initial voltammetry of the *para* complex in acetonitrile reproducibly revealed only one significant wave at -1.281 V (Figure 5.15), corresponding to the second reduction wave seen in other complexes. This was unaffected by scan rates. Focussing on the one wave observed, Figure 5.16, it is apparent that the peak does not exhibit any significant scan rate dependency. The peak separation is of the order of 170 mV ruling out the possibility of a two-electron process: a standard Nernst analysis requires a separation of two electrons to be around 30 mV.¹⁴⁶ In other solvents two peaks were observed (see below): thus any explanation must involve acetonitrile.

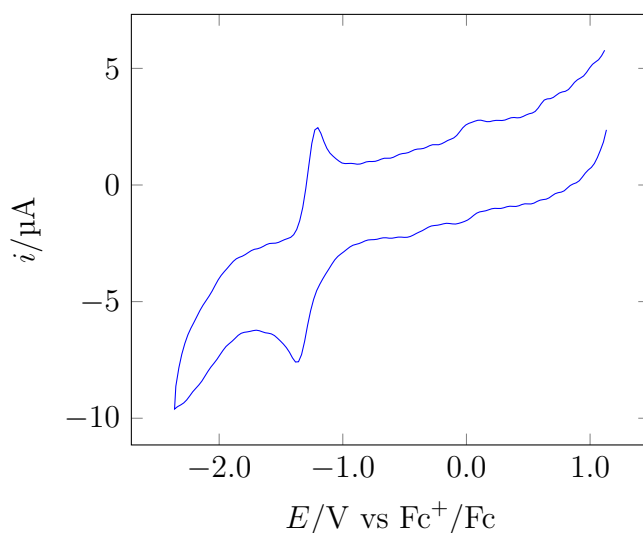


Figure 5.15: Wide sweep cyclic voltammogram of *p*-**77** in MeCN/ NBu_4BF_4 (100 mM) at 100 mV s^{-1} .

In contrast to the behaviour in acetonitrile, in both dichloromethane and dimethyl formamide two peaks were observed (Figure 5.17 and 5.18). These appeared at potentials similar to those of the other isomers. In dimethyl formamide these come at -0.427 V and -1.406 V, and in dichloromethane at -0.399 V and -1.334 V. In dichloromethane, the second wave is clearly irreversible even at higher scan rates.

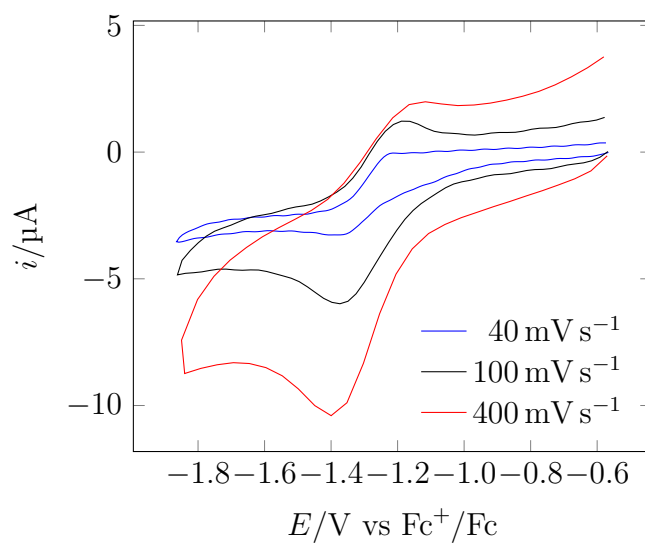


Figure 5.16: Cyclic voltammogram of *p*-**77** in MeCN/NBu₄BF₄ (100 mM).

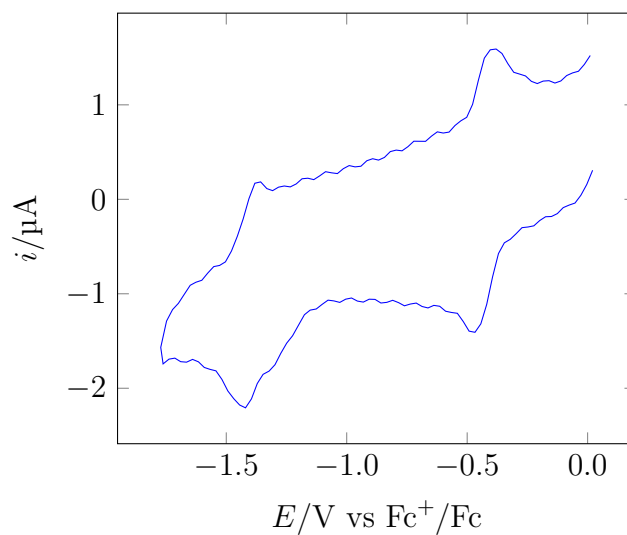


Figure 5.17: Cyclic voltammogram of *p*-**77** in DMF/NBu₄PF₆ (100 mM) at 100 mV s⁻¹.

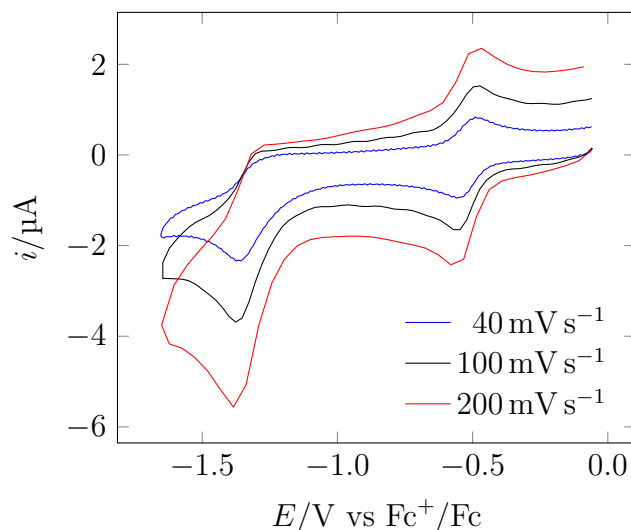


Figure 5.18: Cyclic voltammogram of *p*-**77** in $\text{CH}_2\text{Cl}_2/\text{NBu}_4\text{BF}_4$ (100 mM) at 100 mV s^{-1} .

5.3 Molybdenum dithiolenes

5.3.1 Molybdenum tris(dithiolenes)

As the tris(dithiolene) complex (**87**, Figure 5.19) is far easier to access than the major bis(dithiolene) target, we chose to examine its electrochemistry for comparison. As observed with the bis(dithiolene) complex, two peaks are seen (Figure 5.20). The peaks were separated by 184 mV, whilst Holm group observed a peak separation of about 0.52 V for their simple tris(dithiolene).¹¹⁹ This significant change in the peak separation clearly demonstrates that introduction of a phenyl group heavily impacts on the dithiolene ligand. As the dithiolene ligand is redox active, conjugation with an aromatic group could have a significant impact on the electrochemistry on the complex as a whole. This likely merits further investigation with a range of different dithiolenes.

It is apparent that the first reduction wave is fully reversible but the proximity of the two peaks means that it is much less obvious to access the second peak by inspection. Plots of peak current against scan rate shows that the current response is linear against a range of scan rates and that the forward and backward waves for

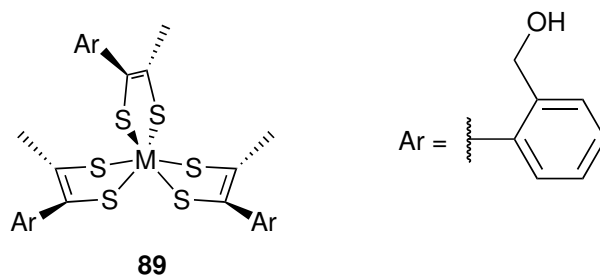


Figure 5.19: Molybdenum (tris)dithiolene complex

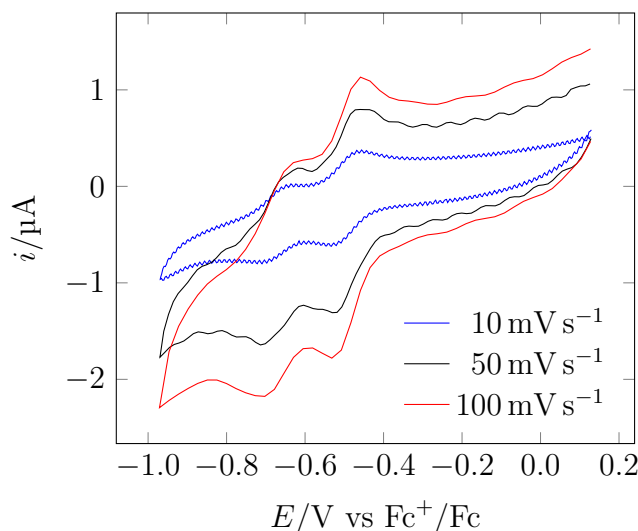


Figure 5.20: Cyclic voltammogram of **89** in $\text{CH}_2\text{Cl}_2/\text{NBu}_4\text{BF}_4$ (100 mM).

the second peak is reversible (Figure 5.21). This is consistent with the robust nature of the tris(dithiolene) complexes.

5.3.2 Molybdenum bis(dithiolenes)

Cyclic voltammetry of *o*-**78** reveals two reversible waves separated by 0.467 V (Figure 5.22), about 100 mV below that of simple dithiolenes reported by the Holm group (0.55 V, Figure 5.7).¹¹⁹ This narrowing of the peak separation can be attributed to the replacement of one of the methyl groups with a phenyl group in the ligand, reflecting the non-innocent nature of the dithiolene ligand in the electrochemistry. It seems unlikely that the hydroxy group is implicated in this change as it is electronically isolated from the metal centre.

With the basic chemistry of *o*-**78** established, we turned our attention to catalysis,

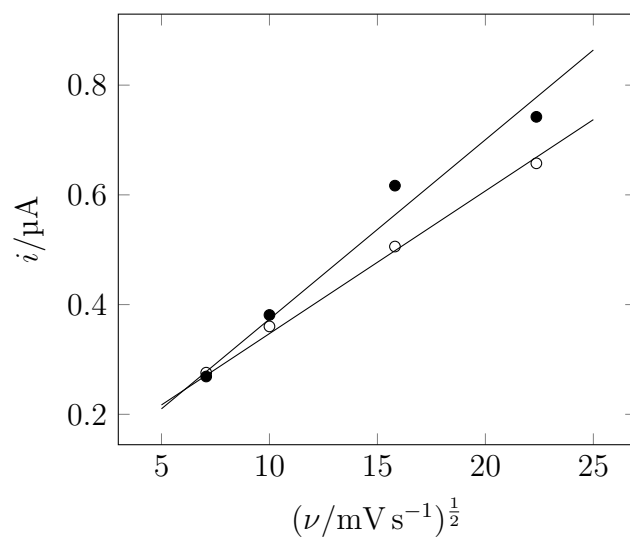


Figure 5.21: Plot of absolute peak current against square root of scan rate for the first reduction wave of *o*-**77** in $\text{CH}_2\text{Cl}_2/\text{NBu}_4\text{BF}_4$ (100 mM). Filled circles are for forward waves and empty circles are for backward waves.

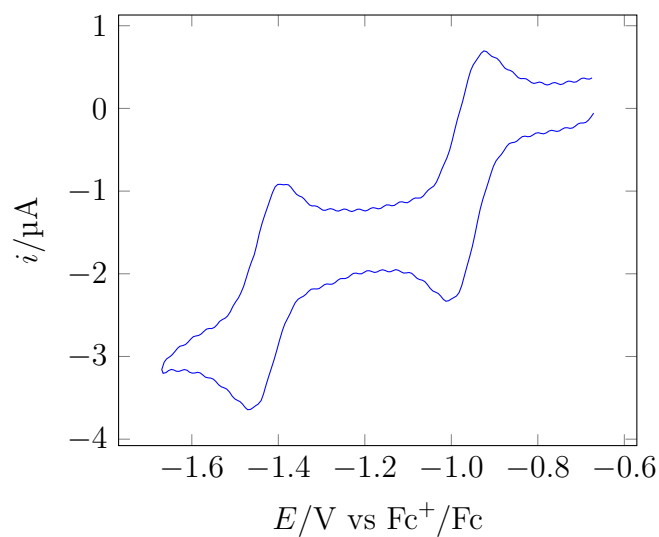


Figure 5.22: Cyclic voltammogram of *o*-**78** in $\text{CH}_2\text{Cl}_2/\text{NBu}_4\text{BF}_4$ (100 mM) at 25 mV s^{-1} .

specifically proton reduction. Fontecave has demonstrated electroreduction of protons at molybdenum oxo dithiolenes,¹⁴⁵ and we hypothesised our complex could also be active.

Addition of equivalents of trifluoroacetic acid (TFA) to a solution of *o*-**78** in dichloromethane revealed electrocatalytic processes taking place at both reduction waves (Figure 5.23). It is clear that the first reduction wave becomes more negative as acid is added. The behaviour of the second wave is much less defined as the concentration increases above 20 equivalent. Up to 20 equivalent, the second peak shifts to a more positive position (Figure 5.24). At the highest acid concentration, the two peaks appear to merge.

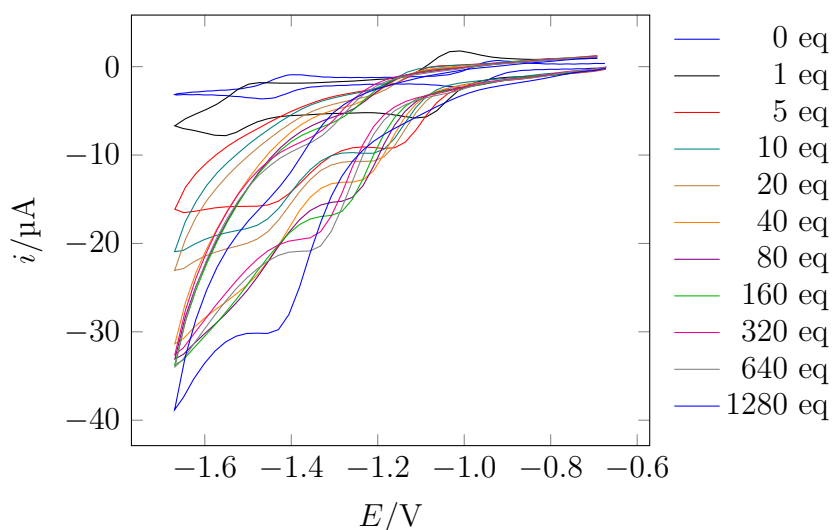


Figure 5.23: Cyclic voltammogram of *o*-**78** in $\text{CH}_2\text{Cl}_2/\text{NBu}_4\text{BF}_4$ (100 mM) in presence of trifluoroacetic acid at 100 mV s^{-1} .

Examining the peak currents (Figure 5.25), it is clear that in both cases the currents observed are approaching plateaux. Current at the second wave rises rapidly, indicating a fast electrochemical reduction. Above 40 equivalents of acid, it was not possible to identify clear peak maxima, but visually it is apparent that the current has not risen significantly. The peak current for the first wave rises more slowly, approaching a maximum above 600 equivalents.

In Fontecave's systems protonation at the oxo is a possible pathway, followed by

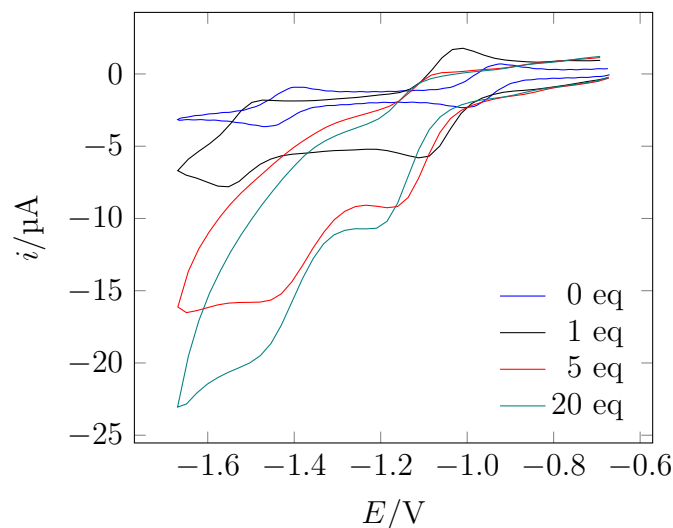


Figure 5.24: Cyclic voltammogram of *o*-**78** in $\text{CH}_2\text{Cl}_2/\text{NBu}_4\text{BF}_4$ (100 mM) in presence of selected concentration of trifluoroacetic acid at 100 mV s^{-1} .

protonation at the metal centre.¹⁴⁵ This pathway is not available to us. Protonation at the metal, at the alcohol or at sulphur are all plausible. Further studies, including computational simulations will be required to elucidate the full mechanistic detail. One might speculate that protonation at the metal leads to hydrogen bonding by the hydroxy group which opens up a facile pathway for hydrogen production.

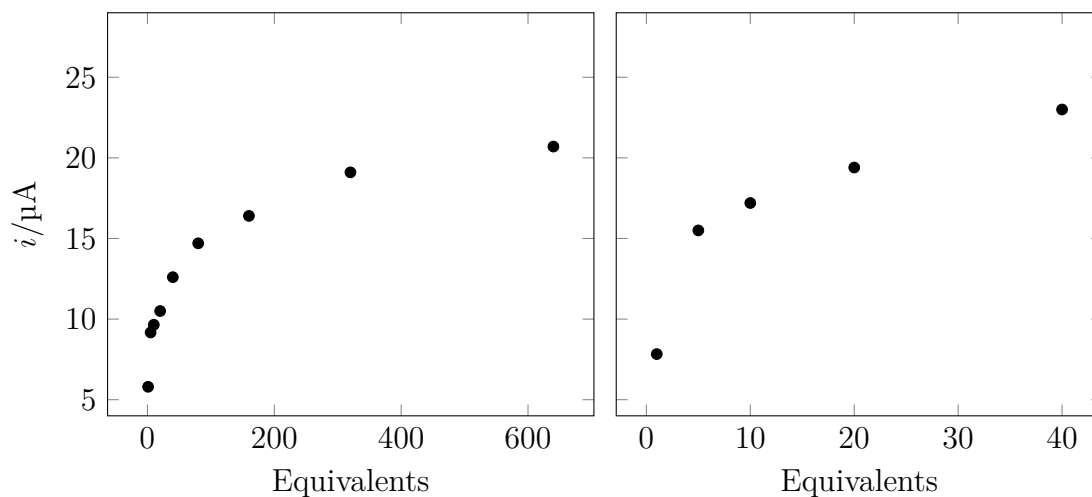


Figure 5.25: Plot of absolute peak current against equivalents of TFA for reduction waves of *o*-**78** in $\text{CH}_2\text{Cl}_2/\text{NBu}_4\text{BF}_4$ (100 mM). Left: First wave; Right: Second wave.

5.4 Conclusion

Cyclic voltammetry of all three nickel bis(dithiolene) complexes exhibit two broadly reversible reduction waves. However, only in the case of the *ortho* isomer can these two waves and only these two waves be observed in both acetonitrile and dichloromethane. The *meta* and *para* isomers both show solvent dependent characteristics, which likely merit further study.

The molybdenum dithiolene complexes show the anticipated pair of reversible reduction waves for both the bis- and tris(ligand) complexes. It is notable that the peak separation for both bis- and tris(dithiolene) complexes are smaller than those of the systems reported by Holm. The peak separation in tris(dithiolene) molybdenum complex is the narrowest of the ones observed for our target complexes.

Electrocatalytic hydrogen production was achieved in the bis molybdenum complex. The data revealed two competing pathways, although the nature of the mechanism requires further studies.

Chapter 6

Conclusions

We explored two different avenues to synthesise small novel molybdenum nitrogen complexes to activate nitrogen. Our efforts to access molybdenum nitrogen complex supported by *N*-heterocyclic carbene was riddled with many challenges. Attempts to synthesise molybdenum nitrogen complex supported either pincer carbene or mono carbenes and phosphines were both unsuccessful. This could be due to the oxidation states targeted in these systems; Mo(III) and Mo(II).

The second approach we considered was to access molybdenum nitrogen complex supported by bidentate phosphine ligand, known as PNP ligand. This route was also challenging, not least because of the extreme air sensitivity of our target systems. We have found that utilising a mercury based bubbler instead of a silicon based one prolonged the lifetime metal complexes. We have successfully synthesised molybdenum nitrogen complex supported by PNP ligand. Crystallographic data showed the presence of both mono (**57c**) and bis (**58c**) PNP ligand on the metal complex. Surprisingly enough, IR data revealed stronger bond in the bound nitrogen in the bis PNP metal complex, **58a** and **58b** than in mono PNP metal complexes **57a** and **57b**. Further investigation is required to successfully isolate mono and bis coordinated metal complex.

We aimed to access a simple and quick route to molybdenum bis carbonyl

complexes and then intended to tune the ligand when on the complex. Our attempts deprotect the pendant hydroxyl group once coordinated to molybdenum has been unsuccessful. We therefore modified our plans and utilised transmetallation. This gave us a dependable and accessible route to bis dithiolene molybdenum carbonyl complexes as the expense of reduction in yield by half. Our target bis dithiolene complexes were extremely sensitive to CO loss. We have found that a even under the most successful conditions in the laboratory, we have synthesised a significant amount of tris dithiolene complexes as a by-product. This may suggest the need to explore alternative molybdenum supporting ligand or molybdenum oxo complexes in the future.

To understand and examine the behaviour of our potential target, we conducted DFT studies. For the purpose of comparison we ran DFT of molybdenum dithiolene complexes reported by Holm, **81** and **82**. We managed to utilise both B3LYP and BP86 for the simulation of **82**, however, only BP86 yielded any results for **81**. According to our simulations the IR of CO bonds were consistently lower by about 35 cm^{-1} from that of the experimental values reported by Holm. We have also noticed the same phenomenon for all three positional isomers of our target complex, **78**, simulated values being lower than that of the experimental values. Further investigation and adjustment of the basis set is required to understand why the simulated values are out from the experimental values.

Lastly, we utilised electrochemistry to examine the behaviour of all three isomers of our nickel complexes and molybdenum carbonyl complex, *o*-**78**. We have observed the reduction waves in acetonitrile and dichloromethane. While both of the two waves were found in both of the solvents for *ortho* complex, the *meta* and *para* showed solvent dependent characteristics. Further investigation is required into the solvent dependency of the *meta* and *para* nickel complexes.

In the case of the molybdenum carbonyl complexes, a pair of reversible reduction waves were observed for bis- and tris(ligand) complexes as anticipated. However, the

peak separation was much smaller than those of systems reported by Holm. It could be due to the fact that our ligand system is more varied than the ones reported by Holm. To establish the real reason behind narrower peak separation, two avenues may be pursued; synthesise more ligand systems similar to our systems and compare that with the electrochemistry of the Holm systems, both prepared in parallel.

We studied the catalytic potential of our novel by molybdenum carbonyl complex. Two competing pathways were observed. The nature and mechanism of the two pathways merits further study.

Chapter 7

Experimental

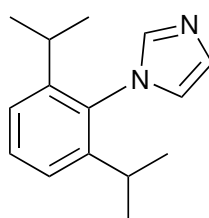
7.1 General

All reactions were conducted under a dry nitrogen atmosphere using standard Schlenk techniques unless otherwise specified. Starting materials were purchased from Aldrich, Alfa Aesar or Strem, and were used without further purification. All glassware and solvents were pre-dried and degassed prior to use. The appropriate drying agents were used for solvent drying: CH_2Cl_2 (CaH_2), tetrahydrofuran ($\text{Na}/(\text{C}_6\text{H}_5)_2\text{CO}$) and acetonitrile (CaH_2). Thin Layer Chromatography (TLC) was carried out using 0.2 mm thick silica gel plates 60F-254 (5735 Merck) with visualization by illumination using UV light ($\lambda = 254 \text{ nm}$). Column chromatography using silica gel from Sigma-Aldrich 60 Å, 230–400 mesh particle size as a stationary phase. Masses were measured using a Fisherbrand analytical balance. FT-IR spectra were recorded using a Bruker Vertex 80 instrument. NMR spectra were recorded on a Bruker AvanceIII 500 operating at ambient temperature; ^1H spectra were collected at 500 MHz, ^{13}C spectra at 126 MHz and ^{31}P spectra at 202 MHz. ^{13}C and ^{31}P spectra were recorded using broad-band proton decoupling. Abbreviations used in NMR analysis are: s (singlet), d (doublet), t (triplet), q (quartet), dd (doublet of doublets), and m (multiplet). Chemical shifts are given in parts per million (δ) and quoted relative to the residual

solvent peak. Elemental analysis was carried out at London Metropolitan University. Mass spectrometry was carried out at the National Mass Spectrometry Facility at the Swansea University or at the University of Sussex. The metal complex $\text{MoCl}_3(\text{THF})_3$ was prepared following the literature method.¹⁰²

7.2 Molybdenum–dinitrogen complexes

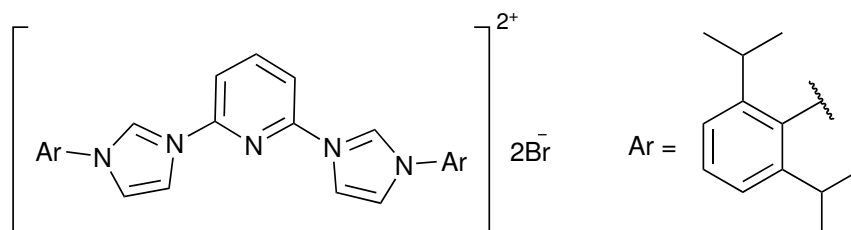
7.2.1 1-(2,6-Diisopropylphenyl)-1*H*-imidazole 41



The method of Johnson was followed.¹⁰⁰ Thiophosgene (13.8 ml, 20.7 g, 180 mmol) was suspended in water (400 ml). Neat 2,6-diisopropylaniline (31.9 ml, 30.0 g, 169 mmol) was added drop-wise and the reaction stirred for two hours. The mixture was extracted with CHCl_3 (2×50 ml), and the combined extracts dried over MgSO_4 , filtered and evaporated to give an orange oil. This was dissolved in EtOH (100 ml) prior to the addition of diethyl aminoacetaldehyde (25.4 ml, 23.3 g, 175 mmol). The solution was heated to reflux for 90 minutes. The solvent was removed under reduced pressure, and dilute HCl (10 %, 400 ml) was added. After reflux for 90 min, the reaction was collect to 0 °C. The resulting white solid was recovered by filtration and recrystallised from EtOH. It was then mixed with dilute HNO_3 (20 %, 120 ml) at room temperature. The reaction was warmed slowly to 100 °C. After the vigorous reaction had subsided, the vessel was cooled to room temperature. The solution was then neutralised with aq. NH_3 (15 %). The reaction was extracted with CHCl_3 (4×100 ml), and the combined extracts dried over MgSO_4 , filtered and evaporated to give a yellow solid (20.3 g, 52 %). ^1H NMR (500 MHz, CDCl_3) 1.13 (d, 12H, $J = 6.9$ Hz, Me), 2.40 (sept., 2H, $J = 6.7$ Hz, CH), 7.25–7.30 (m, 3H, phenyl CH and

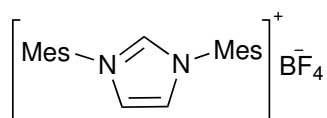
imidazolium CH), 6.94 (br s, 1H, imidazolium CH), 7.43 (t, 1H, $J = 7.8$ Hz, phenyl CH), 7.48 (br s, 1H, imidazolium CH).

7.2.2 Pyridine-2,6-diylbis-[3-(2,6-diisopropylphenyl)-3*H*-imidazol-1-ium] dibromide **43**



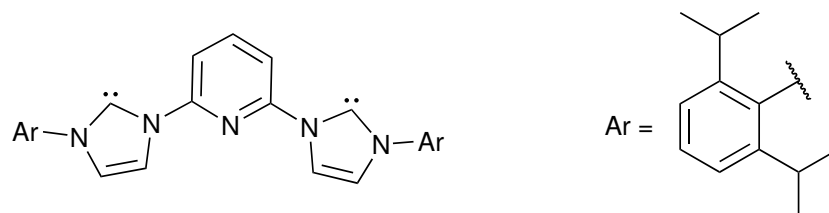
The method of Danopolous was followed.⁸⁹ 2,6-Dibromopyridine (3.76 g, 15.7 mmol) and **38** (7.19 g, 31.4 mmol) were mixed in a glass ampoule. This was sealed under vacuum and heated to 170 °C for 6 days. After cooling to room temperature, the brown solid was dissolved in excess CH₂Cl₂. The solvent was removed at reduced pressure, and the solid stirred overnight with Et₂O. Following filtration, the solid was dried azeotropically with toluene and the solid dried in vacuo. The product was obtained as a cream solid (8.95 g, 82%). ¹H NMR (500 MHz, CDCl₃) 1.10 (d, 12H, $J = 6.7$ Hz, Me), 1.22 (d, 12H, $J = 6.7$ Hz, Me), 2.35 (sept., 4H, $J = 6.7$ Hz, CH), 7.10 (dd, 2H, $J = 7.2, 13.0$ Hz, aromatic CH), 7.16–7.26 (m, 2H, aromatic CH), 7.47 (t, 2H, $J = 7.8$ Hz, aromatic CH), 8.17 (q, 1H, $J = 7.8$ Hz, aromatic CH), 9.13 (d, 2H, $J = 7.8$ Hz, aromatic CH), 10.00 (s, 2H, imidazolium CH), 12.18 (s, 2H, imidazolium CH).

7.2.3 1,3-Bis(2,4,6-trimethylphenyl)-1*H*-imidazolium bromide **48**



The synthetic method of Nolan was followed.¹⁰¹ 2,4,6-Timethylaniline (745.0 ml, 43.3 g, 321 mmol) was dissolved in MeOH (20 ml). Glyoxal (40 % in water, 20 ml, 160 mmol) and a few drops of formic acid were added, and the reaction stirred for 16 h. The resulting yellow solid was recovered by filtration. This was dissolved in EtOAc (48 ml), and warmed to 50 °C. Paraformaldehyde (6.2 g, 21.2 mmol) was dissolved in HCl (4 M in dioxane, 10 ml) and added drop-wise to the reaction solution. After addition was complete, the reaction was left to stir for 16 h. The resulting off-white solid was recovered by filtration (12.2 g, 87 %). For the intermediate **47**: ¹H NMR (500 MHz, CDCl₃) 2.18 (s, 12H, Me), 2.34 (s, 6H, Me), 7.03 (s, 4H, aromatic CH), 7.61 (s, 2H, imidazolium CH), 10.64 (s, 1H, imidazolium CH). The chloride salt was dissolved in water (500 ml), before addition of HBF₄ (40 % in water, 10 ml). The milky solution was extracted with CH₂Cl₂ (4 × 25 ml). The combined extracts were dried over MgSO₄, filtered and the solvent evaporated. The crude solid was taken up in CH₂Cl₂ (40 ml) and precipitated with Et₂O (200 ml) to give a cream solid (21.0 g, 84 %). ¹H NMR (500 MHz, CDCl₃) 2.13 (s, 12H, Me), 2.35 (s, 6H, Me), 7.04 (s, 4H, aromatic CH), 7.56 (s, 2H, imidazolium CH), 8.99 (s, 1H, imidazolium CH).

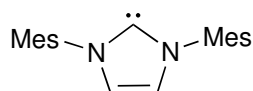
7.2.4 2,6-Bis-[3-(2,6-diisopropylphenyl)imidazol-2-ylidene]-pyridine **34**



The method of Danopolous was followed.⁸⁹ The imidazolium salt **43** (890 mg, 1.28 mmol) was suspended in THF (20 ml) and cooled to -78 °C. A solution of KHMDS (692 mg, 2.83 mmol) in (15 ml) was cooled to -78 °C and added to the salt suspension. The reaction was left to stir and warm slowly to room temperature over 16 h. After evaporation of the solvent at reduced pressure, the residue was dissolved

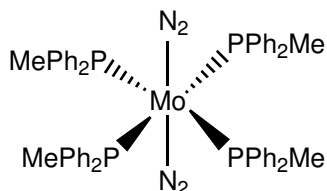
in toluene (20 ml) and filtered through Celite. The solvent evaporated, giving the product as a cream solid (799 mg, 64 mmol). ^1H NMR (500 MHz, C_6D_6) 1.14 (d, 12H, $J = 6.9$ Hz, Me), 1.23 (d, 12H, $J = 6.9$ Hz, Me), 2.95 (sept., 4H, $J = 6.9$ Hz, CH), 6.65 (d, H, $J = 1.7$ Hz, imidazole CH), 7.10 (t, 1H, $J = 7.9$ Hz, aromatic CH), 7.18 (d, 4H, $J = 7.9$ Hz, aromatic CH), 7.30 (q, 2H, $J = 7.9$ Hz, aromatic CH), 8.05 (d, H, $J = 7.9$ Hz, imidazole CH), 8.41 (d, H, $J = 1.7$ Hz, aromatic CH).

7.2.5 1,3-Bis(2,4,6-trimethylphenyl)imidazol-2-ylidene **49**



The method of Nolan was followed.¹⁰¹ The salt **48** (750 mg, 1.91 mmol) was suspended in THF (7.5 ml). Sodium hydride (60 mg, 2.3 mmol) and catalytic KO^tBu was added and the reaction was stirred for 16 h. The solution was filtered and the solution concentrated. Hexanes were added, resulting in a white precipitate which was recovered by filtration. The crude product was taken up in THF (10 ml) and reprecipitated with hexane (90 ml), giving the product as a cream solid (400 mg, 69%). ^1H NMR (500 MHz, d_8 -THF) 2.13 (s, 12H, Me), 2.34 (s, 6H, Me), 7.06 (s, 4H, aromatic CH), 7.65 (s, 2H, imidazolyl CH).

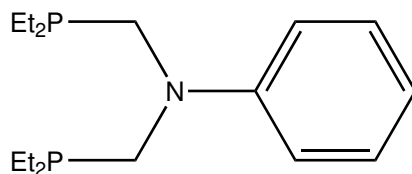
7.2.6 Bis(dinitrogen)tetrakis(methyldiphenylphosphino)-molybdenum(0) **53**



This reaction was carried out under nitrogen pressure supported by a mercury bubbler: use of a silicon oil bubbler was unsuccessful. A solution of PPh_2Me (0.83 ml, 0.88 g, 4.4 mmol) and MoCl_5 (0.30 g, 1.1 mmol) in THF (100 ml) was cooled to 0°C

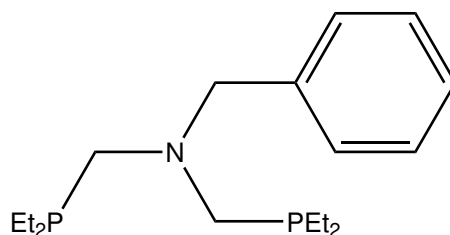
and added to I₂-activated magnesium (1.5 g) under nitrogen. The reaction mixture was stirred for 16 hours and allowed to warm slowly to room temperature. Filtration to remove excess magnesium was followed by removal of the solvent. The residue was taken up in toluene (100 ml), filtered through Celite and the volume reduced to around one-third, yielding an orange precipitate. Washing with MeOH gave a bright orange solid (0.66 g, 63 %). $\tilde{\nu}_{\max}$ (THF) 1929 cm⁻¹ (N≡N). ³¹P NMR (202 MHz, C₆D₆) 19.41 (PPh₂Me).

7.2.7 PN^{Ph}P Ligand 56a



A mixture of HPEt₂ (0.50 g, 5.6 mmol) and paraformaldehyde (0.17 g, 5.6 mmol) in EtOH (10 ml) was heated to 70 °C under nitrogen for four hours. Neat H₂NPh (0.25 ml, 0.26 g, 2.8 mmol) was added and the reaction heated to 70 °C for 6 days. After cooling to room temperature, the volatiles were removed at reduced pressure and the residue taken up in Et₂O. The solution was dried over MgSO₄ and filtered before removal of the solvent at reduced pressure. The product was obtained as a cream oil (0.69 g), which was used without further purification. ³¹P NMR (202 MHz, C₆D₆) -29.8 (78 %, product).

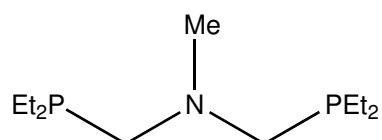
7.2.8 PN^{Bn}P Ligand 56b



Reaction was carried out by the same method as for PN^{Ph}P (Section 7.2.7). Reaction

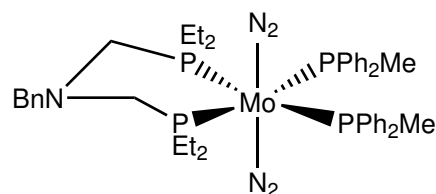
for 6 days on a 5.6 mmol scale yielded the target compound as a colourless oil (0.64 g), which was used without further purification. ^{31}P NMR (202 MHz, C_6D_6) -34.5 (85 % product), -25.5 (15 %).

7.2.9 $\text{PN}^{\text{Me}}\text{P}$ Ligand **56c**



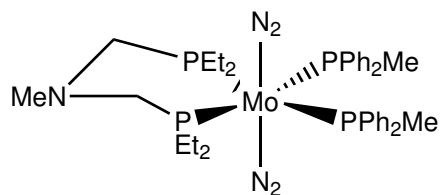
Reaction was carried out by the same method as for $\text{PN}^{\text{Ph}}\text{P}$ (Section 7.2.7). Reaction for 6 days on a 5.6 mmol scale yielded the target compound as a colourless oil (0.27 g), which was used without further purification. ^{31}P NMR (202 MHz, C_6D_6) -33.5 (76 % product), -26.6 (24 %).

7.2.10 Complex **57b**



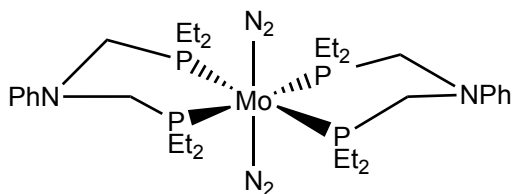
Ligand **56b** (47 mg, 0.15 mmol) was dissolved in THF (5 ml) and added to a solution of complex **53** (120 mg, 0.13 mmol) in THF (15 ml). After stirring for 16 h, the solvent was removed at reduced pressure to yield a dark red/brown oil. This was taken up in PhMe/THF (2 : 1, 10 ml) and filtered through alumina. Removal of the solvent yielded a brown solid. $\tilde{\nu}_{\text{max}}$ (THF) 1937 cm^{-1} ($\text{N}\equiv\text{N}$). ^{31}P NMR (202 MHz, d_8 -THF) 7.25 (d, $^2J_{\text{P-P}} = 78.9\text{ Hz}$), 15.40 (d, $^2J_{\text{P-P}} = 78.9\text{ Hz}$).

7.2.11 Complex 57c



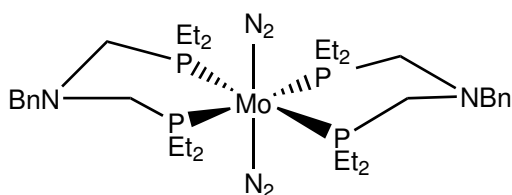
Reaction was carried out by the same method as for $\text{PN}^{\text{Ph}}\text{P}$ (Section 7.2.10), yielding an orange solid. $\tilde{\nu}_{\text{max}}$ (THF) 1937 cm^{-1} ($\text{N}\equiv\text{N}$). ^{31}P NMR (202 MHz, d_8 -THF) 9.75 (d, $^2J_{\text{P}-\text{P}} = 78.5\text{ Hz}$), 17.86 (d, $^2J_{\text{P}-\text{P}} = 78.5\text{ Hz}$).

7.2.12 Complex 58a



Reaction was carried out by the same method as for $\text{PN}^{\text{Ph}}\text{P}$ (Section 7.2.10), using twice the amount of chelating phosphine. $\tilde{\nu}_{\text{max}}$ (THF) 1942 cm^{-1} ($\text{N}\equiv\text{N}$). ^{31}P NMR (202 MHz, d_8 -THF) 13.88.

7.2.13 Complex 58b



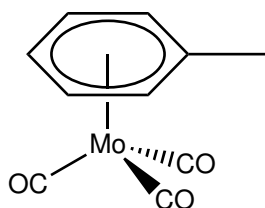
Reaction was carried out by the same method as for $\text{PN}^{\text{Ph}}\text{P}$ (Section 7.2.10), using twice the amount of chelating phosphine. $\tilde{\nu}_{\text{max}}$ (THF) 1941 cm^{-1} ($\text{N}\equiv\text{N}$). ^{31}P NMR (202 MHz, d_8 -THF) 8.8.

7.3 Molybdenum carbonyl precursors

7.3.1 Tri(acetonitrile)tricarbonylmolybdenum(0) 63

Freshly distilled acetonitrile was degassed and added to molybdenum hexacarbonyl (4.48 g, 16.95 mmol). The solution was refluxed for 16 hours. An olive solution with some dark brown solid was formed. The suspension was filtered to give greenish-yellow solution. Evaporation afforded a light yellow solid. This was washed with ether and dried under vacuum to afford pale yellow solid (6.35 g). $\tilde{\nu}_{\max}$ (MeCN) 1911, 1841 cm^{-1} ; (CH_2Cl_2) 1980, 1946, 1904 cm^{-1} .

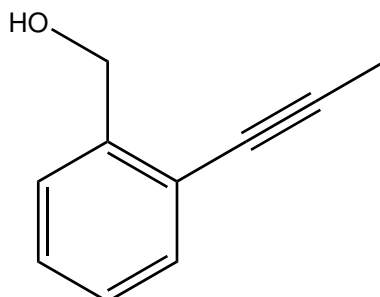
7.3.2 η^3 -Toluenetricarbonylmolybdenum(0) 64



Molybdenum hexacarbonyl (4.2 g, 15.9 mmol) was dissolved in toluene (300 ml) and refluxed at 130 °C for 87 hours. The dark olive solution with some black solid was cooled to room temperature and filtered to afford a yellow solution. Removal of the solvent gave a yellow solid (3.85 g, 14.2 mmol, 89 %). $\tilde{\nu}_{\max}$ (PhMe) 1970, 1890 cm^{-1} ; (CH_2Cl_2) 1968, 1885 cm^{-1} .

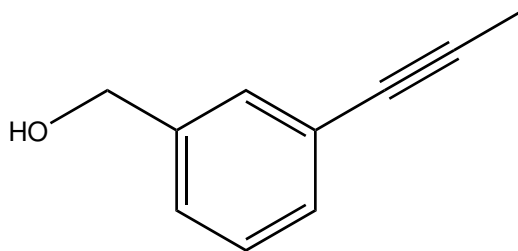
7.4 Functionalised dithiolene ligands

7.4.1 2-(Propyn-1-yl)benzyl alcohol *o*-67



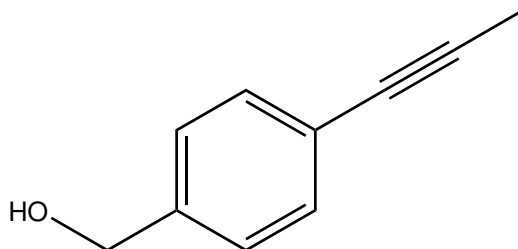
An ethyne generator was prepared by dissolving KOH (28.6 g) in butanol (120 ml) in a flask fitted with a reflux condenser and dropping funnel filled with 1,2-dibromopropane (25 ml, 50 g, 250 mmol). Iodobenzyl alcohol (5.85 g, 25 mmol), Pd(PPh₃)₄ (0.433 g, 0.375 mmol) and CuI (0.143 g, 0.75 mmol) were dissolved in THF (80 ml) and piperidine (75 ml). A gas transfer tube was fitted from the top of the reflux condenser of the generator flask to a dip tube in the reaction flask. The generator reaction was heated to reflux and slow addition of the bromoalkane commenced. The reaction was purged with ethyne until all of the bromoalkane was consumed, then the dip tube was sealed and the reaction mixture left to stir for 16 hours. The reaction solution was poured into HCl (6 M, 200 ml) whilst cooling to 0 °C. The layers were separated, and the aqueous layer extracted with EtOAc (200 ml then 2 × 100 ml). The combined organic extracts were washed with aq. NaHCO₃ and brine, then dried over MgSO₄. After removal of the solvent, the resulting solid was purified by sublimation at reduced pressure. The product was obtained as a white solid (3.50 g, 96%). ¹H NMR (500 MHz, CDCl₃) 2.10 (s, 3H, Me), 2.13 (t, 1H, *J* = 6.4 Hz, OH), 4.79 (d, 2H, *J* = 6.4 Hz, CH₂), 7.22 (td, 1H, *J* = 1.4, 7.5 Hz, aryl CH), 7.29 (td, 1H, *J* = 1.4, 7.5 Hz, aryl CH), 7.40 (m, 2H, 2 × aromatic CH). ¹³C NMR (126 MHz, CDCl₃) 4.63 (Me), 64.39 (CH₂), 90.90 (alkyne), 122.37 (aromatic CH), 127.47 (aromatic CH), 127.57 (aromatic CH), 128.12 (aromatic CH), 132.41 (aromatic C), 142.53 (aromatic C).

7.4.2 3-(Propyn-1-yl)benzyl alcohol *m*-67



The reaction was carried out following the method reported by Pfer.¹²³ A mixture of PdCl₂(PPh₃)₂ (300 mg, 0.43 mmol), butyric acid (2.15 g, 25.6 mmol), (3-iodophenyl)methanol (*m*-65) (2.72 ml, 5.00 g, 21.4 mmol) and dppb (182 mg, 0.427 mmol) was degassed for ten minutes. DMSO (60 ml) and DBU (18.2 ml, 18.6 g, 122 mmol) were added and the reaction heated to 110 °C for 12 h. The resulting brown solution was quenched with saturated aq. NaHCO₃ with cooling and extracted with EtOAc. The organic solution was washed with water and brine, dried over MgSO₄ and filtered. The solution was stirred with activated carbon, filtered and the solvent removed at reduced pressure. This gave the product as a brown oil (1.25 g, 42%). ¹H NMR (500 MHz, CDCl₃) 1.91 (s, 3H, Me), 4.52 (s, 2H, CH₂), 7.10–7.18 (m, 3H, aromatic CH), 7.18 (td, 1H, *J* = 1.6, 4.8 Hz, aromatic CH). ¹³C NMR (126 MHz, CDCl₃) 4.79 (Me), 64.96 (CH₂), 79.61 (alkyne), 85.99 (alkyne), 124.24 (aromatic C), 126.10 (aromatic CH), 128.45 (aromatic CH), 129.96 (aromatic CH), 130.68 (aromatic CH), 140.89 (aromatic C).

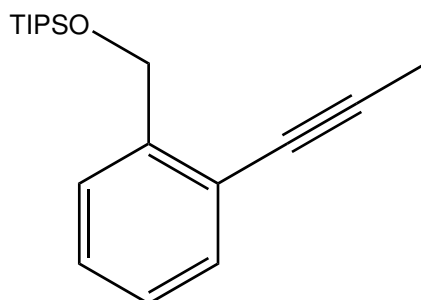
7.4.3 4-(Propyn-1-yl)benzyl alcohol *p*-67



The reaction was carried out following the method reported by Pfer.¹²³ A mixture of PdCl₂(PPh₃)₂ (560 mg, 0.80 mmol), butyric acid (4.12 g, 49.0 mmol), (4-

bromophenyl)methanol (**79**) (7.60 g, 40.6 mmol) and dppb (340 mg, 0.797 mmol) was degassed for ten minutes. DMSO (60 ml) and DBU (18.2 ml, 18.6 g, 122 mmol) were added and the reaction heated to 110 °C for 12 h. The resulting brown solution was quenched with saturated aq. NH₄Cl with cooling and extracted with EtOAc. The organic solution was washed with water and brine, dried over MgSO₄, filtered and the solvent removed at reduced pressure. The crude material was purified by column chromatography on silica, eluting with hexane–EtOAc 3 : 1. This gave the product as a yellow solid (4.13 g, 28.2 %). ¹H NMR (500 MHz, CDCl₃) 2.05 (s, 3H, Me), 4.68 (s, 2H, CH₂), 7.25–7.32 (m, 2H, aromatic CH), 7.38 (d, 2H, *J* = 8.2 Hz, aromatic CH). ¹³C NMR (126 MHz, CDCl₃) 4.33 (Me), 65.04 (CH₂), 79.49 (alkyne), 85.91 (alkyne), 123.32 (aromatic C), 126.77 (aromatic CH), 131.66 (aromatic CH), 140.16 (aromatic C).

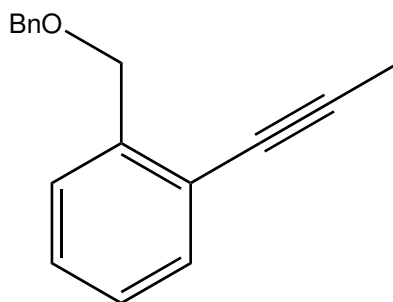
7.4.4 TIPS-protected *o*-alkyne **o-73a**



This compound was previously reported by Shioiri and co-workers, but via a different route and with no spectroscopic data available.¹⁴⁷ Imidazole (145 mg, 2.13 mmol) and TIPS-Cl (0.29 ml, 1.34 mmol) were dissolved in DMF (7 ml). 2-(Propyn-1-yl)benzyl alcohol **o-67** (100 mg, 0.68 mmol) was added and stirred for 16 hours. Progress was monitored with thin layer chromatography with 3 : 1 hexane–ethyl acetate as mobile phase (*R_f* = 0.73). The solution was poured into water (100 ml) and extracted with diethyl ether (3 × 25 ml), washed with LiCl (5 % w/v), dried over MgSO₄, filtered and the solvent removed to afford light yellow oil (155 mg, 75 %). ¹H NMR (500 MHz, CDCl₃) 1.11 (d, 18H, *J* = 7.1 Hz, CH(CH₃)₂), 1.15–1.25 (m, 3H, CH(CH₃)₂), 2.08 (s,

3H, Me), 7.16 (td, 1H, $J = 1.3, 7.5$ Hz, 1H, aryl CH), 7.26–7.37 (m, 2H, aryl CH), 7.60 (dd, 1H, $J = 1.3, 7.7$ Hz, aryl CH). ^{13}C NMR (126 MHz, CDCl_3) 12.22 ($\text{CH}(\text{CH}_3)_2$), 18.21 (Me), 63.65 (CH_2), 90.80 (alkyne), 120.70 (aromatic CH), 125.60 (aromatic CH), 126.35 (aromatic CH), 127.87 (aromatic CH), 131.60 (aromatic C), 143.40 (aromatic C). HRMS m/z (TOF) found 303.2143, $\text{C}_{19}\text{H}_{30}\text{OSi}$ requires 303.2144.

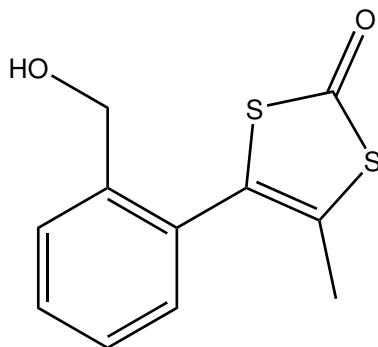
7.4.5 Benzyl-protected *o*-alkyne ***o*-73c**



NaH (free of oil, 480 mg, 20 mmol) was suspended in THF (45 ml) cooled to 0°C . 2-(Propyn-1-yl)benzyl alcohol ***o*-67** (3.0 g, 20.5 mmol) was dissolved in THF (40 ml) and added drop-wise to the sodium hydride suspension. This resulted in a cream suspension, which was warmed up to room temperature. BnBr (5.6 ml, 45 mmol) was added drop-wise over 10 minutes. The cream-yellow suspension was stirred for 16 hours, resulting in a cream solution with white solid at the bottom. This suspension was poured on HCl (1 M, 100 ml), extracted with EtOAc (3×50 ml), washed with HCl , NaHCO_3 and brine. The product was then dried with MgSO_4 , filtered and the solvent removed to afford yellow oil. This was purified by flash chromatography on silica gel in hexane– EtOAc (9 : 1), yielding the product as a white solid (4.16 g, 89%). ^1H NMR (500 MHz, CDCl_3) 1.97 (s, 3H, Me), 4.60 (s, 2H, CH_2), 4.65 (s, 2H, CH_2), 7.13–7.36 (m, 9H, aryl CH). ^{13}C NMR (101 MHz, CDCl_3) 33.70 (Me), 70.51 (CH_2), 72.64 (CH_2), 90.49 (alkyne), 122.85 (aromatic CH), 127.32 (aromatic CH), 127.70 (aromatic CH), 127.88 (aromatic CH), 128.50 (aromatic CH), 128.56 (aromatic CH), 128.94 (aromatic CH), 129.17 (aromatic CH), 132.17 (aromatic CH), 137.93 (aromatic C), 138.61 (aromatic C), 140.03 (aromatic C). HRMS m/z (TOF)

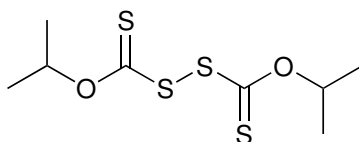
found 237.1278, C₁₇H₁₆OH requires 237.1279.

7.4.6 Unprotected *o*-dithiolene *o*-69



Disulphide **68** (4.06 g, 15 mmol) and 2-(propyn-1-yl)benzyl alcohol *o*-**67** (2.0 g, 13.7 mmol) were dissolved in xylenes (20 ml), and the suspension degassed. The suspension was heated at 40 °C to dissolve the substrate. ACNH (1.47 g, 6 mmol) was added, and the solution was heated to 140 °C for 18 hours. The residue was cooled and purified by column chromatography (hexane–EtOAc 3 : 1), yielding the title compound (1.02 g) along with recovered alkyne (0.45 g). The presence of sulphur-based impurities meant this compound was used without further purification. ¹H NMR (500 MHz, CDCl₃) 1.70 (t, 1H, *J* = 5.4 Hz, OH), 2.02 (s, 3H, Me), 4.70 (d, 2H, *J* = 5.4 Hz, CH₂), 7.29 (dd, 1H, *J* = 1.5, 7.7 Hz, aryl CH), 7.36 (td, 1H, *J* = 1.4, 7.5 Hz, aryl CH), 7.46 (td, 1H, *J* = 1.5, 7.6 Hz, aryl CH), 7.59 (ddd, 1H, *J* = 0.7, 1.4, 7.8 Hz, aryl CH).

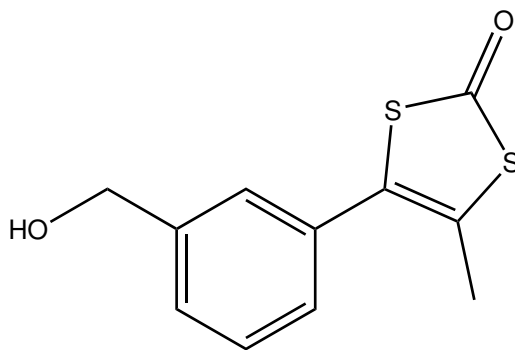
7.4.7 Diisopropyl xanthogen disulphide **68**



The synthesis was carried out following the method of Jamir.¹⁴⁸ KOH (9.33 g, 166 mmol) was dissolved in *isopropanol* (200 ml) by warming to 50 °C. Once fully

dissolved, the solution was cooled to 0 °C under argon. Carbon disulphide (10.0 ml, 12.7 g, 166 mmol) was added drop-wise leading to a cream precipitate. Additional *isopropanol* (150 ml) was added, reaction allowed to warm to room temperature and stirred for three hours. The intermediate salt Me₂CHOC(=S)SK was obtained after filtration and washing with *isopropanol* (3×50 ml) and hexane (100×50 ml). ¹H NMR (500 MHz, DMSO-*d*₆) 1.16 (d, 6H, *J* = 6.3 Hz, Me), 5.45 (sept., 1H, *J* = 6.3 Hz, CH). KOH (320 mg, 5.7 mmol) and I₂ (6.34 g, 25.0 mmol) were dissolved in water (100 ml) and cooled to 0 °C. A portion of the intermediate salt (10.0 g, 57.0 mmol) in water (80 ml) was added drop-wise. The reaction was allowed to stir for 16 h, resulting in a yellow solution and a yellow oily solid. The solution was decanted and the residue washed with water (500 ml), then with a small amount of MeCN (10 ml). The resulting pale yellow solid (3.86 g, 50 %) was used without further purification. ¹H NMR (500 MHz, MeCN-*d*₃) 1.42 (d, 12H, *J* = 6.2 Hz, Me), 5.72 (sept., 2H, *J* = 6.2 Hz, CH).

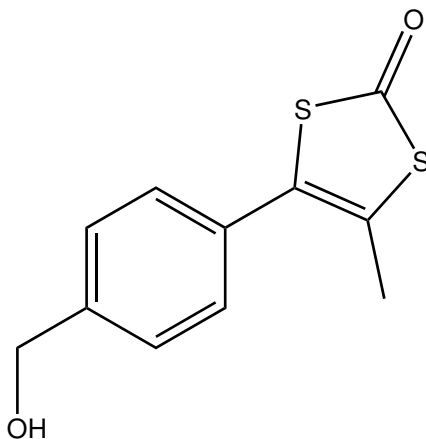
7.4.8 Unprotected *m*-dithiolene *m*-69



The reaction was carried out as described for *o*-**69**, using disulphide **68** (2.4 g, 9.0 mmol), *m*-**67** (2.3 g, 9.0 mmol) and ACNH (1.0 g, 4.4 mmol). Yield 624 mg, 34 %. ¹H NMR (400 MHz, CDCl₃) 2.05 (s, 3H, Me), 4.65 (s, 2H, CH₂), 7.26–7.29 (m, 2H, aryl CH), 7.31 (dt, 1H *J* = 1.6, 5.9 Hz, aryl CH), 7.39 (d, 1H, *J* = 1.7 Hz, aryl CH). ¹³C NMR (101 MHz, CDCl₃) 15.33 (Me), 64.91 (CH₂), 125.12 (alkene), 127.46 (aromatic CH), 127.86 (aromatic CH), 128.71 (aromatic CH), 129.21 (aromatic CH),

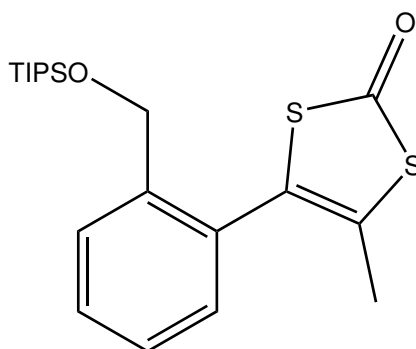
131.78 (aromatic C), 141.83 (aromatic C), 191.60 (CO).

7.4.9 Unprotected *p*-dithiolene *p*-69



The reaction was carried out as described for *o*-69, using disulphide **68** (6.20 g, 23 mmol), *p*-67 (3.35 g, 23 mmol) and ACNH (2.8 g, 11 mmol). ¹H NMR (400 MHz, CDCl₃) 2.23 (s, 3H, Me), 4.74 (s, 2H, CH₂), 7.36 (d, 2H, *J* = 8.2 Hz, aryl CH), 7.43 (d, 2H, *J* = 8.2 Hz, aryl CH).

7.4.10 TIPS-protected *o*-dithiolone *o*-70a



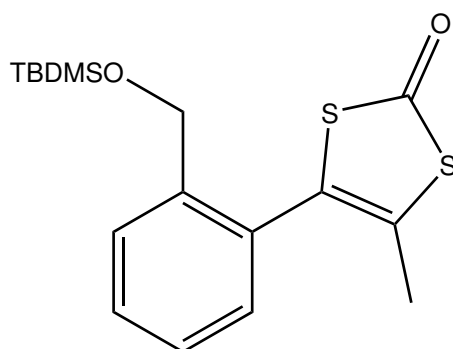
Two approaches were used for the synthesis of this molecule: from *o*-69 and from *o*-73a.

The ligand *o*-69 (121 mg, 0.51 mmol) was dissolved in DMF (12 ml). Imidazole (104 mg, 1.52 mmol) and TIPS-Cl (293 mg, 1.52 mmol) were added, and the reaction mixture stirred for 16 hours. The solution was poured into water (100 ml) and

extracted with hexane (3×50 ml). The combined extracts were washed with sat. LiCl solution then dried over MgSO_4 . After treatment with activated charcoal, evaporation of the solvent gave the product as teal oil (87 mg). ^1H NMR (400 MHz, CDCl_3) 1.03–1.12 (m, 27H, TIPS), 2.00 (s, 3H, Me), 7.24 (dd, 1H, $J = 1.5, 7.6$ Hz, aryl CH), 7.31 (td, 1H, $J = 1.5, 7.4$ Hz, aryl CH), 7.45 (td, 1H, $J = 1.5, 7.6$ Hz, aryl CH), 7.69 (dd, 1H, $J = 1.5, 7.6$ Hz, aryl CH).

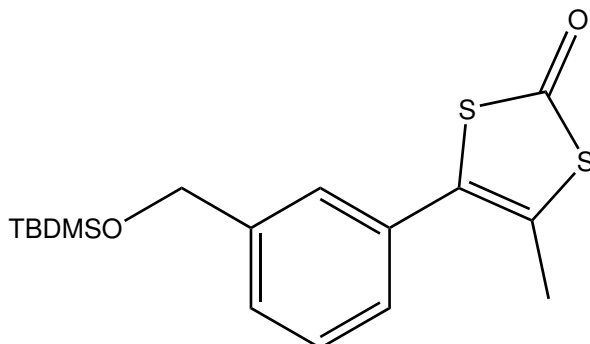
Reaction starting from *o*-**73a** was carried out as described for the synthesis of *o*-**69**, using disulphide **68** (379 mg, 1.4 mmol), *o*-**73a** (175 mg, 0.58 mmol) and ACNH (122 mg, 0.5 mmol). A small amount of clear oil was obtained, but was not purified further.

7.4.11 TBDMS-protected *o*-dithiolone *o*-**70b**



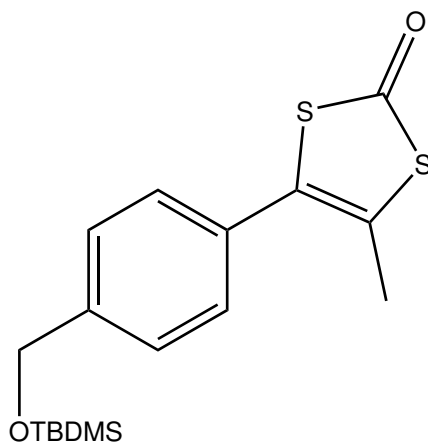
The dithione *o*-**69** (0.370 g, 1.55 mmol) and imidazole (0.211 g, 3.1 mmol) were dissolved in DMF (10 ml). TBDMS-Cl (0.47 g, 3.1 mmol) was added, and the solution stirred for 16 hours. It was poured into water and extracted with hexane (3×50 ml). The combined extracts were washed with aq. LiCl (5%, 100 ml) and the solution dried over MgSO_4 and decoloured using charcoal. The solvent was removed at reduced pressure yielding the product as a light yellow oil (0.284 g, 52%). ^1H NMR (400 MHz, CDCl_3) 0.09 (s, 6H, Me), 0.93 (s, 9H, ^tBu), 2.00 (s, 3H, Me), 4.67 (s, 2H, CH_2), 7.22–7.26 (m, 1H, aryl CH), 7.29–7.33 (m, 1H, aryl CH), 7.44 (td, 1H, $J = 1.5, 7.6$ Hz, aryl CH), 7.60 (ddd, 1H, $J = 0.7, 1.4, 7.8$ Hz, aryl CH).

7.4.12 TBDMS-protected *m*-dithiolone *m*-70b



The reaction was carried out as described for *o*-70b. Found C 58.23, H 6.91%; $C_{17}H_{24}O_2S_2Si$ requires C 57.91, H 6.86% 1H NMR (400 MHz, $CDCl_3$) 0.12 (s, 6H, Me), 0.95 (s, 9H, *t*-Bu), 2.23 (s, 3H, Me), 4.76 (s, 2H, CH_2), 7.22–7.25 (m, 1H, aryl CH), 7.30 (m, 1H, aryl CH), 7.35 (m, 1H, aryl CH), 7.38 (td, 1H, $J = 0.7, 7.5$ Hz). ^{13}C NMR (101 MHz, $CDCl_3$) –4.84 (silyl Me), 14.70 (Me), 26.35 (Me), 63.25 (CH_2), 89.41 (alkene), 126.23 (aromatic CH), 127.29 (aromatic CH), 129.47 (aromatic CH), 132.32 (aromatic CH).

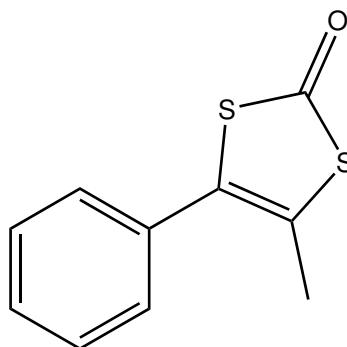
7.4.13 TBDMS-protected *p*-dithiolone *p*-70b



The reaction was carried out as described for *o*-70b. 1H NMR (400 MHz, $CDCl_3$) 0.12 (s, 6H, Me), 0.96 (s, 9H, *t*Bu), 2.22 (s, 3H, Me), 4.76 (s, 2H, CH_2), 7.30–7.34 (m, 2H, aryl CH), 7.37 (d, 2H, $J = 8.5$ Hz, aryl CH). ^{13}C NMR (101 MHz, $CDCl_3$) –5.28

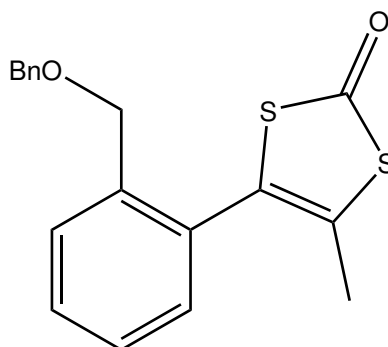
(silyl Me), 4.33 (CMe_3), 18.39 (Me), 25.92 (Me), 64.69 (CH_2), 85.29 (alkene), 122.43 (aromatic C), 125.84 (aromatic CH), 131.34 (aromatic CH), 140.88 (aromatic C).

7.4.14 Unfunctionalised dithiolone **72**



Reaction was carried out as for *o*-**70b**, with purification using hexane–EtOAc 9 : 1. 1H NMR (500 MHz, $CDCl_3$) 2.15 (s, 3H, Me), 7.28–2.27 (m, 5H, Ph). HRMS m/z (TOF) found 209.0098, $C_{10}H_8OS_2H$ requires 209.0095.

7.4.15 Benzyl-protected *o*-dithiolone *o*-**70c**

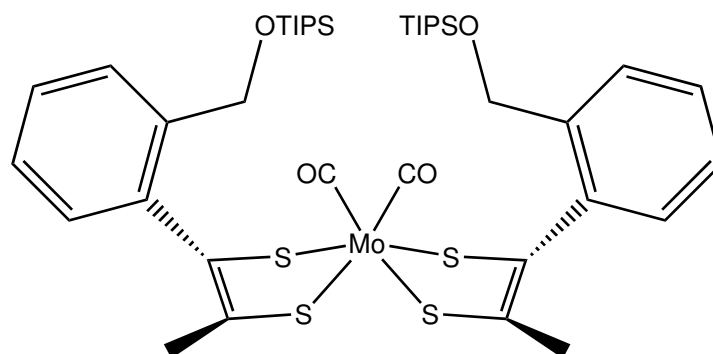


Reaction was carried out as for the synthesis of *o*-**70b**. Chromatography in hexane–EtOAc 20 : 1 yielded the product. The product was purified by chromatography in hexane–EtOAc 20 : 1, yielding a yellow oil (0.801 g, 14%). Found C 65.68, H 4.88 %; $C_{18}H_{16}O_2S_2$ requires C 65.82, H 4.91 %. 1H NMR (500 MHz, $CDCl_3$) 1.87 (s, 3H, Me), 4.42 (s, 2H, CH_2), 4.47 (s, 2H, CH_2), 7.16–7.29 (m, 7H, aryl CH), 7.35 (td, 1H, $J = 1.5, 7.5$ Hz, aryl CH), 7.46–7.53 (m, 1H, aryl CH). ^{13}C NMR (126 MHz,

CDCl₃) 15.17 (Me), 69.76 (CH₂), 73.12 (CH₂), 125.89, 126.50, 127.99, 128.02, 128.31, 128.62, 129.58, 129.85, 130.13, 130.92, 137.92, 138.16, 191.99 (CO). HRMS *m/z* (TOF) found 329.0667, C₁₈H₁₆O₂S₂H requires 329.0670.

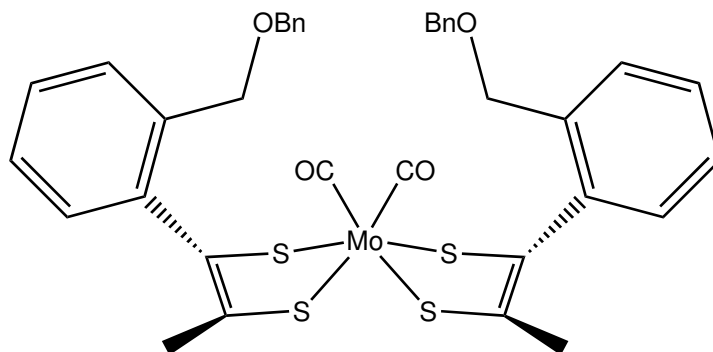
7.5 Direct formation of metal ditholene complexes

7.5.1 TIPS-protected molybdenum complex *o*-74a



n-BuLi (1.6 M in hexanes, 0.33 ml, 0.56 mmol) was added to *o*-70a (85 mg, 0.22 mmol) in PhMe (10 ml) at 0 °C. The solution was stirred for 16 hours, during which time it became yellow. A solution of Mo(CO)₃(PhMe) (54 mg, 0.20 mmol) in PhMe (10 ml) was then cooled to -78 °C before addition of I₂ (25 mg, 0.10 mmol). After three hours, the ligand solution was added drop-wise to the metal solution. The reaction was stirred for 16 hours. The solvent was removed at reduced pressure and the crude material purified by chromatography (hexane-CH₂Cl₂ 4 : 1). Two fractions were obtained, the *title compound* first as a purple solid, followed by the tris(ligand) adduct as a green solid. For the title compound: $\tilde{\nu}_{\max}$ (PhMe) 2038, 1995 cm⁻¹. HRMS *m/z* (TOF) found 1196.3591, C₅₇H₉₀MoO₃S₆Si₃ requires 1196.3580.

7.5.2 Benzyl-protected molybdenum complex *o*-74c



Reaction was carried out by the same method as for the synthesis of complex *o*-74a. HRMS m/z (TOF) found 999.1047, $C_{51}H_{48}MoO_3S_6$ requires 999.1064.

7.5.3 Deprotection of *o*-74a using TASF

Complex *o*-74a (60 mg, 0.068 mmol) was dissolved in THF (3 ml) and cooled to 0 °C. TASF (100 mg, 0.27 mmol) was added. The solution immediately turned green then black. An infra-red spectrum of the crude reaction mixture showed no CO bands.

7.5.4 Deprotection of *o*-74a using $Et_3N \cdot 3HF$

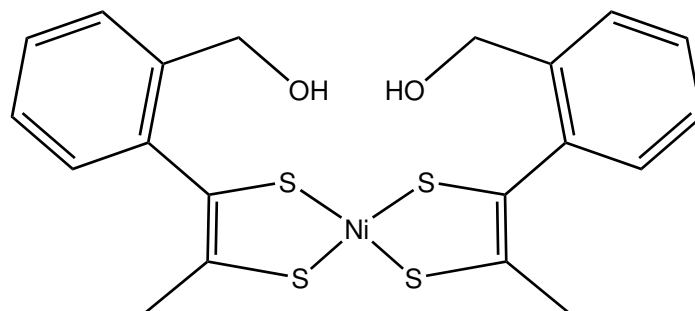
Complex *o*-74a (60 mg, 0.068 mmol) was dissolved in THF (3 ml) and cooled to 0 °C. $Et_3N \cdot HF$ (0.2 ml, 0.68 mmol) was added. The solution immediately turned brown then green. An infra-red spectrum of the crude reaction mixture showed no CO bands.

7.5.5 Deprotection of *o*-74a using TBAF

Complex *o*-74a (60 mg, 0.068 mmol) was dissolved in THF (3 ml) and cooled to 0 °C. TBAF (1 M in THF, 0.3 ml, 0.20 mmol) was added. The solution immediately turned black. An infra-red spectrum of the crude reaction mixture showed no CO bands.

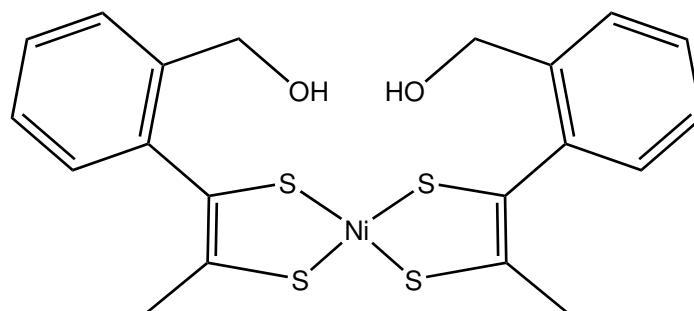
7.6 Formation of metal dithiolene complexes via nickel

7.6.1 *Ortho*-nickel complex *o*-77 using TIPS-protected pro-ligand



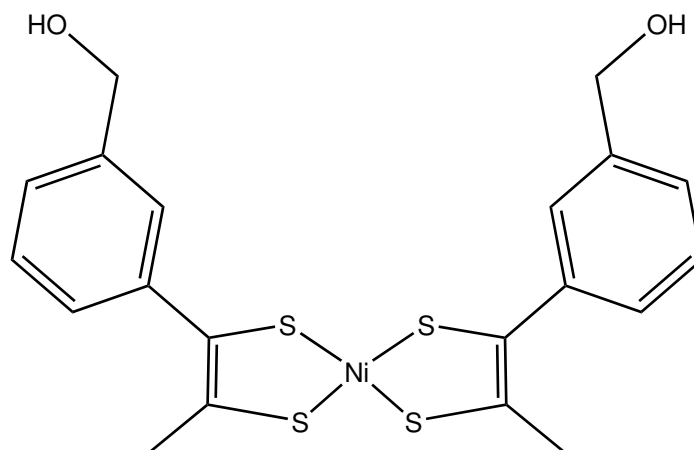
n-BuLi (1.6 M) in hexanes (3.8 ml, 6.1 mmol) was added to *o*-**70** (0.96 g, 2.4 mmol) in PhMe (30 ml) at 0 °C. The solution was stirred for 16 hours, during which time it became yellow. This was then added drop-wise to Ni(acac)₂ (312 mg, 1.22 mmol) in PhMe (50 ml). After two hours, I₂ (309 mg, 1.22 mmol) was added and the solution stirred for 16 hours. The solvent was removed at reduced pressure. The residue was taken up in THF (70 ml) prior to addition of aq. HCl (12 M HCl 0.5 ml/water 6 ml). The reaction was stirred for one hour, after which time the solution was diluted with EtOAc and washed with aq. NaHCO₃ and brine. After drying over MgSO₄, removal of the solvent gave a brown oil.

7.6.2 *Ortho*-nickel complex *o*-77 using TBDMS-protected proligand



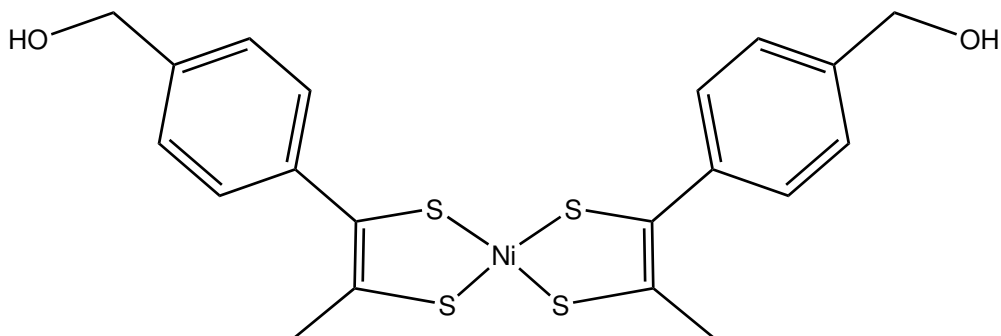
Reaction was carried out following the same method as starting from the TIPS-protected proligand. After removal of the protective group using HCl, the reaction solution was dark purple. This was then purified by chromatography on silica using hexane–EtOAc 1 : 1 as the mobile phase. The product was obtained as a dark green oily solid (61 mg, 31 %).

7.6.3 *Meta*-nickel complex *m*-77



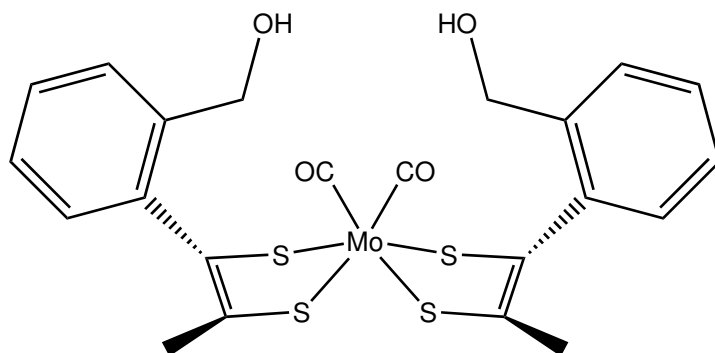
Reaction was carried out using the same method as for the TBDMS variant (Section 7.6.2). Yield (102 mg, 99%). m/z 478 ((M – H)⁺).

7.6.4 *Para*-nickel complex *p*-77



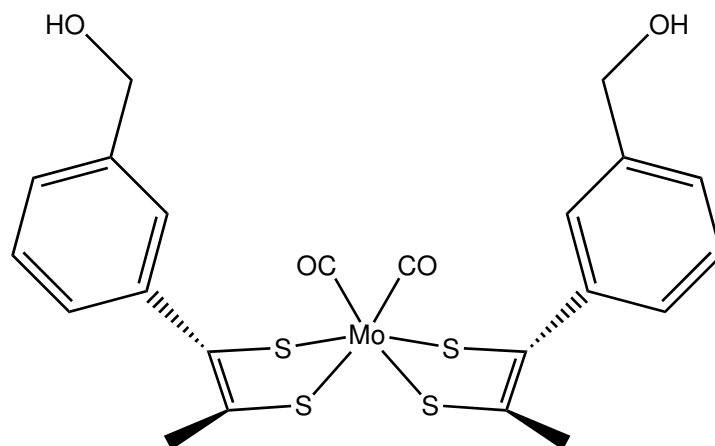
Reaction was carried out using the same method as for the TBDMS variant (Section 7.6.2). m/z 478 ((M - H)⁺).

7.6.5 *Ortho*-molybdenum complex *o*-78



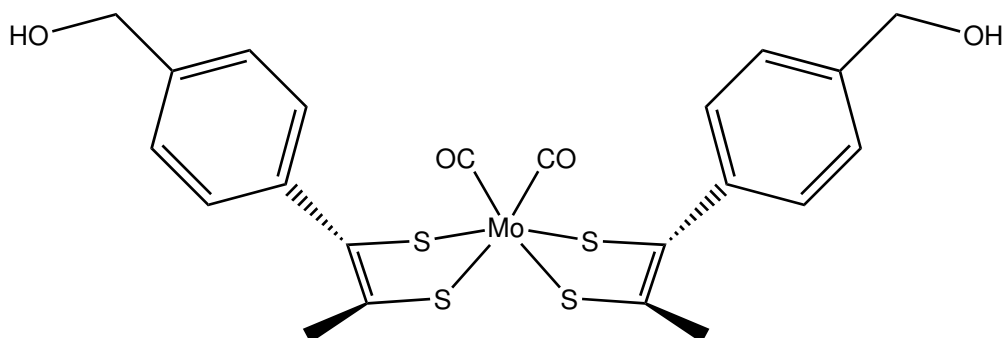
Complex *o*-76 (61 mg, 0.13 mmol) was dissolved in EtOAc (20 ml) and added rapidly to Mo(CO)₃(PhMe) (27 mg, 0.10 mmol) in EtOAc (20 ml). The reaction was stirred for 16 hours then the solvent was removed at reduced pressure. Purification on silica, using hexane–EtOAc 1 : 1 as the mobile phase, gave the title compound as a purple solid (164 mg) along with the tris-ligand adduct as a green solid (56 mg). $\tilde{\nu}_{\max}$ (EtOAc) 2035, 1983 cm⁻¹.

7.6.6 *Meta*-molybdenum complex *m*-78



Reaction was carried out using the same method as for the *ortho* variant (Section 7.6.5). $\tilde{\nu}_{\max}$ (CH₂Cl₂) 2039 cm⁻¹.

7.6.7 *Para*-molybdenum complex *p*-78



Reaction was carried out using the same method as for the *ortho* variant (Section 7.6.5). m/z 572 (M⁺). $\tilde{\nu}_{\max}$ (EtOAc) 2044, 1983 cm⁻¹. For the *tris*(ligand) product m/z 696 (M⁺ - CH₂OH).

7.7 X-Ray crystallography

For each sample, crystals were suspended in oil and one was mounted on a glass fibre and fixed in the cold nitrogen stream of the diffractometer. Data were collected using either Cu-K α ($\lambda = 1.54184 \text{ \AA}$) using a Rigaku FR-E++ equipped with copper

rotating anode equipped with confocal mirrors (2 (**56c**) · **57c**) and *p*-**77**), or Mo-K α ($\lambda = 0.71073 \text{ \AA}$) radiation using a Bruker D8 QUEST (*o*-**77**). Data were collected and processed using Bruker SAINT and Bruker APEX2 (2 (**56c**) · **57c** and *p*-**77**)^{149,150} or CrystalClear-SM Expert and CrysAlisPro (*o*-**77**).^{151,152}

Structures were determined dual space methods in SHELXT-2018¹⁵³ and refined by full-matrix least-squares methods on F^2 in SHELXL-2018.¹⁵⁴ Non-hydrogen atoms were refined with anisotropic thermal parameters. Hydrogen atoms bound to carbon were included in idealized positions and their U_{iso} values were set to ride on the U_{eq} values of the parent atom.

For structure 2 (**56c**) · **57c**, disorder in one phenyl group, one phosphine group and one methylene group was modelled by appropriate restraints between the component parts. Thermal parameters were constrained between the equivalent parts. In *o*-**77**, the OH group was disordered over two positions. Structure *p*-**77** was refined as a two-component merohedral twin, in which the major component had occupancy of 0.810(7) at the conclusion of refinement. A summary of key X-ray data parameters are given in Table 7.1.

7.8 DFT calculations

All calculations were performed using the ADF computational package.^{127–129} Geometry optimisation was carried out using the ADF triple- ζ basis set with the zero-order regular approximation (ZORA) to account for relativistic effects.¹⁵⁵ The generalized-gradient approximation (GGA) was employed in the geometry optimizations using the Beck and Perdew (BP86) exchange-correlation (XC) functional.^{134,135} Structures were geometry optimised in the gas phase with the default convergence criteria and confirmed as minima through frequency calculations. Final atomic co-ordinates are provided as an appendix.

Table 7.1: Summary of X-ray data for compounds 2 (**56c**) · **57c**, **57c**, **o-77** and **p-77**.

	2 (56c) · 57c	o-77	p-77
Formula	$2(\text{C}_{37}\text{H}_{53}\text{MoN}_5\text{P}_4)$, $\text{C}_{22}\text{H}_{54}\text{MoN}_6\text{P}_4$	$\text{C}_{20}\text{H}_{20}\text{NiO}_2\text{S}_4$	$\text{C}_{20}\text{H}_{18}\text{NiO}_2\text{S}_4$
Formula weight	2197.85	479.31	477.29
Crystal system	Triclinic	Triclinic	Monoclinic
Space group	$P\bar{1}$	$P\bar{1}$	$P2_1/n$
$a/\text{\AA}$	12.3554(4)	5.2415(2)	10.7580(11)
$b/\text{\AA}$	15.4060(7)	7.2493(3)	4.2295(7)
$c/\text{\AA}$	15.5785(6)	14.0207(6)	21.705(3)
$\alpha/^\circ$	104.217(4)	88.0490(10)	90
$\beta/^\circ$	108.209(3)	85.5570(10)	90.393(13)
$\gamma/^\circ$	91.469(3)	74.3650(10)	90
$V/\text{\AA}^3$	2713.63(19)	511.45(4)	987.6(2)
Z	1	1	2
T/K	100(2)	113(2)	100.01(10)
Crystal size/mm	$0.01 \times 0.04 \times 0.08$	$0.017 \times 0.074 \times 0.186$	$0.01 \times 0.01 \times 0.20$
$\lambda/\text{\AA}$	1.54184	0.71073	1.54184
$\theta/^\circ$	66.593	25.242	43.715
Reflections measured	39399	15825	5218
Unique reflections	9554	2089	745
Reflections with $I > 2\sigma I$	6928	1925	627
R_{int}	0.0697	2089	0.1995
No. parameters	599	134	127
$R_1 (I > 2\sigma I)$	0.0591	0.0221	0.1159
wR_2 (all data)	0.1758	0.0511	0.3073

References

- (1) R. Crabtree, *The Organometallic Chemistry of the Transition Metals*, Wiley, Hoboken, New Jersey, 2014.
- (2) R. H. Holm, P. Kennepohl and E. I. Solomon, *Chem. Rev.*, 1996, **96**, 2239–2314.
- (3) R. M. Bullock, J. G. Chen, L. Gagliardi, P. J. Chirik, O. K. Farha, C. H. Hendon, C. W. Jones, J. A. Keith, J. Klosin, S. D. Minteer, R. H. Morris, A. T. Radosevich, T. B. Rauchfuss, N. A. Strotman, A. Vojvodic, T. R. Ward, J. Y. Yang and Y. Surendranath, *Science*, 2020, **369**, eabc3183.
- (4) V. Smil, *Enriching the Earth: Fritz Haber, Carl Bosch, and the Transformation of World Food Production*, MIT University Press Group Ltd, Cambridge, Mass. and London, 2001.
- (5) C. Smith, A. K. Hill and L. Torrente-Murciano, *Energy Environ. Sci.*, 2020, **13**, 331–344.
- (6) B. Ruscic, D. Feller and K. A. Peterson, *Theor. Chem. Acc.*, 2013, **133**, 1415.
- (7) B. deB. Darwent, *Bond Dissociation Energies in Simple Molecules*, tech. rep. NSRDS-NBS 31, National Bureau of Standards, 1970.
- (8) B. K. Burgess and D. J. Lowe, *Chem. Rev.*, 1996, **96**, 2983–3012.
- (9) J. Chatt, J. R. Dilworth, R. L. Richards and J. R. Sanders, *Nature*, 1969, **224**, 1201–1202.

- (10) M. Georgiadis, H. Komiya, P. Chakrabarti, D. Woo, J. Kornuc and D. Rees, *Science*, 1992, **257**, 1653–1659.
- (11) O. Einsle, F. A. Tezcan, S. L. A. Andrade, B. Schmid, M. Yoshida, J. B. Howard and D. C. Rees, *Science*, 2002, **297**, 1696–1700.
- (12) L. C. Seefeldt, B. M. Hoffman and D. R. Dean, *Annu. Rev. Biochem.*, 2009, **78**, 701–722.
- (13) K. Danyal, B. S. Inglet, K. A. Vincent, B. M. Barney, B. M. Hoffman, F. A. Armstrong, D. R. Dean and L. C. Seefeldt, *J. Am. Chem. Soc.*, 2010, **132**, 13197–13199.
- (14) K. Danyal, D. Mayweather, D. R. Dean, L. C. Seefeldt and B. M. Hoffman, *J. Am. Chem. Soc.*, 2010, **132**, 6894–6895.
- (15) T. Spatzal, M. Aksoyoglu, L. Zhang, S. L. A. Andrade, E. Schleicher, S. Weber, D. C. Rees and O. Einsle, *Science*, 2011, **334**, 940.
- (16) K. Lancaster, M. Roemelt, P. Ettenhuber, Y. Hu, M. Ribbe, F. Neese, U. Bergmann and S. DeBeer, *Science*, 2011, **334**, 974–977.
- (17) S. E. Creutz and J. C. Peters, *J. Am. Chem. Soc.*, 2014, **136**, 1105–1115.
- (18) I. Čorić, B. Q. Mercado, E. Bill, D. J. Vinyard and P. L. Holland, *Nature*, 2015, **526**, 96–99.
- (19) B. M. Hoffman, D. Lukoyanov, Z.-Y. Yang, D. R. Dean and L. C. Seefeldt, *Chem. Rev.*, 2014, **114**, 4041–4062.
- (20) P. E. Wilson, A. C. Nyborg and G. D. Watt, *Biophys. Chem.*, 2001, **91**, 281–304.
- (21) R. N. F. Thorneley and D. J. Lowe, in *Molybdenum Enzymes*, ed. T. G. Spiro, Wiley, New York, 1985, pp. 221–284.
- (22) D. Schilter, J. M. Camara, M. T. Huynh, S. Hammes-Schiffer and T. B. Rauchfuss, *Chem. Rev.*, 2016, **116**, 8693–8749.

- (23) J. Li and R. H. Burris, *Biochemistry*, 1983, **22**, 4472–4480.
- (24) K. Fisher, M. J. Dilworth and W. E. Newton, *Biochemistry*, 2000, **39**, 15570–15577.
- (25) T. Spatzal, K. A. Perez, O. Einsle, J. B. Howard and D. C. Rees, *Science*, 2014, **345**, 1620–1623.
- (26) R. R. Schrock, *Acc. Chem. Res.*, 2005, **38**, 955–962.
- (27) J. S. Anderson, J. Rittle and J. C. Peters, *Nature*, 2013, **501**, 84–87.
- (28) M. M. Rodriguez, E. Bill, W. W. Brennessel and P. L. Holland, *Science*, 2011, **334**, 780–783.
- (29) A. D. Allen and C. V. Senoff, *Chem. Commun.*, 1965, 621.
- (30) K. Nakamoto, *Infrared Spectra of Inorganic and Co-ordination Compounds*, Wiley, New York, 1963.
- (31) T. Bazhenova and A. Shilov, *Coord. Chem. Rev.*, 1995, **144**, 69–145.
- (32) A. E. Shilov, *Russ. Chem. Bull.*, 2003, **52**, 2555–2562.
- (33) T. I. Al-Salih and C. J. Pickett, *J. Chem. Soc., Dalton Trans.*, 1985, 1255.
- (34) M. Kol, R. R. Schrock, R. Kempe and W. M. Davis, *J. Am. Chem. Soc.*, 1994, **116**, 4382–4390.
- (35) D. V. Yandulov and R. R. Schrock, *J. Am. Chem. Soc.*, 2002, **124**, 6252–6253.
- (36) D. V. Yandulov and R. R. Schrock, *Science*, 2003, **301**, 76–78.
- (37) F. Studt and F. Tuczek, *Angew. Chem. Int. Ed.*, 2005, **44**, 5639–5642.
- (38) K. Arashiba, Y. Miyake and Y. Nishibayashi, *Nat. Chem.*, 2010, **3**, 120–125.
- (39) E. Kinoshita, K. Arashiba, S. Kuriyama, Y. Miyake, R. Shimazaki, H. Nakanishi and Y. Nishibayashi, *Organometallics*, 2012, **31**, 8437–8443.
- (40) Y.-H. Tian, A. W. Pierpont and E. R. Batista, *Inorg. Chem.*, 2014, **53**, 4177–4183.

- (41) Y. Ashida, K. Arashiba, K. Nakajima and Y. Nishibayashi, *Nature*, 2019, **568**, 536–540.
- (42) M.-E. Moret and J. C. Peters, *Angew. Chem. Int. Ed.*, 2011, **50**, 2063–2067.
- (43) Y. Lee, N. P. Mankad and J. C. Peters, *Nat. Chem.*, 2010, **2**, 558–565.
- (44) H. Fong, M.-E. Moret, Y. Lee and J. C. Peters, *Organometallics*, 2013, **32**, 3053–3062.
- (45) K. M. Lancaster, Y. Hu, U. Bergmann, M. W. Ribbe and S. DeBeer, *J. Am. Chem. Soc.*, 2013, **135**, 610–612.
- (46) J. Kfoury, Z. Benedek, T. Szilvási and J. Oláh, *Organometallics*, 2022, **41**, 1134–1146.
- (47) R. Hille, *Dalton Trans.*, 2013, **42**, 3029.
- (48) J. H. Enemark, J. J. A. Cooney, J.-J. Wang and R. H. Holm, *Chem. Rev.*, 2004, **104**, 1175–1200.
- (49) M. Dixon and S. Thurlow, *Biochem. J.*, 1924, **18**, 971–975.
- (50) R. Hille, *Essays Biochem.*, 1999, **34**, ed. D. P. Ballou, 125–137.
- (51) R. Hille, *Trends Biochem. Sci.*, 2002, **27**, 360–367.
- (52) H. Dobbek, L. Gremer, R. Kiefersauer, R. Huber and O. Meyer, *Proc. Natl. Acad. Sci. USA*, 2002, **99**, 15971–15976.
- (53) L. M. Thomson and M. B. Hall, *J. Am. Chem. Soc.*, 2001, **123**, 3995–4002.
- (54) N. R. Bastian, C. J. Kay, M. J. Barber and K. V. Rajagopalan, *J. Biol. Chem.*, 1991, **266**, 45–51.
- (55) D. C. Rees, Y. Hu, C. Kisker and H. Schindelin, *J. Chem. Soc., Dalton Trans.*, 1997, 3909–3914.
- (56) M. K. Johnson, D. C. Rees and M. W. W. Adams, *Chem. Rev.*, 1996, **96**, 2817–2840.

- (57) T. Schindler, A. Sauer, T. P. Spaniol and J. Okuda, *Organometallics*, 2018, **37**, 4336–4340.
- (58) H. Marom, S. Antonov, Y. Popowski and M. Gozin, *J. Org. Chem.*, 2011, **76**, 5240–5246.
- (59) B. S. Lim, M. W. Willer, M. Miao and R. H. Holm, *J. Am. Chem. Soc.*, 2001, **123**, 8343–8349.
- (60) H. Oku, N. Ueyama, M. Kondo and A. Nakamura, *Inorg. Chem.*, 1994, **33**, 209–216.
- (61) H. Oku, N. Ueyama and K. Nakamura, *Inorg. Chem.*, 1995, **34**, 3667–3676.
- (62) N. Ueyama, H. Oku, M. Kondo, T.-A. Okamura, N. Yoshinaga and A. Nakamura, *Inorg. Chem.*, 1996, **35**, 643–650.
- (63) H. Sugimoto, S. Tatemoto, K. Suyama, H. Miyake, S. Itoh, C. Dong, J. Yang and M. L. Kirk, *Inorg. Chem.*, 2009, **48**, 10581–10590.
- (64) H. Sugimoto, S. Tatemoto, K. Toyota, K. Ashikari, M. Kubo, T. Ogura and S. Itoh, *Chem. Commun.*, 2013, **49**, 4358–4360.
- (65) H. Sugimoto, S. Tatemoto, K. Suyama, H. Miyake, R. P. Mtei, S. Itoh and M. L. Kirk, *Inorg. Chem.*, 2010, **49**, 5368–5370.
- (66) S. Enthaler, *ChemSusChem*, 2008, **1**, 801–804.
- (67) F. Joó, *ChemSusChem*, 2008, **1**, 805–808.
- (68) M. L. Man, Z. Zhou, S. M. Ng and C. P. Lau, *Dalton Trans.*, 2003, 3727–3735.
- (69) S. H. Strauss, K. H. Whitmire and D. F. Shriver, *J. Organomet. Chem.*, 1979, **174**, C59–C62.
- (70) T. C. Johnson, D. J. Morris and M. Wills, *Chem. Soc. Rev.*, 2010, **39**, 81–88.
- (71) R. Kanega, N. Onishi, L. Wang and Y. Himeda, *ACS Catal.*, 2018, **8**, 11296–11301.

- (72) A. Kumar, S. Semwal and J. Choudhury, *ACS Catal.*, 2019, **9**, 2164–2168.
- (73) G. H. Gunasekar, K. Park, K.-D. Jung and S. Yoon, *Inorg. Chem. Front.*, 2016, **3**, 882–895.
- (74) A. A. Danopoulos, J. A. Wright and W. B. Motherwell, *Chem. Commun.*, 2005, 784–786.
- (75) H. W. Wanzlick, *Angew. Chem., Int. Ed. Engl.*, 1962, **1**, 75–80.
- (76) H.-W. Wanzlick and H.-J. Schönherr, *Angew. Chem., Int. Ed. Engl.*, 1968, **7**, 141–142.
- (77) K. Öfele, *J. Organomet. Chem.*, 1968, **12**, P42–P43.
- (78) A. J. Arduengo, R. L. Harlow and M. Kline, *J. Am. Chem. Soc.*, 1991, **113**, 361–363.
- (79) W. A. Herrmann and C. Köcher, *Angew. Chem., Int. Ed. Engl.*, 1997, **36**, 2162–2187.
- (80) D. J. Nelson and S. P. Nolan, *Chem. Soc. Rev.*, 2013, **42**, 6723.
- (81) M. F. Lappert, P. L. Pye and G. M. McLaughlin, *J. Chem. Soc., Dalton Trans.*, 1977, 1272–1282.
- (82) M. Scholl, S. Ding, C. W. Lee and R. H. Grubbs, *Org. Lett.*, 1999, **1**, 953–956.
- (83) Y. Ohki, K. Aoyagi and H. Seino, *Organometallics*, 2015, **34**, 3414–3420.
- (84) J. Chatt, A. J. Pearman and R. L. Richards, *Nature*, 1975, **253**, 39–40.
- (85) J. Chatt, A. J. Pearman and R. L. Richards, *J. Chem. Soc., Dalton Trans.*, 1977, 1852.
- (86) A. Watakabe, T. Takahashi, D.-M. Jin, I. Yokotake, Y. Uchida and M. Hidai, *J. Organomet. Chem.*, 1983, **254**, 75–82.
- (87) A. A. Danopoulos, A. A. D. Tulloch, S. Winston, G. Eastham and M. B. Hursthouse, *Dalton Trans.*, 2003, 1009–1015.

- (88) A. Hills, D. L. Hughes, M. Jimenez-Tenorio, G. J. Leigh and A. T. Rowley, *J. Chem. Soc., Dalton Trans.*, 1993, 3041–3049.
- (89) D. Pugh, J. A. Wright, S. Freeman and A. A. Danopoulos, *Dalton Trans.*, 2006, 775–782.
- (90) D. S. McGuinness, V. C. Gibson, D. F. Wass and J. W. Steed, *J. Am. Chem. Soc.*, 2003, **125**, 12716–12717.
- (91) Y. Zhang, B. S. Hanna, A. Dineen, P. G. Williard and W. H. Bernskoetter, *Organometallics*, 2013, **32**, 3969–3979.
- (92) M. L. Helm, M. P. Stewart, R. M. Bullock, M. R. DuBois and D. L. DuBois, *Science*, 2011, **333**, 863–866.
- (93) M. O’Hagan, M.-H. Ho, J. Y. Yang, A. M. Appel, M. R. DuBois, S. Rauegi, W. J. Shaw, D. L. DuBois and R. M. Bullock, *J. Am. Chem. Soc.*, 2012, **134**, 19409–19424.
- (94) W. J. Shaw, M. L. Helm and D. L. DuBois, *Biochim. Biophys. Acta, Bioenerg.*, 2013, **1827**, 1123–1139.
- (95) T. Liu, D. L. DuBois and R. M. Bullock, *Nat. Chem.*, 2013, **5**, 228–233.
- (96) P. Bhattacharya, D. E. Prokopchuk and M. T. Mock, *Coord. Chem. Rev.*, 2017, **334**, 67–83.
- (97) L. A. Labios, Z. M. Heiden and M. T. Mock, *Inorg. Chem.*, 2015, **54**, 4409–4422.
- (98) C. J. Weiss, A. N. Groves, M. T. Mock, W. G. Dougherty, W. S. Kassel, M. L. Helm, D. L. DuBois and R. M. Bullock, *Dalton Trans.*, 2012, **41**, 4517.
- (99) L. A. Labios, C. J. Weiss, J. D. Egbert, S. Lense, R. M. Bullock, W. G. Dougherty, W. S. Kassel and M. T. Mock, *Z. Anorg. Allg. Chem.*, 2014, **641**, 105–117.
- (100) A. L. Johnson, *US Patent*, 3 637 731, E. I. DuPont, 1972.

- (101) X. Bantreil and S. P. Nolan, *Nat. Protoc.*, 2010, **6**, 69–77.
- (102) F. Stoffelbach, D. Saurenz and R. Poli, *Eur. J. Inorg. Chem.*, 2001, **2001**, 2699–2703.
- (103) R. J. Errington, *Advanced Practical Inorganic and Metalorganic Chemistry*, Taylor & Francis Group, London, 2017.
- (104) J. M. Darmon, S. Raugei, T. Liu, E. B. Hulley, C. J. Weiss, R. M. Bullock and M. L. Helm, *ACS Catal.*, 2014, **4**, 1246–1260.
- (105) T. Reda, C. M. Plugge, N. J. Abram and J. Hirst, *Proc. Natl. Acad. Sci. USA*, 2008, **105**, 10654–10658.
- (106) W. E. Robinson, A. Bassegoda, E. Reisner and J. Hirst, *J. Am. Chem. Soc.*, 2017, **139**, 9927–9936.
- (107) A. R. Oliveira, C. Mota, C. Mourato, R. M. Domingos, M. F. A. Santos, D. Gesto, B. Guigliarelli, T. Santos-Silva, M. J. Romão and I. A. C. Pereira, *ACS Catal.*, 2020, **10**, 3844–3856.
- (108) G. N. Schrauzer, V. P. Mayweg and W. Heinrich, *J. Am. Chem. Soc.*, 1966, **88**, 5174–5179.
- (109) P. Chandrasekaran, K. Arumugam, U. Jayarathne, L. M. Pérez, J. T. Mague and J. P. Donahue, *Inorg. Chem.*, 2009, **48**, 2103–2113.
- (110) T. Fogeron, T. K. Todorova, J.-P. Porcher, M. Gomez-Mingot, L.-M. Chamoreau, C. Mellot-Draznieks, Y. Li and M. Fontecave, *ACS Catal.*, 2018, **8**, 2030–2038.
- (111) T. Fogeron, P. Retailleau, L.-M. Chamoreau, Y. Li and M. Fontecave, *Angew. Chem. Int. Ed.*, 2018, **57**, 17033–17037.
- (112) D. A. Brown and F. J. Hughes, *J. Chem. Soc. A*, 1968, **0**, 1519–1523.
- (113) G. W. Wagner and B. E. Hanson, *Organometallics*, 1987, **6**, 2494–2498.

- (114) H. Sashida, K. Ohyanagi, M. Minoura and K.-Y. Akiba, *J. Chem. Soc., Perkin Trans. 1*, 2002, 606–612.
- (115) H. Yu, R. N. Richey, M. W. Carson and M. J. Coghlan, *Org. Lett.*, 2006, **8**, 1685–1688.
- (116) P. G. M. Wuts and T. W. Greene, *Greene's Protective Groups in Organic Synthesis*, Wiley-Interscience, Hoboken, N.J, 2007.
- (117) J. A. McCleverty, *Prog. Inorg. Chem.*, 1968, 49–221.
- (118) E. Hoyer, W. Dietzsch and W. Schroth, *Z. Chem.*, 1971, **11**, 41–53.
- (119) D. V. Fomitchev, B. S. Lim and R. H. Holm, *Inorg. Chem.*, 2001, **40**, 645–654.
- (120) K. A. Scheidt, H. Chen, B. C. Follows, S. R. Chemler, D. S. Coffey and W. R. Roush, *J. Org. Chem.*, 1998, **63**, 6436–6437.
- (121) T. Ohshima, Y. Xu, R. Takita, S. Shimizu, D. Zhong and M. Shibasaki, *J. Am. Chem. Soc.*, 2002, **124**, 14546–14547.
- (122) W. G. Earley, J. E. Jacobsen, A. Madin, G. P. Meier, C. J. O'Donnell, T. Oh, D. W. Old, L. E. Overman and M. J. Sharp, *J. Am. Chem. Soc.*, 2005, **127**, 18046–18053.
- (123) L. Pfeifer and V. Gouverneur, *Org. Lett.*, 2018, **20**, 1576–1579.
- (124) W. Kohn and L. J. Sham, *Phys. Rev.*, 1965, **140**, A1133–A1138.
- (125) P. Hohenberg and W. Kohn, *Phys. Rev.*, 1964, **136**, B864–B871.
- (126) W. Koch and M. C. Holthausen, *A Chemist's Guide to Density Functional Theory*, Wiley-VCH, Weinheim New York, 2001.
- (127) E. J. Baerends, T. Ziegler, J. Autschbach, D. Bashford, F. M. B. A. Bérces, C. Bo, P. M. Boerrigter, L. Cavallo, D. P. Chong, L. Deng, R. M. Dickson, D. E. Ellis, M. van Faassen, L. Fan, T. H. Fischer, C. F. Guerra, M. Franchini, A. Ghysels, A. Giammona, S. J. A. van Gisbergen, A. W. Götz, O. V. G. J. A. Groeneveld, M. Grüning, S. Gusarov, F. E. Harris, P. van den Hoek, C. R.

- Jacob, H. Jacobsen, L. Jensen, J. W. Kaminski, G. van Kessel, F. Kootstra, A. Kovalenko, M. V. Krykunov, E. van Lenthe, D. A. McCormack, A. Michalak, M. Mitoraj, S. M. Morton, J. Neugebauer, V. P. Nicu, L. Noodleman, V. P. Osinga, S. Patchkovskii, M. Pavanello, P. H. T. Philipsen, C. C. P. D. Post, W. Ravenek, J. I. Rodríguez, P. Ros, P. R. T. Schipper, H. van Schoot, G. Schreckenbach, J. S. Seldenthuis, M. Seth, J. G. Snijders, M. Solà, M. Swart, D. Swerhone, G. te Velde, P. Vernooijs, L. Versluis, L. Visscher, O. Visser, F. Wang, T. A. Wesolowski, E. M. van Wezenbeek, G. Wiesenekker, S. K. Wolff, T. K. Woo and A. L. Yakovlev, *ADF2014*, SCM, Theoretical Chemistry, Vrije Universiteit, Amsterdam, The Netherlands, 2014.
- (128) G. te Velde, F. M. Bickelhaupt, E. J. Baerends, C. F. Guerra, S. J. A. van Gisbergen, J. G. Snijders and T. Ziegler, *J. Comput. Chem.*, 2001, **22**, 931–967.
- (129) C. F. Guerra, J. G. Snijders, G. te Velde and E. J. Baerends, *Theo. Chem. Acc.*, 1998, **99**, 391–403.
- (130) L. Dang, X. Yang, J. Zhou, E. N. Brothers and M. B. Hall, *J. Phys. Chem. A*, 2011, **116**, 476–482.
- (131) M. J. Frisch, G. W. Trucks, H. B. Schlegel, G. E. Scuseria, M. A. Robb, J. R. Cheeseman, G. Scalmani, V. Barone, B. Mennucci, G. A. Petersson, H. Nakatsuji, M. Caricato, X. Li, H. P. Hratchian, A. F. Izmaylov, J. Bloino, G. Zheng, J. L. Sonnenberg, M. Hada, M. Ehara, K. Toyota, R. Fukuda, J. Hasegawa, M. Ishida, T. Nakajima, Y. Honda, O. Kitao, H. Nakai, T. Vreven, J. A. Montgomery, Jr., J. E. Peralta, F. Ogliaro, M. Bearpark, J. J. Heyd, E. Brothers, K. N. Kudin, V. N. Staroverov, R. Kobayashi, J. Normand, K. Raghavachari, A. Rendell, J. C. Burant, S. S. Iyengar, J. Tomasi, M. Cossi, N. Rega, J. M. Millam, M. Klene, J. E. Knox, J. B. Cross, V. Bakken, C. Adamo, J. Jaramillo, R. Gomperts, R. E. Stratmann, O. Yazyev, A. J.

- Austin, R. Cammi, C. Pomelli, J. W. Ochterski, R. L. Martin, K. Morokuma, V. G. Zakrzewski, G. A. Voth, P. Salvador, J. J. Dannenberg, S. Dapprich, A. D. Daniels, Ö. Farkas, J. B. Foresman, J. V. Ortiz, J. Cioslowski and D. J. Fox, *Gaussian 09 Revision C.01*, Gaussian, Inc., Wallingford, CT, 2009.
- (132) A. D. Becke, *J. Chem. Phys.*, 1993, **98**, 5648–5652.
- (133) J. Tao, J. P. Perdew, V. N. Staroverov and G. E. Scuseria, *Phys. Rev. Lett.*, 2003, **91**, 146401–146405.
- (134) J. P. Perdew, *Phys. Rev. B*, 1986, **33**, 8822–8824.
- (135) A. D. Becke, *Phys. Rev. A*, 1988, **38**, 3098–3100.
- (136) J.-D. Chai and M. Head-Gordon, *J. Chem. Phys.*, 2008, **128**, 084106.
- (137) B. S. Lim, J. P. Donahue and R. H. Holm, *Inorg. Chem.*, 2000, **39**, 263–273.
- (138) N. Elgrishi, K. J. Rountree, B. D. McCarthy, E. S. Rountree, T. T. Eisenhart and J. L. Dempsey, *J. Chem. Educ.*, 2017, **95**, 197–206.
- (139) N. G. Tsierkezos, *J. Solution Chem.*, 2007, **36**, 289–302.
- (140) R. H. Holm and M. J. O'Connor, 1971, 241–401.
- (141) *Dithiolene Chemistry*, ed. E. I. Stiefel, John Wiley & Sons, Inc., 2003.
- (142) G. A. Bowmaker, P. D. W. Boyd and G. K. Campbell, *Inorg. Chem.*, 1983, **22**, 1208–1213.
- (143) A. Zarkadoulas, M. J. Field, V. Artero and C. A. Mitsopoulou, *ChemCatChem*, 2017, **9**, 2308–2317.
- (144) A. Zarkadoulas, M. J. Field, C. Papatriantafyllopoulou, J. Fize, V. Artero and C. A. Mitsopoulou, *Inorg. Chem.*, 2015, **55**, 432–444.
- (145) J.-P. Porcher, T. Fogeron, M. Gomez-Mingot, E. Derat, L.-M. Chamoreau, Y. Li and M. Fontecave, *Angew. Chem. Int. Ed.*, 2015, **54**, 14090–14093.
- (146) A. J. Bard and L. R. Faulkner, *Electrochemical Methods, Fundamentals and Applications*, Wiley, 2000, p. 856.

- (147) Y. Ito, T. Aoyama and T. Shioiri, *Synlett*, 1997, **1997**, 1163–1164.
- (148) L. Jamir, R. Yella and B. K. Patel, *J. Sulfur Chem.*, 2009, **30**, 128–134.
- (149) *APEX2*, Bruker AXS Inc., Madison, Wisconsin, USA, 2012.
- (150) *SAINT*, Bruker AXS Inc., Madison, Wisconsin, USA, 2012.
- (151) *CrystalClear-SM Expert*, Rigaku Americas Corporation, The Woodlands, Texas, USA, 2013.
- (152) *CrysAlis Pro*, Rigaku OD, Yarnton, United Kingdom, 2015.
- (153) G. M. Sheldrick, *Acta Cryst. A*, 2015, **71**, 3–8.
- (154) G. M. Sheldrick, *Acta Cryst. C*, 2015, **71**, 3–8.
- (155) E. van Lenthe, E. J. Baerends and J. G. Snijders, *J. Chem. Phys.*, 1993, **99**, 4597–4610.